

Axial and Lateral Behavior of Helical Piles under Static Loads

By

Weidong Li

A thesis submitted in partial fulfillment of the requirements for the degree of

Master of Science

in

GEOTECHNICAL ENGINEERING

Department of Civil and Environmental Engineering

University of Alberta

©Weidong Li, 2016

Abstract

Helical piles have been used extensively in Western Canada to support the superstructures particularly with applications in power transmission towers, commercial buildings, camps, and so on. Extensive research in helical piles has been conducted using physical testing methods; however, there has been insufficient research in the numerical modeling soil-helical pile interaction in axial or lateral directions. The present research is thus carried out to bridge the knowledge gap.

The first part of present research is aimed to investigate the behavior of helical piles subject to axial static loading using field load tests and numerical simulation based on Beam-on-Nonlinear- Winkler-Foundation (BNWF) methodology. Field load tests were conducted on 26 single-helix piles including 15 compression tests and 11 tension tests in two types of soils in Alberta, Canada. The soils in the two selected sites were classified as medium to stiff clay, and medium to dense sand respectively. Three sizes of helical piles whose shaft diameters varied from 7.3 cm to 11.4 cm were tested according to the same test procedures. The load-displacement curves were obtained to show the axial behavior of the helical piles under axial static load. Installation torque was recorded per foot penetration into the ground to portrait the correlations between the installation torque and bearing or uplift capacity. Cone penetration tests (CPT) were applied to develop soil profiles of the test sites to provide input parameters to the numerical models.

The field tests provide case studies to the subsequent finite element analyses of axial soil-pile interaction. A BNWF model was developed on the platform of Open System for Earthquake Engineering Simulation (OpenSees). Soil reaction springs (p - y , q - z and t - z) were adopted by the developed model to simulate the integrated behavior of piles. It was

found that the existing soil reaction spring implemented in OpenSees were capable of simulating the axial behavior of helical piles.

The second part of present research is aimed to investigate the lateral soil-pile interaction using the BNWF model developed in OpenSees. In the literature, the effects of helix on the lateral capacity of helical piles have not been quantified. The numerical model was calibrated against published results of lateral load tests of helical piles. Systematic parametric analyses of helical piles using the BNWF models were conducted to observe the lateral capacity improvement due to the change of size and embedment depth of the helix, diameter and length of the bucket (partially enlarged pile shaft), and the soil classification (clay and sand). The effect of these geometric factors on the lateral capacity of helical piles was quantified, and the results of the parametric studies may be used for the practical design of lateral capacities of helical piles.

Acknowledgement

I would like to extend my sincere gratitude to Dr. Lijun Deng for his wise and patient guidance throughout my research program. His support, encouragement, and care to his student in the last three years have improved not only my technical skills but also the cognition of life. I would also like to express my thanks to Dr. Carlos Cruz Noguez for his advices in the development of my numerical models.

I truly appreciate the financial support of Natural Sciences and Engineering Research Council of Canada- Industrial Postgraduate Scholarship with the contribution from Almita Piling Inc. This thesis will be impossible without the support.

Great thanks go to Shaikh Islam and Jesse Liu, Almita's engineers, who spent days on the field tests with me. I am thankful to Almita staff, Mohamed Abdelaziz, Baocheng Li, and Richard Schmidt for their training on helical piles and Almita Piling Inc. for permitting the publication of field test results.

Special gratitude goes to my parents for their understanding and support during these years I have spent overseas on studying.

Table of Contents

Abstract	ii
Acknowledgement	iv
List of Figures	viii
List of Tables	xi
List of Symbols	xii
1 Introduction	1
1.1 Background and problem statement.....	1
1.2 Objectives.....	3
1.3 Scope of work.....	3
1.4 Thesis organization	4
2 Literature Review	9
2.1 Current theories of helix behavior.....	9
2.2 Axial resistance	11
2.2.1 Shaft skin friction or adhesion	12
2.2.2 End bearing and uplift resistance	17
2.3 Lateral resistance.....	18
2.3.1 Lateral shaft resistance.....	18
2.3.2 Effect of helical plate on lateral capacity.....	20
3 Field Testing and Numerical Modeling of Axial Behavior of Single-helix Piles	35
Abstract	35
3.1 Introduction	35
3.2 Subsurface investigation	36

3.3	Field testing program	38
3.3.1	Pile installation.....	38
3.3.2	Pile dimensions and set-up.....	38
3.3.3	Load reaction system	39
3.3.4	Testing Procedure	40
3.4	Tests results	41
3.4.1	Load vs. Displacement Curves	41
3.4.2	Torque factor analysis.....	42
3.5	Development of numerical models	43
3.6	Numerical simulation results.....	44
3.7	Conclusions	46
4	Numerical Modeling of Lateral Behavior of Helical Piles and Parametric Analyses	66
	Abstract	66
4.1	Introduction	66
4.2	Development of Numerical Models	68
4.2.1	Selected case studies for numerical model calibration	70
4.2.2	Calibration of soil reaction springs	71
4.3	Parametric Analyses.....	74
4.3.1	Influence of helix diameter D compared to helix embedment H	75
4.3.2	Influence of helix diameter D compared to shaft diameter d	77
4.3.3	Influence of bucket diameter d_B compared to bucket length l_B	78
4.4	Conclusions	79
5	Conclusions	86

5.1	Axial Behavior of Helical Piles.....	86
5.2	Lateral Behavior of Helical Piles	87
5.3	Recommended Future Studies.....	88
	References.....	89
	Appendix – OpenSees code for lateral soil – helical pile interaction.....	96

List of Figures

Figure 1-1: Sketches of single-helix, multi-helix, and bucket piles	5
Figure 1-2: Picture of single-helix piles, multi-helix piles, and bucket pile.....	6
Figure 1-3: Selected applications of helical piles	7
Figure 1-4: The performance of helical pile vs. conventional pile	8
Figure 2-1: Helical pile failure models (a) individual bearing model, single-helix pile (b) individual bearing model, multi-helix pile (c) cylindrical shearing model (d) mix of two models	24
Figure 2-2: Compression load transfer mechanism: (a) UofA Farm (b) Sand Pit (After Zhang, 1999, redrawn in Li et al. 2016).....	25
Figure 2-3: Tension load transfer mechanism: (a) UofA Farm (b) Sand Pit (After Zhang, 1999, redrawn in Li et al. 2016).....	25
Figure 2-4: Friction or adhesion development along the shaft: (a) compression (b) tension (Li et al. 2016)	26
Figure 2-5: Skin friction vs. axial displacement curve of driven piles in sand (After Mosher 1984)	27
Figure 2-6: Ultimate skin friction of driven piles in sand (After Castello 1980)	27
Figure 2-7: Skin friction vs. axial displacement curve of driven piles in sand (After Vijayvirgiya 1977).....	28
Figure 2-8: Shaft adhesion vs. axial displacement curve in clay (After Coyle and Reese 1966). 28	
Figure 2-9: The ultimate shaft adhesion vs. undrained shear strength (After Coyle and Reese 1966).....	29

Figure 2-10: The ultimate steel shaft adhesion vs. undrained shear strength (After Tomlinson 1957)	29
Figure 2-11: Shaft adhesion vs. axial displacement curve in clay (After Heydinger and O’Neill 1986)	30
Figure 2-12: The $t-z$ curves adopted by OpenSees (After Boulanger et al. 1999)	30
Figure 2-13. Ultimate end bearing in sand (After Mosher 1984)	31
Figure 2-14: Q-z curves and the fitting curves derived by Boulanger et al. (1999)	31
Figure 2-15: Initial subgrade reaction constant (After API, 1993)	32
Figure 2-16: P-y curve in sand (After API, 1993) and clay (After Matlock, 1970)	32
Figure 2-17: Model piles used to test the effect of helical plate(s) on lateral capacity of helical piles (Prasad and Narasimha Rao, 1996)	33
Figure 2-18: Lateral load vs. deflection of the three types of piles as shown in Figure 2-17 (Prasad and Narasimha Rao, 1996)	33
Figure 2-19: Lateral load vs. deflection of two relevant double-helix and single-helix piles (Sakr 2009)	34
Figure 3-1: Locations of two test sites	51
Figure 3-2: Layout of the piles and CPT boreholes	52
Figure 3-3: CPT profile of Site 1 at the University of Alberta Farm	52
Figure 3-4: CPT profile of Site 2 at the Sand Pit in Bruderheim	53
Figure 3-5: Installation of a helical pile	54
Figure 3-6: The true helix design	54
Figure 3-7: Test frame of axial compression loading	55
Figure 3-8: Test frame of axial tension loading	55

Figure 3-9: Setup of axial compression tests	56
Figure 3-10: Setup of axial tension tests.....	57
Figure 3-11: Test results from Site 1	58
Figure 3-12: Test results from Site 2	59
Figure 3-13: Axial ultimate capacity interpretation using the load-displacement curves of Type1 piles (P1) under compression (P1C) and tension (P1T) loading at Site1	60
Figure 3-14: Torque factor design charts for the tested piles	62
Figure 3-15: Numerical model configuration	63
Figure 3-16: Comparison of numerical modeling to the in-situ test results of selected helical piles in clay (a)(b), and sand (c)(d)	64
Figure 3-17: The components of numerical load-displacement curve for S2P2C.....	65
Figure 3-18: The sensitivity of the axial behavior to the half capacity displacement z_{50}	65
Figure 4-1: The 3-D BNWF model for a single-helix pile	82
Figure 4-2: The calibration of single-helix pile and straight pile	83
Figure 4-3: Effects of head fixity condition or vertical load on the lateral behaviour of double-helix piles under lateral loading.....	83
Figure 4-4: The lateral capacity improvement due to D/d and H/E	84
Figure 4-5: The bending moment and rotation angle distribution	84
Figure 4-6: The lateral capacity improvement due to the length and diameter of bucket	85

List of Tables

Table 2-1: The factor k_f values based on internal friction angle (After Mosher and Dawkins, 2000) 22

Table 2-2: T_{ult} and z_c values for t - z behavior presented by Vijayvirgiya (1977) 22

Table 2-3: Representative values of k after API (1993) 22

Table 2-4: Representative values of ε_{50} after Matlock (1970)..... 23

Table 3-1. Test pile geometries..... 48

Table 3-2: Axial ultimate capacities 49

Table 3-3: The estimation of parameters of the numerical model for axial loading..... 50

Table 4-1: Pile geometries 81

Table 4-2: Adjustment of parameters of numerical models..... 81

List of Symbols

\bar{A}	adjustment coefficient for static loading
c	a constant that defines the shape of soil reaction curves
C_1, C_2, C_3	factors defined in API (1993) to estimate the lateral soil resistance of piles in sand
C_e	a constant that defines the normalized stiffness of elasticity of soil reaction curves
d	pile shaft diameter, m
D	diameter of the helix, m
d_B	diameter of the bucket, m
E	the embedment of a helical pile, m
E_0	initial undrained elastic modulus of clay, kPa
E_{avg}	average initial undrained elastic modulus of clay, kPa
H	the embedment of helix, m
H_{eff}	effective length, m
H_l	improvement of lateral capacity of helical piles
H_u	lateral capacity of helical piles
H_{u0}	lateral capacity of straight piles
J	a constant accounts for the lateral soil resistance of clay at wedge failure
k	initial subgrade reaction constant, kPa/m
K_0	horizontal coefficient of earth pressure
K_t	torque factor, m ⁻¹
k_f	initial slope of the skin friction – displacement curve, kPa/m
L	length of pile, m

l_B	length of the bucket, m
m	index of adhesion
n	an index that defines the shape of soil reaction curves
N	index accounts for soil density
N_b	breakout factor of anchors in sand
N_c	end bearing factor of piles in clay
N_q	end bearing factor of piles in sand
p_a	the atmosphere pressure, kPa
p	lateral soil resistance, kPa
p_s	govern ultimate lateral soil resistance, kPa
p_{sd}	ultimate lateral soil resistance at flow failure, kPa
p_{st}	ultimate lateral soil resistance at wedge failure, kPa
p_{ult}	ultimate lateral soil resistance, kPa
q	bearing or uplift soil resistance, kPa
Q_u	bearing or uplift capacity of pile, N
q_{ult}	ultimate bearing or uplift soil resistance, kPa
s_u	undrained shear strength, kPa
t	skin friction or adhesion, kPa
T	installation torque, N·m
t^e	elastic component of skin friction or adhesion, kPa
t^p	plastic component of skin friction or adhesion, kPa
t_0^p	t^p at the start of current plastic loading, kPa
t_{ult}	ultimate skin friction or adhesion, kPa

y	lateral displacement, m
y_{50}	lateral displacement at half capacity, m
z	displacement of skin friction or adhesion and/or end bearing or uplift, m
z^e	elastic component of the axial displacement, m
z^p	plastic component of the axial displacement, m
z_0^p	z^p at the start of current plastic loading, m
Z	depth, m
z_{50}	z at half capacity, m
z_{50q}	z_{50} of end bearing or uplift, m
z_{50t}	z_{50} of skin friction or adhesion, m
z_c	z when resistance starts to maintain a constant value, m
α	adhesion factor
β	$45^\circ + \phi/2$
δ	interface friction coefficient
ε_{50}	strain at half of capacity
ϕ	internal friction angle of sand, °
γ	effective unit weight, kN/m ³
σ	vertical effective stress, kPa

1 Introduction

This chapter introduces the background of present research, problem statement, general objectives, and thesis organization.

1.1 Background and problem statement

Helical piles, also known as screw piles or screw anchors are a deep foundation system used to support axial compression, axial tension, and lateral loadings. In general, a helical pile consists of a central shaft, and one or multiple helical plates affixed to the shaft as presented in Figure 1-1 and Figure 1-2. The most commonly used material to fabricate helical piles is steel, and occasionally galvanized to resist corrosion. The shaft can be a hollow circular pipe, a solid circular rod, or a solid squared bar. The solid shaft design is usually adopted for some small diameter piles, and rarely for large diameter piles. For the hollow circular shaft, the toe is usually open ended with a 45-degree cut to minimize the resistance from the soil against the installation. Holes are drilled at the head of the shaft for the plain torque transfer from the driving head to the pile via several bolts, and an extension shaft can also be bolted to the holes if necessary. The helix is affixed to the shaft by welding, bolting, riveting, or being molded in one body with the shaft (Bradka 1997). The number of helices depends on the design. For single-helix design, the helix has to be located at the toe of the shaft to lead the advancement of the pile using the plain torque applied to the pile head. For multiple-helix design, there has to be one helix at the toe of the shaft, and the rest of the helices can be affixed above the bottom helix. The diameters of the helices may be consistent, or tapered, and the spacing between two adjacent helices may be consistent, or varied. Figure 1-1c sketches a pile type named bucket pile, which has a partially enlarged shaft to enhance the lateral capacity.

Engineering applications of helical piles are commonly seen in pipelines, power transmission towers, residential houses, monopoles, and offshore structures. Figure 1-3 shows some of the representative applications. The advantage of helical piles over conventional piles is featured by ease of installation, reusability, instant functionality after installation, and better performance against frost jack (the phenomenon that the pile foundation is jacked up by frost heave). Figure 1-4 illustrates the performance of helical pile against frost jack due to the enhanced uplift capacity by the deep-seated helix.

The most popular design method for the axial capacities of helical piles is the torque factor method, i.e. the final installation torque multiplied by a nominal torque factor for bearing or uplift produces the estimation of the bearing or uplift capacity (Hoyt and Clemence 1989).

However, this method may be not reliable especially when the soil conditions fluctuate substantially; in addition, it was found that the torque factor significantly depends on the dimensions of helical piles, i.e. the shaft diameter, helix number, and helical spacing. Thus, for each helical pile, it is normally necessary to conduct pile-specific load tests to characterize the torque factor for design applications.

Livneh and El Naggar (2008), Kurian and Shah (2009), Mosquera et al. (2015) simulated the axial behavior of helical piles using continuum finite element methods. However, this method is usually out of the capability of design offices thus a simplified numerical model is necessary. In the present study, a simplified method based on beam-on-nonlinear-Winker-foundation approach was selected for the numerical modeling of axial behavior of helical piles.

Published literature in the lateral behavior of helical piles has been fairly limited. The lateral behavior of helical piles has been investigated using experimental methods and continuous finite element methods (e.g. Prasad and Narasimha Rao 1996, Zhang 1999, Sakr 2009, Kurian and

Shah 2009, Al-Baghdadi et al. 2015, Elkasabgy and El Naggar 2015). Different recommendations were proposed: while some literature concludes that the influence of helix on the lateral capacity was negligible, other literature concludes that the helix improves the lateral performance of helical piles. It is speculated that the critical parameters affecting lateral behaviour are helix diameter and helix embedment depth. Therefore, based on the developed 3-D BNWF model, the present study carried out a systematic parametric analysis of the effect of the helix on the lateral capacity. Helix diameter, helix embedment depth, shaft diameter, bucket diameter, bucket length, and soil classification were considered as the variables in the parametric analyses.

1.2 Objectives

The first objective of this study is to investigate the axial compression and tension behavior of three types of single-helix piles that were newly developed by industrial partner, and to develop a numerical model for soil-helical pile interaction using the BNWF method.

The second objective is to investigate the lateral behavior of helical piles (including bucket piles) using BNWF modeling. The numerical models are developed on the platform of Open System of Earthquake Engineering Simulation (OpenSees 2016).

1.3 Scope of work

To fulfill the first objective, field load tests of newly-developed helical piles subject to axial compression and tension were conducted at two representative sites located in Alberta. The University of Alberta farm and a sand pit site in Bruderheim were selected to carry out the axial static loading tests of 26 single-helix piles, of which 15 were for compression and 11 for tension. Both sites are located in Alberta, Canada, and the surficial materials consist of typical lacustrine clay and sand derived from the glacial history of Western Canada. The installation torque was

measured to develop the correlations to the axial capacities. Load vs. displacement curves were obtained from the load tests to investigate the axial behavior of these three types of helical piles. A numerical model using BNWF method was developed in OpenSees to simulate the axial behavior based on the soil parameter profiles obtained from 4 and 3 CPT tests conducted at the University Farm site and Sand Pit site respectively.

To fulfill the second objective, 3-D BNWF models were developed and calibrated based on case studies of lateral load – displacement curves of helical piles in the literature. The calibrated numerical models were used to conduct a series of parametric analyses to investigate the improvement of the lateral capacity due to the contour of the helical pile. Helix diameter, helix embedment depth, shaft diameter, bucket diameter, and bucket length were included in the parametric analyses. The optimum design principles were recommended to improve the lateral capacity evaluation in practice.

1.4 Thesis organization

This thesis consists of five chapters. Chapter 1 introduces helical piles, objectives of research, and thesis organization. Chapter 2 reviews the current literature in the research of helical pile behavior and the soil reaction springs required to simulate the helical pile behavior. Chapter 3 describes the study on the axial behavior of helical piles including the field load test program, site investigation, test results, and numerical modeling. Chapter 4 investigates the lateral behavior of helical piles using numerical modeling. Chapter 5 summarizes the conclusions and direction of research. Appendix A is the source code of the developed numerical model for lateral soil – helical pile interaction.

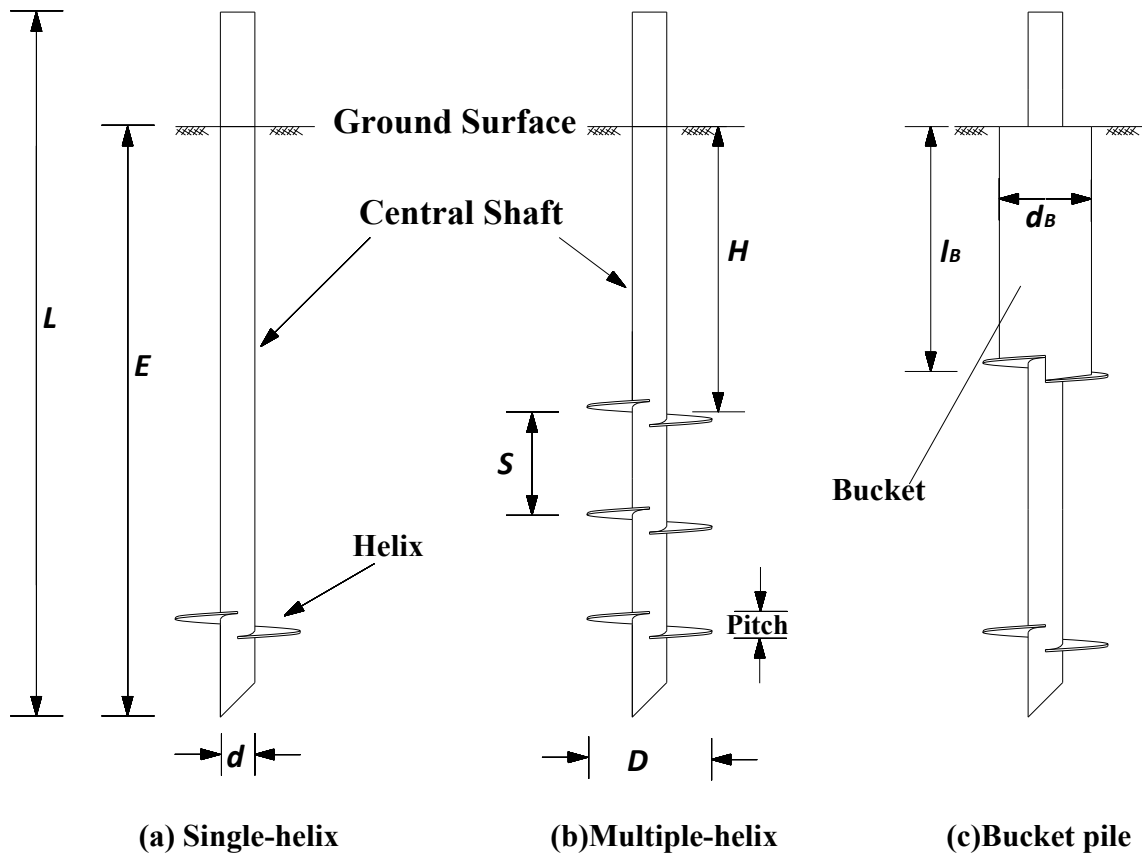


Figure 1-1: Sketches of single-helix, multi-helix, and bucket piles



<http://forums.mtbr.com/trail-building-advocacy/laser-levels-trail-work-952048.html>



From internet



Almita Piling Inc.

Figure 1-2: Picture of single-helix piles, multi-helix piles, and bucket pile



Figure 1-3: Selected applications of helical piles

Frost jack

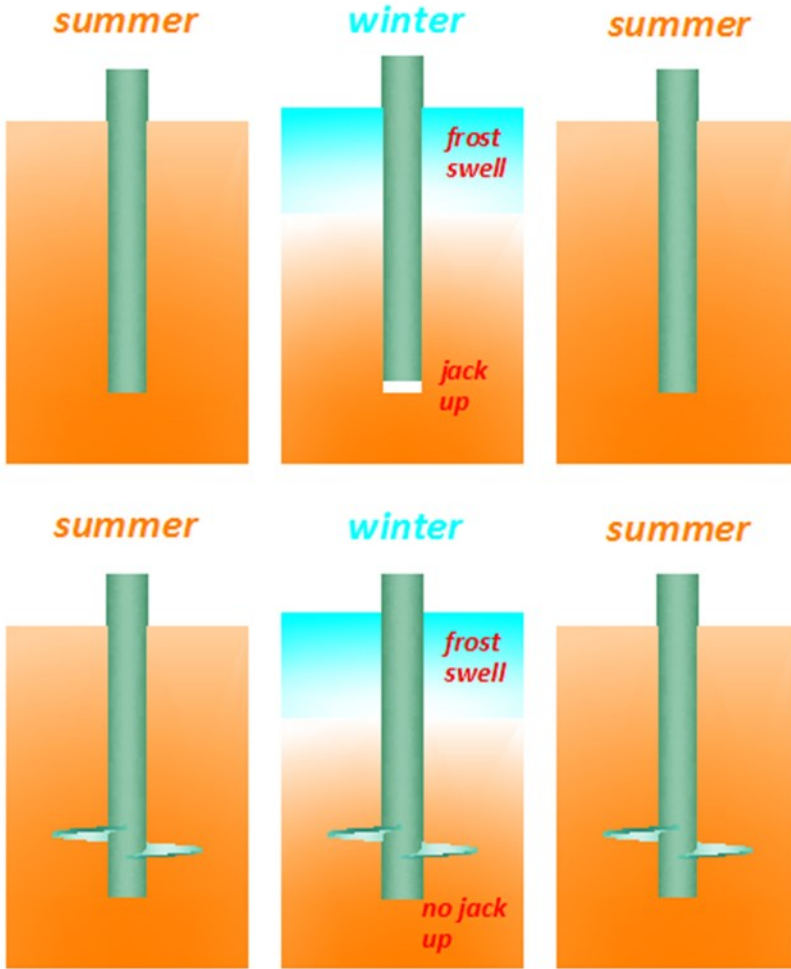


Figure 1-4: The performance of helical pile vs. conventional pile

2 Literature Review

This chapter summarizes the published literature in the behavior of helical piles and conventional piles subject to static loading. Constitutive models of soil reaction springs in the literature are also summarized to assist BNWF modeling that will be used in this study.

2.1 Current theories of helix behavior

The helix has different behavior modes in the axial loading and lateral loading conditions. Under axial loading, the helix carries the bearing or uplift resistance whereas under lateral loading, the overturning resistance carried by the helix consists of normal bearing and uplift resistance, skin friction/adhesion on the upper and lower surfaces, and the resistance on the edge of the helix which is negligible. When the axial limit capacity of the helical pile is reached, the limit bearing or uplift resistance of the helix is mobilized. However in the lateral loading condition, the normal and shearing resistance on the helix surfaces usually has not reached the limit state yet.

Therefore the current design methods in the industry assume the axial capacity of single-helix piles to be the summation of the limit shearing resistance on the shaft, and the limit axial resistance of the helix. But the overturning resistance of the helix in lateral loading condition depends on the rotation and lateral displacement of the helix, which can be significantly affected by the helix embedment depth and the pile bending moment distribution. It is difficult to determine the rotation and lateral displacement of the helix in lateral loading. Hence the current design methods assume the helix has no influence on the lateral capacity of helical piles.

Zhang (1999) and Tappenden and Sego (2007) estimated the helical plate bearing capacity using many theoretical methods developed for conventional pile tip. It is a common practice to assume the helix bearing capacity to be similar to the tip bearing of conventional piles.

Tsuha et al. (2007) and Sakr (2014) both proposed theoretical models to correlate the helix uplift and axial capacity to the installation torque respectively. The spiral geometry of the helix was considered in these two papers including the inclined shearing resistance on the upper and lower surfaces, the shearing resistance on the spiral edge, and the resisting force against the leading edge. Gavin et al. (2014) used field load tests and finite element model to study the axial behavior of helix. The helix was assumed to be two horizontal rigid beams which could not represent the spiral structure of the helix. These theories and methods are capable of predicting the axial capacity of the helical pile but not able to estimate the contribution of the helix to the lateral capacity.

Sakr (2009) developed a numerical model to simulate the lateral performance of helical piles by neglecting the helix. The computed load-deflection curves reached agreement with the test results. However the helices were seated at a great depth that was the main reason why the helix had limited influence. Kurian and Shah (2009) conducted a 3-D continuous finite element study which considered the spiral contour of the helix and found the lateral capacity could be significantly affected by the diameter of the helix, the pitch length of the helix, and even the inclination between the helix and shaft.

These studies provided important knowledge about the behavior of helical piles. However the research in the behavior of helix against overturning is limited. Considering the study of soil reaction springs has been started and complemented for decades. Curras et al. (2001), El Naggar et al. (2005) have accomplished numerical modeling using soil reaction springs existing in the literature. There are three types of soil reaction spring elements, namely TzSimple1 (t - z behavior), QzSimple1 (q - z behavior), and PySimple1 (p - y behavior) implemented in OpenSees by Boulanger et al. (2003). These types of soil elements are normalized to the corresponding

ultimate capacities (t_{ult} , q_{ult} , and p_{ult}) and the displacement of each element at half of the ultimate capacity (z_{50} , z_{50} , and p_{50}). The following literature review summarized the current methods to estimate the ultimate capacities and half capacity displacements so that these soil reaction spring elements can be characterized to simulate the behavior of a helical pile.

2.2 Axial resistance

The resistance of the helical pile against uniaxial loading consists of the skin friction or adhesion developed on the shaft, the individual plate bearing (compressive or uplift) against the helix, and the shearing force developed on the soil cylinder generated between two adjacent helices if applicable (Mooney et al. 1985, Mitsch and Clemence 1985, and Narasimha Rao et al. 1989). A certain spacing ratio value (S/D), the center to center spacing (S) divided by the average diameter (D) of two adjacent helices, has been used as the criteria of the forming of a full soil cylinder. After Narasimha Rao et al. (1991), a critical spacing ratio from 1.0 to 1.5 is recommended for multi-helix piles in medium to stiff clay. Zhang (1999) recommended using the spacing ratio of 2.0 to draw a line between cylindrical shearing model and individual bearing model in cohesionless and cohesive soils. Li et al. (2016) recommended the critical spacing ratio for medium to stiff clay to be between 1.5 and 3.0. Figure 2-1 shows the two failure models, namely individual plate bearing failure and cylindrical shearing failure. It is shown that a single-helix pile can only develop an individual bearing model, but a multi-helix pile may experience a cylindrical shearing and or an individual shearing failure. In the present testing program, only single-helix piles are involved thus the individual bearing model is the suitable method for the evaluation of the axial behavior of the present helical piles.

2.2.1 Shaft skin friction or adhesion

2.2.1.1 Effective length

Skin friction or adhesion resistance is established on the shaft-soil interface of the helical pile. Narasimha Rao et al. (1993) identified a part of the shaft carried no friction or adhesion (ineffective zone), and proposed a term H_{eff} , the effective length along which shaft friction or adhesion occurred. Zhang (1999) conducted a series of axial loading tests on instrumented helical piles in clay and sand to investigate the development of shaft skin friction or adhesion, helix bearing, and cylindrical shearing resistance, as depicted in Figure 2-2 and Figure 2-3. The pile shaft is divided into 3 segments by the strain gauges as presented in Figure 2-2 and Figure 2-3. Zhang (1999) assumed the ineffective zone (where the shaft friction or adhesion is zero) measures about D above the top helix (segment 3). However based on the load transfer mechanism results presented in Zhang (1999), Figure 2-4 (Li et al. 2016) is generated to display the friction or adhesion behavior along the shaft. The friction or adhesion in segment-3 actually accumulated in the early stage of compression loading and shrank after 3 mm of displacement as shown in Figure 2-4(a), and at the same time, segment-2 also started to lose friction or adhesion at about 3 mm (UofA) and 20 mm (Sand Pit). The segment-1 reached zero at the end, but the segment-2 has not. Thus it makes the reader confident to conclude that the ineffective zone emerges in segment-3 and grows gradually upward into segment-2 as the compression displacement increases. As a comparison, Figure 2-4(b) exhibits the friction or adhesion development subject to tension load. It shows that the friction or adhesion in segment-3 keeps increasing until failure, whereas segment-1 picks up much less friction or adhesion than that in compression. That is to say the ineffective zone in tension lies in segment-1 right below the ground surface.

The following differential Equations 2-1 for effective length in cohesive soil and 2-2 for cohesionless soil are given by Narasimha Rao et al. (1993):

$$dH_{eff} = dt / (\pi d \alpha s_u) \quad (2-1)$$

$$dH_{eff} = dt / (\pi d \delta \sigma') \quad (2-2)$$

where: t is the friction or adhesion on the shaft

d is the shaft diameter, s_u is the undrained shear strength

α is the steel-clay adhesion coefficient

σ' is the vertical effective stress

δ is the steel-sand friction factor.

The length of the ineffective zone (ineffective length) is estimated by subtracting the effective length from the embedded length of the shaft above helix.

2.2.1.2 T-z curves in sand

The behavior of the friction has been established by a lot of previous studies using experimental and theoretical methods. Coyle and Reese (1966) presented two bilinear curves for the skin friction development behavior however it is not quite applicable according to Figure 2-4. Mosher (1984) proposed Equation 2-3 to track the friction accumulated on the interface of driven prismatic pipe piles and sand. The backbone of this skin friction behavior is presented in Figure 2-5.

$$t = \frac{z}{1/k_f + z/t_{ult}} \quad (2-3)$$

where

t is the friction resistance carried by the pile-sand interface

z is the axial displacement of the pile

k_f is the initial slope of the curve presented in Figure 2-5

t_{ult} is the ultimate capacity of the friction.

The factor k_f can be determined by the internal friction angle of the sand as presented in Table 2-1 (Mosher and Dawkins, 2000). The t_{ult} can be estimated by the relative depth Z/d , where Z is the depth below ground level (BGL), and the internal friction angle of the sand after Castello (1980) using Figure 2-6. Briaud and Tucker (1984) modified the curve presented by Mosher (1984) by taking residual stresses into account using standard penetration test (SPT) results.

However, CPT was not conducted in this thesis. Although there are approaches from CPT results to relative SPT numbers in the literature, the uncertainties created in every step will accumulate to make the estimated t - z behavior untrustworthy.

Vijayvergiya (1977) proposed another curve to describe the t - z behavior following Equation 2-4:

$$\frac{t}{t_{ult}} = 2 \sqrt{\frac{z}{z_c}} - \frac{z}{z_c} \quad (2-4)$$

where

z_c is the critical axial displacement at which t_{ult} is reached.

The backbone is shown in Figure 2-7. Vijayvirgiya also provides estimated values of t_{ult} and z_c according to soil classification as presented in Table 2-2.

2.2.1.3 T-z curves in clay

Coyle and Reese (1966) normalized the shaft adhesion to t_{ult} and plotted the adhesion against the nominal axial displacement z as presented in Figure 2-8. The t - z behavior varied with the depth according to Figure 2-8. Curve I represents for the soil-pile interaction from GL to 3 m (10 ft) BGL, curve II represents for 3 m (10 ft) BGL to 6 m (20 ft) BGL, and curve III represents for the depth below 20 ft BGL. The z_{50} can be obtained from Figure 2-8 by referring to the

corresponding depth and $t/t_{ult}=0.5$. As for t_{ult} , Coyle and Reese (1966) provided Figure 2-9 to evaluate the ultimate adhesion capacity based on the undrained shear strength of clay. Tomlinson (1957) provided another curve to estimate the adhesion on the interface of steel pile and clay presented in Figure 2-10. It is easy to find that Tomlinson's evaluation is smaller than Coyle and Reese's. Vijayvergiya (1977) also indicated that Equation 2-4 is applicable for shaft adhesion in clay. The two parameters t_{ult} and z_c were recommended to be estimated by other suitable and less complex methods rather than the method presented in Vijayvergiya (1977).

Heydinger (1987) presented Equation 2-5 to simulate the t - z behavior of piles in clay using finite element and finite difference method. The finite element method assumed unconsolidated-undrained soil-pile interaction.

$$\frac{t}{t_{ult}} = \frac{\frac{E_f}{t_{ult}} \frac{z}{d}}{\left[1 + \left(\frac{E_f}{t_{ult}} \frac{z}{d} \right)^m \right]^{1/m}} \quad (2-5)$$

where

$$E_f = \frac{E_0}{\exp(0.36 + 0.38 \ln(Z/d))}$$

E_0 is the initial undrained elastic modulus of the clay, estimated to be 1,200 to 1,500 times of undrained shear strength

Z is the depth of interest

$$m = \exp(0.12 + 0.54 \ln(E_{avg} / p_a) - 0.42 \ln(Z/d))$$

E_{avg} is the average E over the entire length of the shaft

p_a is the atmosphere pressure

The curve representing Equation 2-5 is presented in Figure 2-11.

Reese and O'Neill (1987) presented a comprehensive design method for drilled shafts in sand and clay. Boulanger et al. implemented the t - z behavior as a uniaxial element for modeling the soil reaction spring of shaft friction/adhesion. Mosher (1984) and Reese and O'Neill (1987) curves were selected for t - z behavior of piles in sand and clay respectively. The following Equations 2-6 and 2-7 are used to fit these two curves:

$$t^e = C_e \cdot \frac{t_{ult}}{z_{50}} \cdot z^e \quad (2-6)$$

$$t^p = t_{ult} - (t_{ult} - t_o^p) \left[\frac{c \cdot z_{50}}{c \cdot z_{50} + |z^p - z_o^p|} \right]^n \quad (2-7)$$

where

t^e is the elastic component of the shaft friction/adhesion

t^p is the plastic component of the shaft friction/adhesion

t_o^p is the plastic component of the shaft friction/adhesion at the start of current plastic loading

$z = z^e + z^p$ is the axial displacement of the pile

z^e is the elastic component of the axial displacement

z^p is the plastic component of the axial displacement

z_o^p is the plastic component of the axial displacement at the start of current plastic loading

n is an exponent and c is a constant that define the shape of t - z^p curve together

C_e is a constant that defines the normalized stiffness of elasticity, but the value of C_e depends on n and c .

Boulanger et al. (2003) selected $c = 0.5$, $n = 1.5$, and $C_e = 0.708$ based on Reese and O'Neill (1987) for piles in clay, and $c = 0.6$, $n = 0.85$, and $C_e = 2.05$ based on Mosher (1984) for piles in sand. The results of the fitting are exhibited in Figure 2-12.

2.2.2 End bearing and uplift resistance

The current design method of the axial capacity of helical piles assumes the helical plate bearing (uplift) resistance is the same to that of a relative-size tip of conventional piles (CFEM 2006, Zhang 1999, Sakr 2009, Merifield 2011). This assumption takes advantage of the numerous experimental and theoretical studies for conventional piles as presented below.

2.2.2.1 Q-z curves in sand

Vijayvergiya (1977) presented an exponential Equation 2-8 for q - z behavior of piles in sand.

$$\frac{q}{q_{ult}} = \left(\frac{z}{z_c} \right)^{1/3} \quad (2-8)$$

Typical values of z_c given by Vijayvergiya range from 3-9 percent of the diameter of the pile end which is similar to the diameter of the helix.

Mosher (1984) proposed a similar equation to Equation 2-8:

$$\frac{q}{q_{ult}} = \left(\frac{z}{z_c} \right)^{1/N} \quad (2-9)$$

where

n accounts for the relative density of the sand, and $N = 4$ for dense sand, 3 for medium sand, and 2 for loose sand.

z_c is a nominal value of 0.25 in (6.35 mm).

The ultimate end bearing capacity is estimated by Figure 2-13 provided by Mosher (1984).

2.2.2.2 Q-z curves in clay

Aschenbrener and Olson (1984) proposed a basic elastic-plastic bilinear curve to represent the q - z behavior in clay, and suggested to use the end bearing capacity factor of clay, N_c , to estimate q_{ult} . The critical displacement was recommended to be 1 percent of the pile tip diameter. Reese

and O'Neill (1987) conducted numerous axial load tests on drilled shafts in clay and proposed a q - z curve to represent the data base, see Figure 2-14. Reese and O'Neill also recommended estimate q_{ult} using N_c , and z_{50} to be about 0.8% of the pile tip diameter.

Vijayvergiya (1977) and Reese and O'Neill (1987) curves were implemented in OpenSees for q - z behavior of piles in sand and clay respectively with details to be found in Boulanger et al. (2003). The fitting results are presented in Figure 2-14.

2.3 Lateral resistance

This section focuses on the p - y curves developed for conventional piles. The existing studies of the effect of helix on lateral capacity of helical piles are also introduced.

2.3.1 Lateral shaft resistance

2.3.1.1 P-y curves in sand

API (1993) adopted the studies of Cox et al. (1974), Reese et al. (1974), Reese and Sullivan (1980), and Murchison and O'Neill (1984) to propose a hyperbolic Equation 2-10 to fit the p - y curve in sand:

$$p = \bar{A} p_s \tanh\left(\frac{kZ}{Ap_{ult}} y\right) \quad (2-10)$$

Where

\bar{A} is an adjustment coefficient for static loading scenario, and $\bar{A} = (3.0 - 0.8 \cdot Z/d) \geq 0.9$

p_s is the smaller of p_{st} and p_{sd} , where $p_{st} = (C_1 Z + C_2 d) \gamma' Z$ is the ultimate lateral capacity due to wedge failure, and $p_{sd} = C_3 d \gamma' Z$ is the ultimate lateral capacity due to flow failure at depth,

where

$$C_1 = \frac{K_0 \tan \phi \sin \beta}{\tan(\beta - \phi) \cos(\phi/2)} + \frac{\tan^2 \beta \tan(\phi/2)}{\tan(\beta - \phi)} + K_0 \tan \beta (\tan \phi \sin \beta - \tan(\phi/2)) \quad (2-11)$$

$$C_2 = \frac{\tan \beta}{\tan(\beta - \phi)} - \tan^2(45^\circ - \frac{\gamma}{2}) \quad (2-12)$$

$$C_3 = K_0 \tan \phi \tan^4 \beta + \tan^2(45^\circ - \frac{\gamma}{2})(\tan^8 \beta - 1) \quad (2-13)$$

K_0 is the horizontal coefficient of earth pressure, which is usually chosen to be 0.4; $\beta=45^\circ+\phi/2$; ϕ is the internal friction angle of the sand; and k is the initial subgrade reaction constant. Table 2-3 presented the representative values for k , and more values based on relative density and internal friction angle can be obtained from Figure 2-15.

The curve of this hyperbolic equation is presented in Figure 2-16.

2.3.1.2 P-y curves in clay

Matlock (1970) conducted a series of lateral loading tests on instrumented piles in soft to medium clays. Matlock developed the following Equation 2-14 to represent the database:

$$\frac{p}{p_{ult}} = 0.5 \left(\frac{y}{y_{50}} \right)^{1/3} \quad (2-14)$$

where

$$y_{50} = 2.5 \varepsilon_{50} d$$

ε_{50} is the strain of the clay at half of the ultimate capacity, and typical values are presented in Table 2-4.

The ultimate lateral capacity of can be determined by the following Equations 2-15 and 2-16:

$$p_{ult} = \left(3 + \frac{\gamma'}{s_u} Z + \frac{J}{d} Z \right) s_u d \quad (2-15)$$

for wedge failure close to GL, and

$$p_{ult} = 9s_u d \quad (2-16)$$

for flow failure at depth, where

J is a constant which equals 0.5 for a soft clay and 0.25 for a medium clay. Reese and Welch (1975) suggested to use $J = 0.5$ for stiff clay above GWL.

In practice, the smaller of the two ultimate capacities is selected at the depth of interest. The p - y curve is presented in Figure 2-16. OpenSees accepted the Matlock (1970) curve and API (1993) curve to represent the p - y behavior of piles in clay and sand respectively.

2.3.2 Effects of helical plate on lateral capacity

Puri et al. (1984) conducted a series of model tests of single-helix, double-helix, and triple-helix piles subject to static lateral load in sand and proposed a mathematical relationship between lateral load and horizontal pile head deflection whereas there was no factor in this relationship accounted for the helices. Puri et al. (1984) recommended consider the effect of installation method (plain torque) based on the same evaluation procedures developed for conventional piles. Prasad and Narasimha Rao (1996) conducted model tests in soft clay and compared the ultimate lateral capacity of two types of model helical piles having 2 and 4 same helices with a single shaft (see Figure 2-17). Prasad and Narasimha Rao (1996) found the lateral capacity of the helical piles was greater than that of the single shaft and the capacity increased with the number of helices. The improvement of the lateral capacity due to the existence of helices was measured to be 20% to 50%, which makes a significant difference in the evaluation of lateral behavior (Figure 2-18). A theoretical model considering the contribution of the helix bearing (uplift) resistance and helix surface friction against the overturning was developed and validated. This model provided an idea to quantify the effect of the helix (helices).

Zhang (1999) carried out a series of in-situ lateral loading tests on four triple-helix piles in both clay and sand. The wall thickness of the pile shaft was varied to study the effect of the structural stiffness of the pile. It was found that the thicker shaft pile provides greater lateral resistance than

that of the thinner shaft pile. The effect of the helix on lateral capacities was found to be negligible due to the large embedment. A series of helical piles were instrumented by strain gauges along the length of the pile to develop load transfer distributions (see Figure 2-2 and Figure 2-3). The derived soil reaction spring displayed in Figure 2-4 can be used to estimate the ultimate capacities and half capacity displacements of relevant soil elements.

Sakr (2009) presented a study of the axial and lateral behavior of helical piles with a single helix or double helices in oil sand. The comparison of the effect of number of the helix was given and it was indicated that an additional helix did not change the lateral performance of the helical piles (see Figure 2-19). This finding might be on the account of the deep embedment of the helices.

Sakr (2009) also conducted a numerical simulation of the lateral behavior using L-pile which did not account for the helix (helices).

Elkasabgy and El Naggar (2015) performed an in-situ lateral load test of two large diameter double-helix piles. The two piles have the same lead sections but different lengths of shaft extension, which means that the embedment of helices is different. The long pile showed a higher capacity than the short pile whereas another uncertainty, the time between installation and loading, was introduced so that the cause of the difference cannot be clearly allocated.

Al-Baghdadi et al. (2015) compared the improvement of the lateral capacity of the 0.61-m-diameter helical pile due to a 2-m-diameter helix embedded at 0.5 m, 1.0 m, 1.5 m, and 2.0 m below ground level in dense sand. It was found the smaller the helix embedment, the greater the lateral capacity despite the improvement was not significant. Additionally, the lateral capacities of three different diameter piles were compared, and it was concluded the effect of the helix on the lateral capacity, was greater for small pile diameter.

In general, it can be concluded from these studies that the lateral capacity of helical piles is affected by the parameters of the helix including the diameter and embedment depth.

Table 2-1: The factor k_f values based on internal friction angle (After Mosher and Dawkins, 2000)

Internal Friction Angle (°)	k_f (kPa/mm)
28 - 31	11 - 19
32 - 34	19 - 26
35 - 38	26 - 34

Table 2-2: T_{ult} and z_c values for t - z behavior presented by Vijayvirgiya (1977)

T_{ult} (kPa)	Soil Classification	z_c (mm)
96	clean medium to dense sand	
81	silty sand	5 - 8
67	sandy silt	
48	silts	

Table 2-3: Representative values of k after API (1993)

Sand	Relative Density		
	Loose	Medium	Dense
Below GWL (MPa/m)	5.4	18.7	33.9
Above GWL (MPa/m)	6.8	24.4	61.1

Table 2-4: Representative values of ε_{50} after Matlock (1970)

Undrained shear strength (kPa)	ε_{50}
12 - 24	0.02
24 - 48	0.01
48 - 96	0.007
96 - 192	0.005
192 - 384	0.004

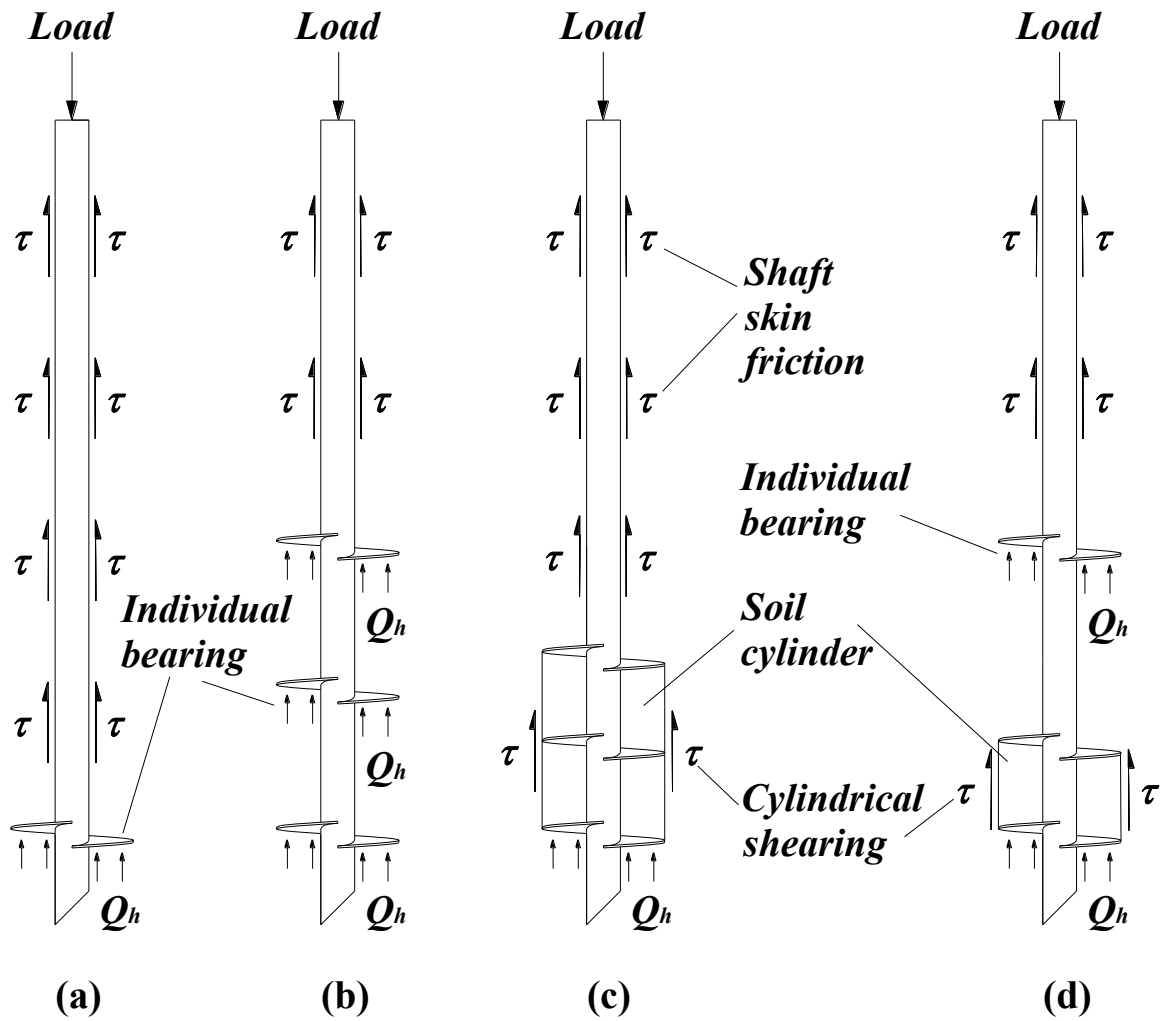


Figure 2-1: Helical pile failure models (a) individual bearing model, single-helix pile (b) individual bearing model, multi-helix pile (c) cylindrical shearing model (d) mix of two models

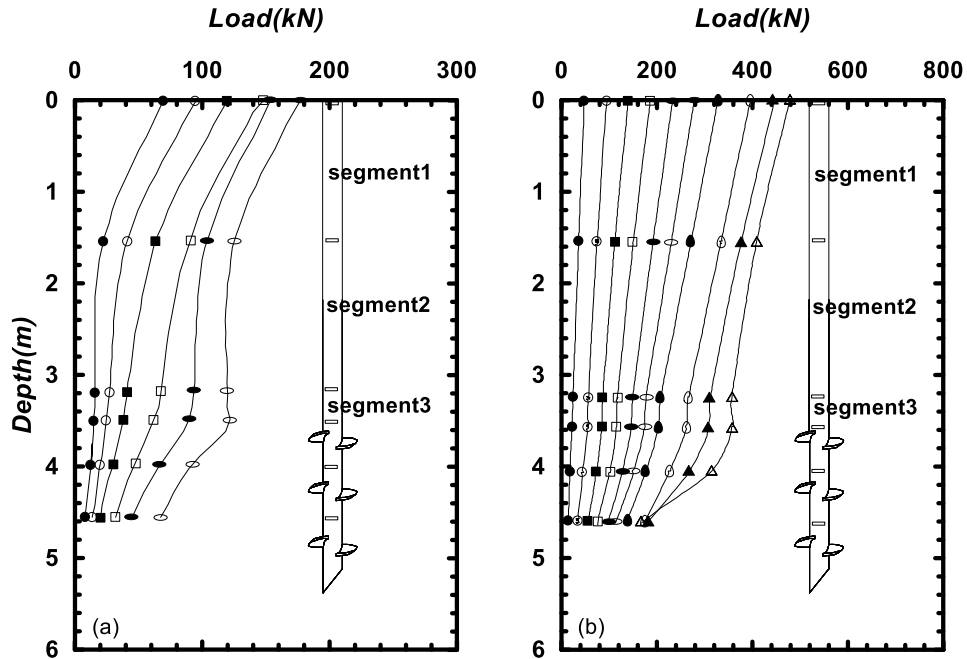


Figure 2-2: Compression load transfer mechanism: (a) UofA Farm (b) Sand Pit (After Zhang, 1999, redrawn in Li et al. 2016)

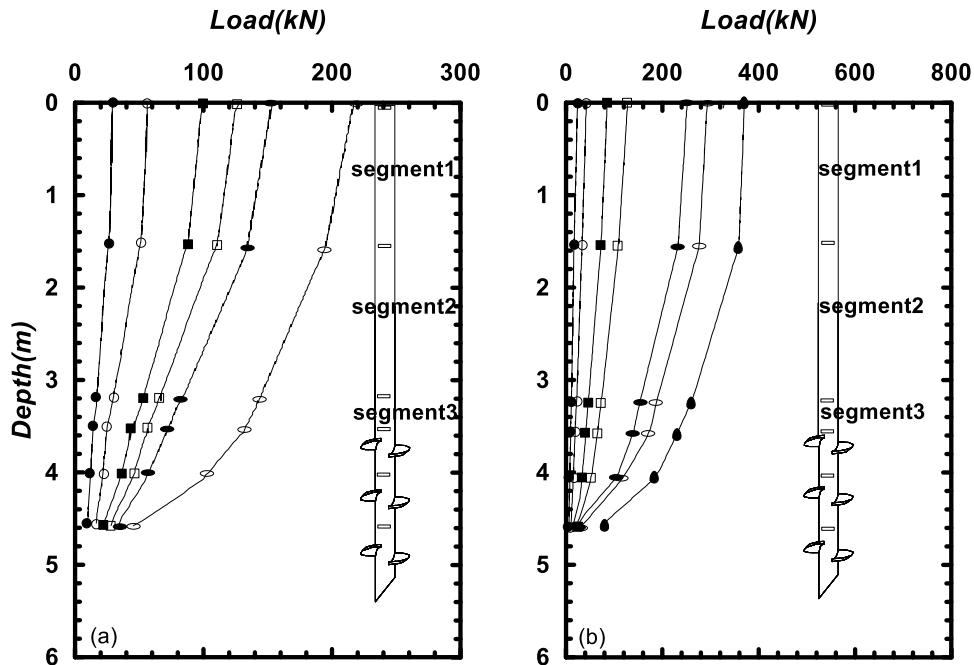


Figure 2-3: Tension load transfer mechanism: (a) UofA Farm (b) Sand Pit (After Zhang, 1999, redrawn in Li et al. 2016)

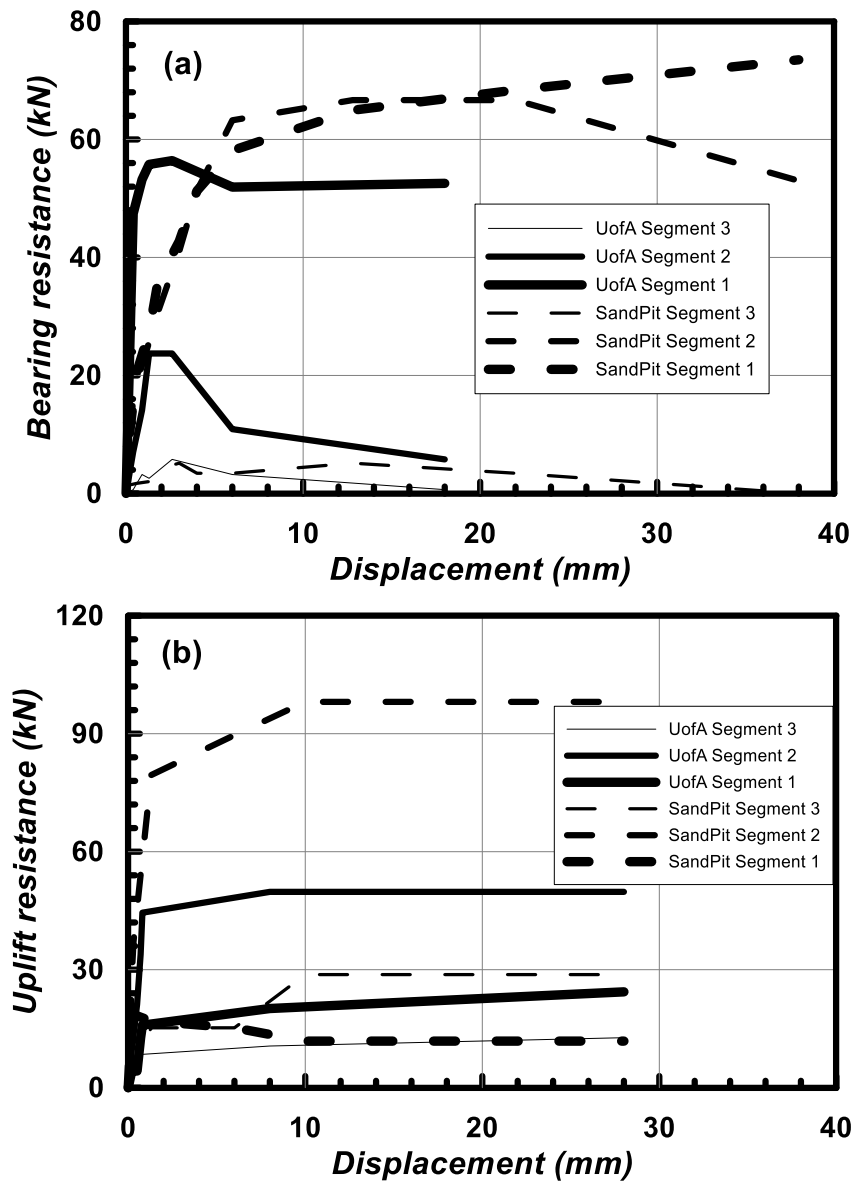


Figure 2-4: Friction or adhesion development along the shaft: (a) compression (b) tension (Li et al. 2016)

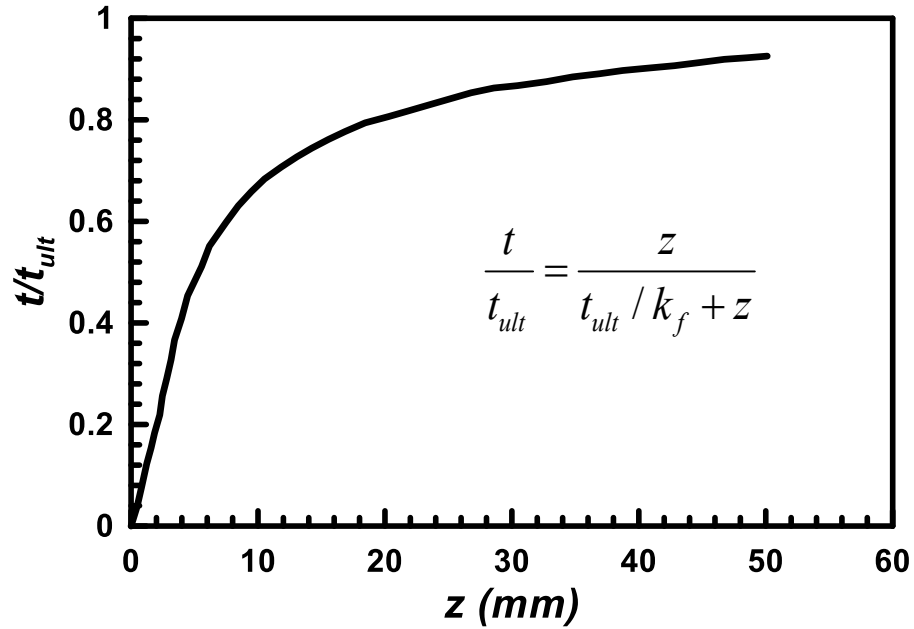


Figure 2-5: Skin friction vs. axial displacement curve of driven piles in sand (After Mosher 1984)

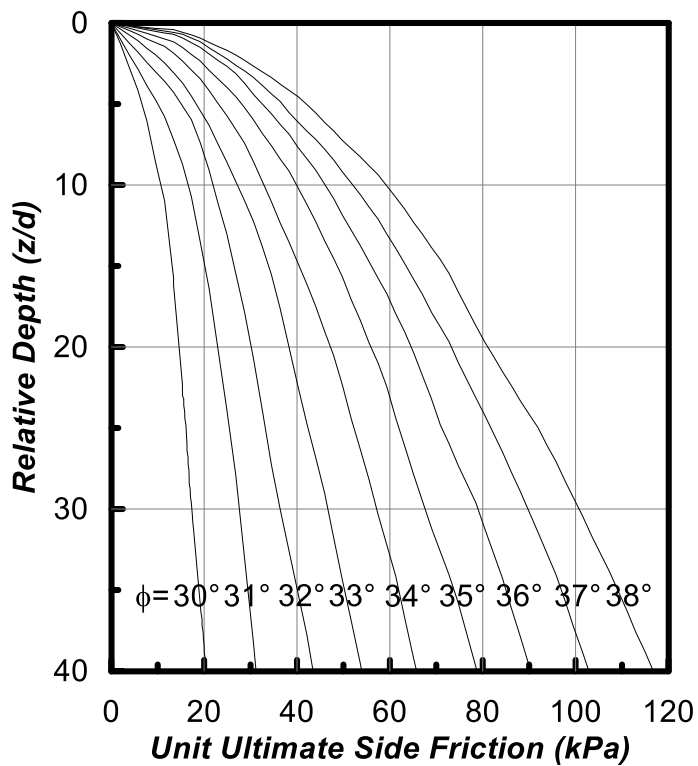


Figure 2-6: Ultimate skin friction of driven piles in sand (After Castello 1980)

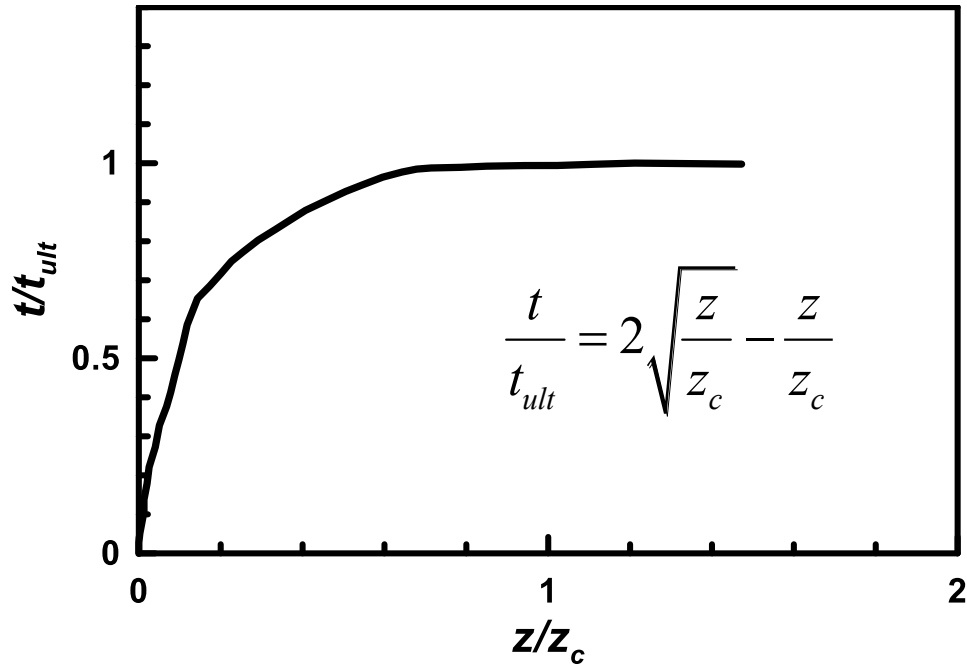


Figure 2-7: Skin friction vs. axial displacement curve of driven piles in sand (After Vijayvirgiya 1977)

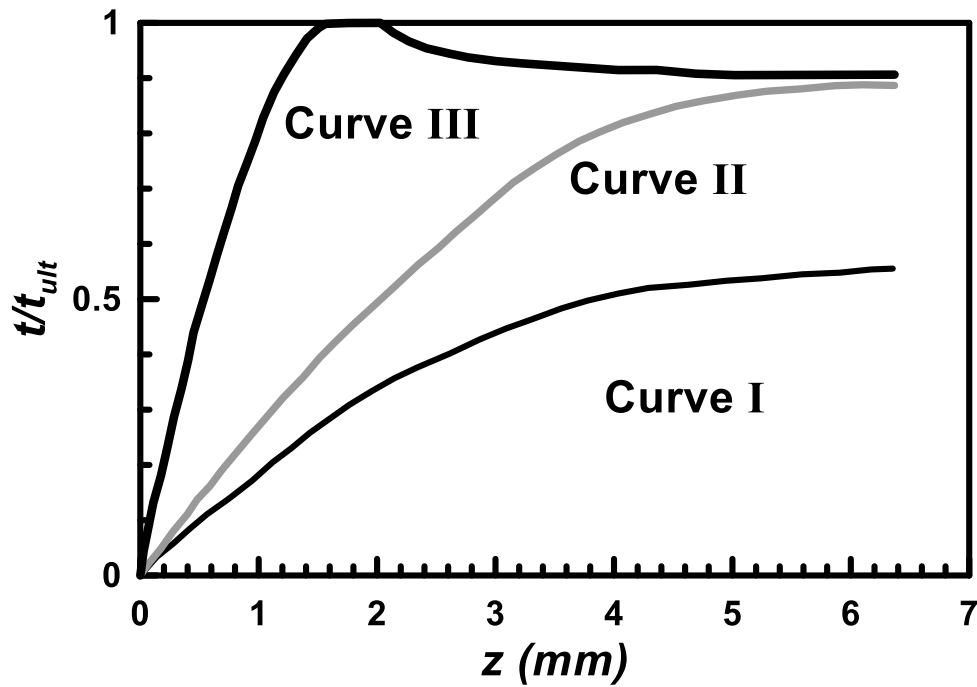


Figure 2-8: Shaft adhesion vs. axial displacement curve in clay (After Coyle and Reese 1966)

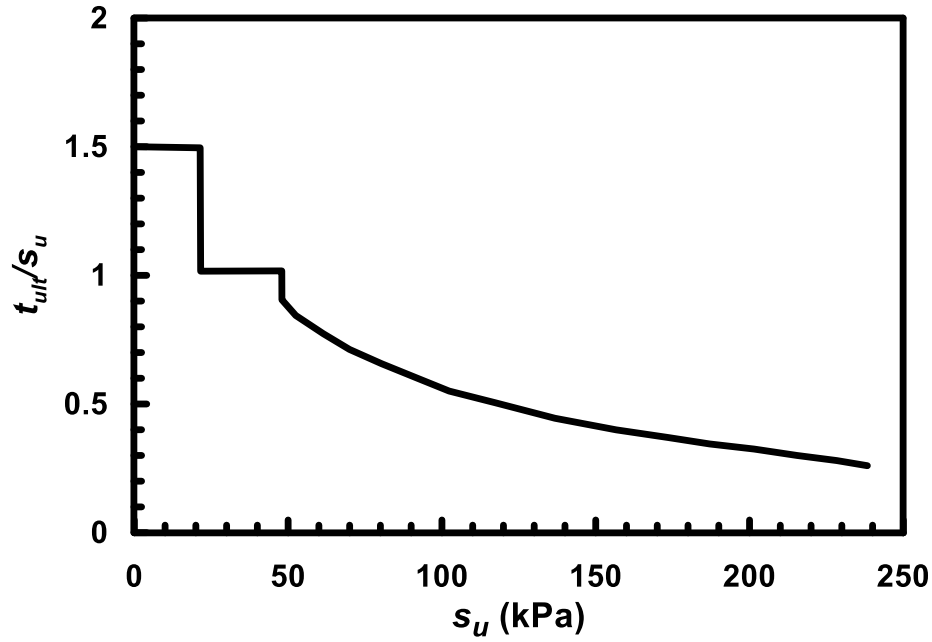


Figure 2-9: The ultimate shaft adhesion vs. undrained shear strength (After Coyle and Reese 1966)

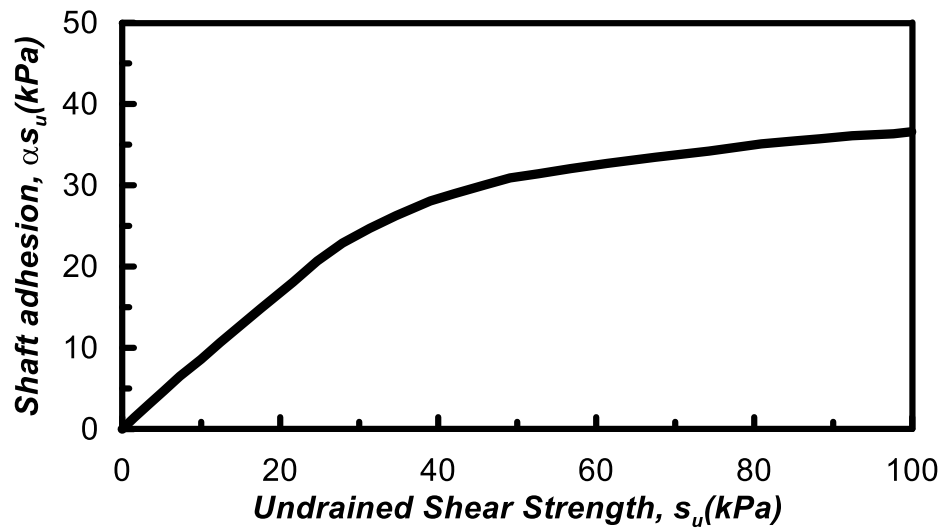


Figure 2-10: The ultimate steel shaft adhesion vs. undrained shear strength (After Tomlinson 1957)

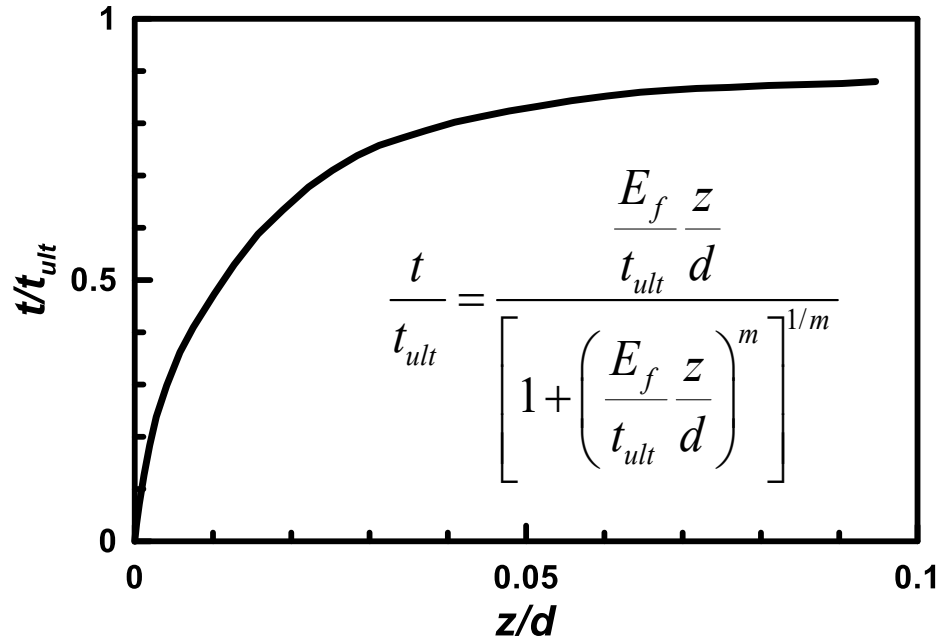


Figure 2-11: Shaft adhesion vs. axial displacement curve in clay (After Heydinger and O'Neill 1986)

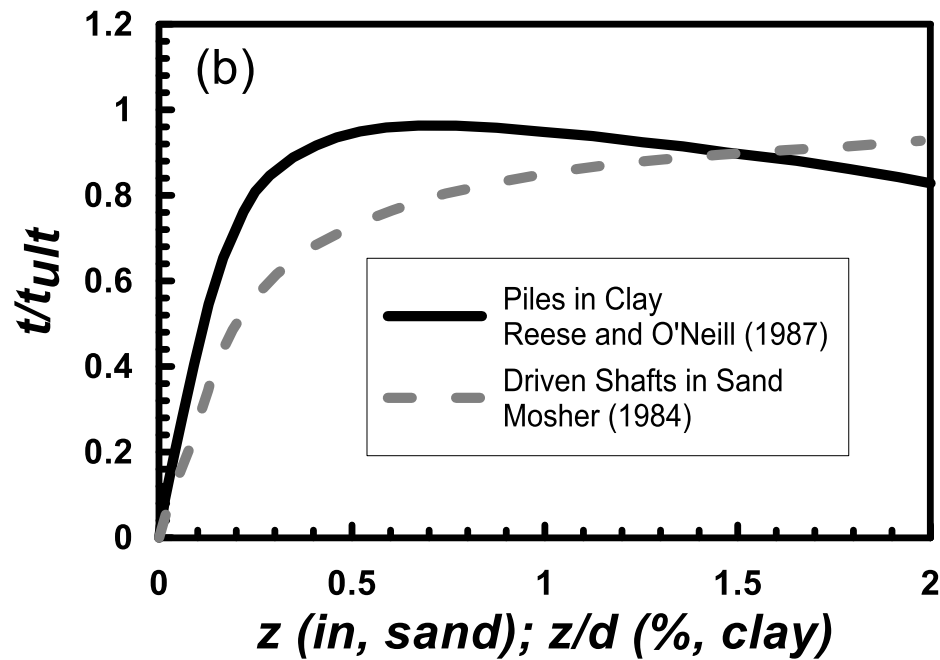


Figure 2-12: The t - z curves adopted by OpenSees (After Boulanger et al. 1999)

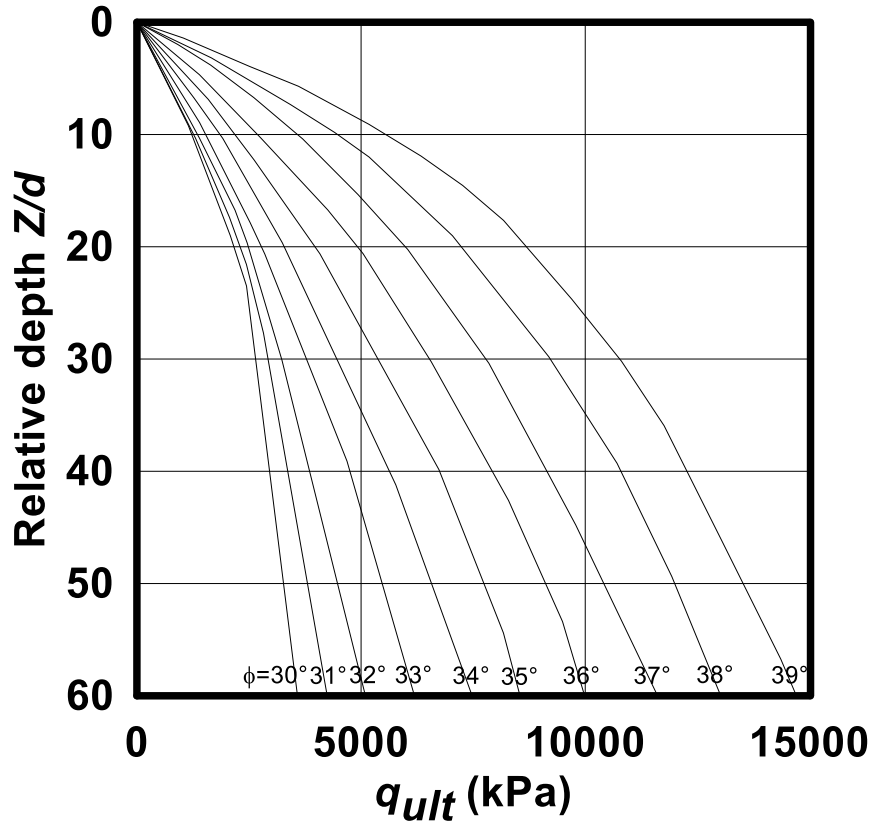


Figure 2-13. Ultimate end bearing in sand (After Mosher 1984)

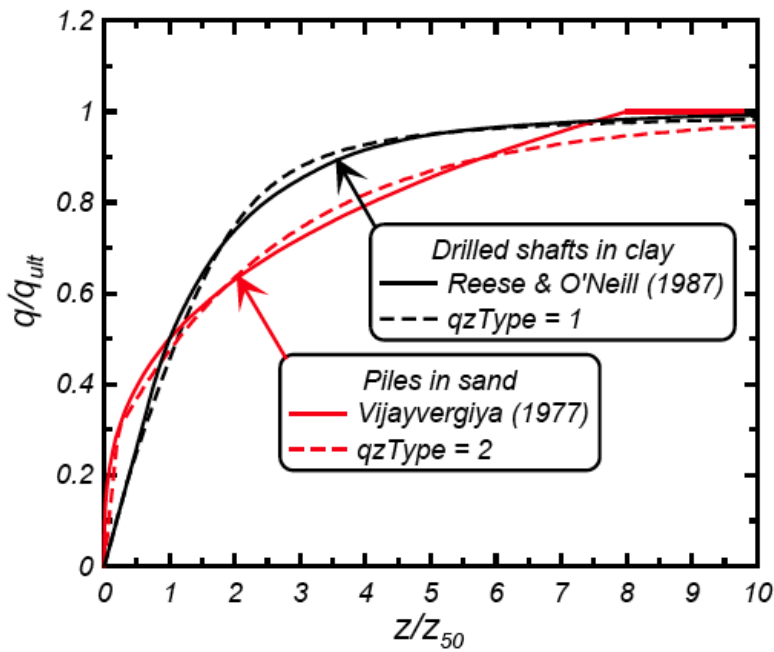


Figure 2-14: Q-z curves and the fitting curves derived by Boulanger et al. (1999)

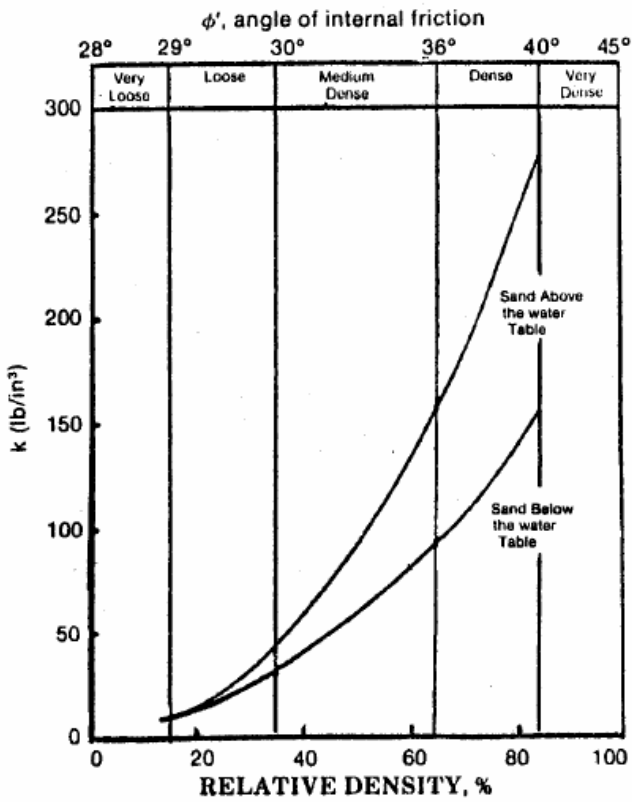


Figure 2-15: Initial subgrade reaction constant (After API, 1993)

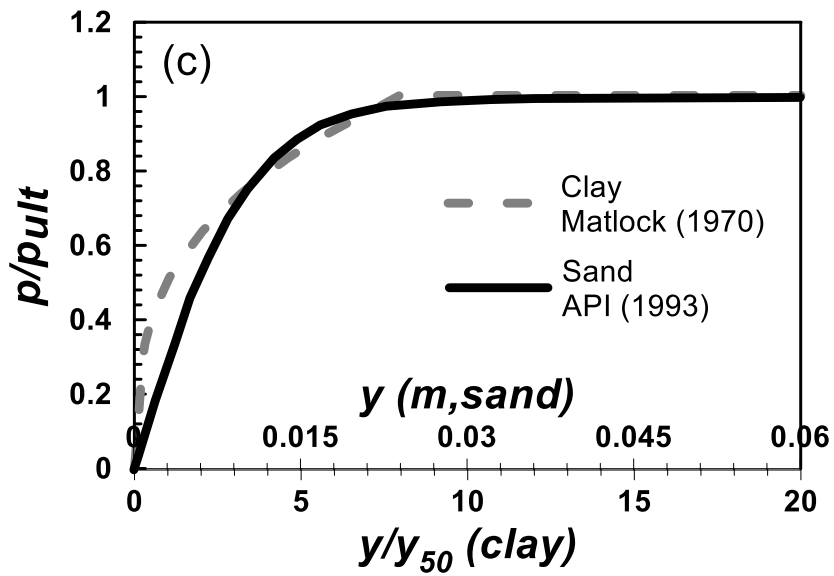


Figure 2-16: P-y curve in sand (After API, 1993) and clay (After Matlock, 1970)

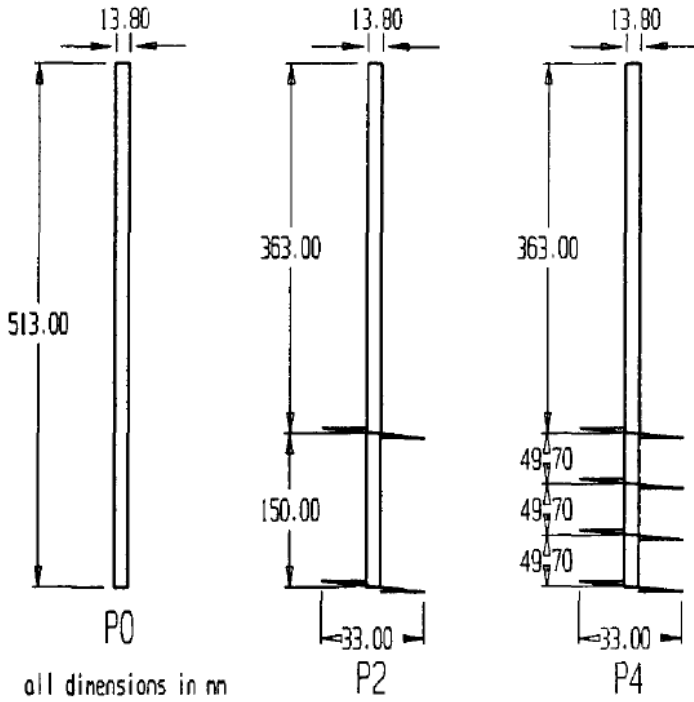


Figure 2-17: Model piles used to test the effect of helical plate(s) on lateral capacity of helical piles (Prasad and Narasimha Rao, 1996)

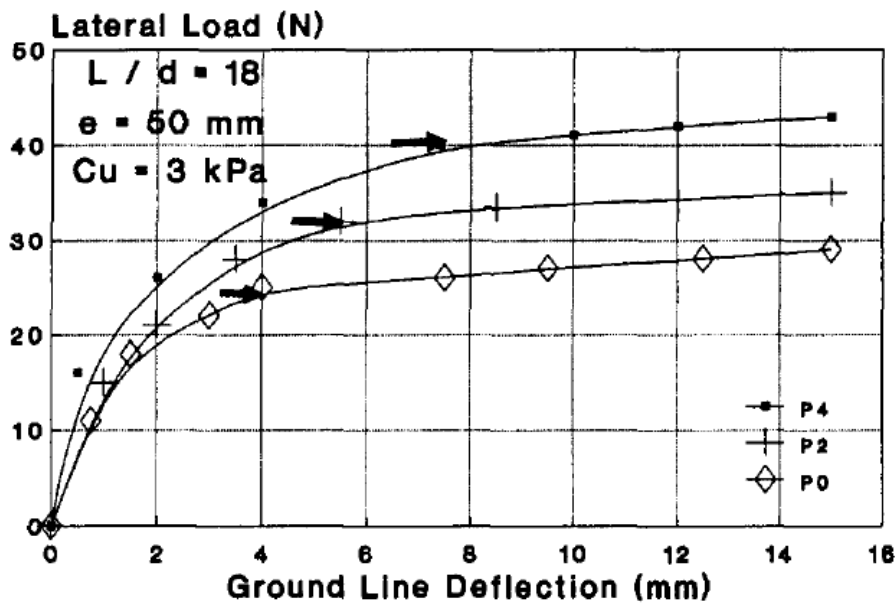


Figure 2-18: Lateral load vs. deflection of the three types of piles as shown in Figure 2-17 (Prasad and Narasimha Rao, 1996)

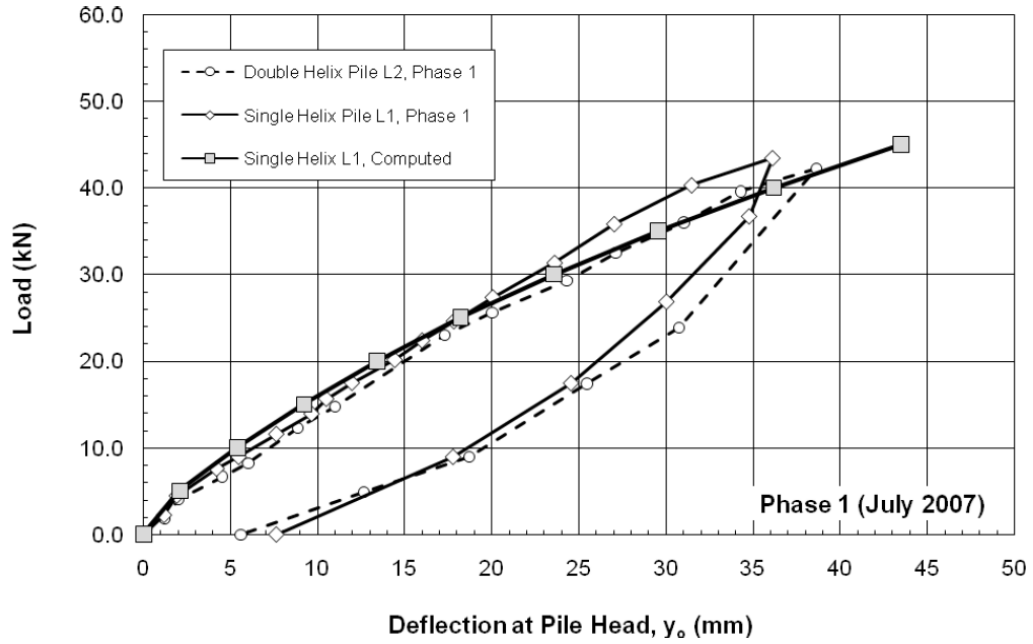


Figure 2-19: Lateral load vs. deflection of two relevant double-helix and single-helix piles (Sakr 2009)

3 Field Testing and Numerical Modeling of Axial Behavior of Single-helix Piles¹

Abstract

Helical piles are widely used in Western Canada for many engineering applications as an alternative of conventional piles. Pile-specific torque-capacity correlations are normally required for the design of a helical pile. This chapter presents the results of the axial compression and tension tests of three types of round shaft single-helix piles installed in cohesive and cohesionless soils located in Alberta, Canada. Twenty-six axial static load tests in total were conducted, including 15 compression and 11 tension tests. The torque-capacity correlations were established using the torques measured during the installation. It was found that the torque-capacity correlation was not perfectly linear; the axial capacity/torque ratio decreased at the higher installation torque. Seven CPT tests were conducted in the field, 4 in the cohesive soil and 3 in the cohesionless soil, to evaluate the subsurface soil properties. Numerical modeling was conducted using BNWF method on the platform of OpenSees to simulate the axial behavior of these helical piles. The soil strength parameters based on the CPT results were used as the input to the soil reaction springs of the numerical model. The results indicate that the BNWF method can properly simulate the load-displacement behavior of single-helix piles.

3.1 Introduction

Twenty-six small-diameter helical piles were installed and tested in two types of soils, namely the medium to stiff clay and medium to dense sand, in Western Canada, including 15 axial compressive tests and 11 axial tensile tests. Three CPT tests were carried out in the cohesive site on the farm of University of Alberta, and another four CPT tests were conducted in the

¹ Part of this chapter is published in Li et al. (2015) and Li and Deng (2015)

cohesionless site in a sand pit in Bruderheim, Alberta. All CPT boreholes were extended to more than 7 m below ground level which is sufficiently greater than all of the installation depths up to 4.3 m. The axial capacities were observed from the load tests results and correlated to the installation torques recorded during the pile installation. Additionally, a BNWF model was described and developed in this chapter to simulate the axial behavior of the helical piles tested in this project. The computed load-displacement curves were calibrated by the load tests results. The first objective of the present study is to understand the behavior of three types of small-diameter single-helix piles in cohesive and cohesionless soils subject to axial static loading. Theoretical methods and empirical methods mentioned in the literature were used to estimate the axial pile capacities. The second objective of the present study is to investigate the feasibility of BNWF method in simulating soil- helical pile interaction in axial direction. The specific tasks are to: (i) evaluate axial capacities of single-helix piles, (ii) correlate axial capacities to installation torques, (iii) simulate the behavior of single-helix piles under static axial loadings using a BNWF model on OpenSees platform, and (iv) evaluate the efficiency and reliability of CPT-based method of estimating soil parameters for numerical modeling.

3.2 Subsurface investigation

The research program selected two sites (see Figure 3-1) for load tests. Site 1 at the University Farm is located in central Edmonton, Alberta, Canada. Site 2 at the Sand Pit is located about 7.5 km north to Bruderheim, Alberta, Canada. Overall, Site 1 soil is cohesive and Site 2 is cohesionless.

CPT tests were performed to a minimum depth of 7.0 m, which covers the longest test piles in length, to develop the soil profile. The layout of the CPT boreholes is presented in Figure 3-2. The CPT results (see Figure 3-3 Figure 3-4) show that at Site 1, the top 5.0 m layer consists of

uniform clay, underlain by interbedded silty clay and clayey silt from 5.0 m to 7.0 m. The ground water table is 4.8 m below ground level, and the negative pore pressure above the ground water table indicates that the clay soil in the upper layers is saturated maybe due to capillary suction.

At Site 2, the top soils are interbedded clean sand and silty sand to a depth of 4.4 m, underlain by clayey silt to silty clay from 4.4 m to 5.6 m, underlain by a mixture of sand to silty sand from 5.6 m to 6.2 m; below 6.2 m, the soil is a mixture of silty clay to clay. Overall, the soil strength exhibits a decreasing trend against the depth. The ground water table is 3.0 m BGL.

The soil profiles based on CPT results and the correlations after Robertson and Cabal (2012) are presented in Figure 3-3 and Figure 3-4. The two critical parameters, namely the undrained shear strength s_u and the internal friction angle ϕ' , were estimated using Equations 3-1 and 3-2:

$$s_u = \frac{q_t - \sigma_v}{N_{kt}} \quad (3-1)$$

$$\tan \phi' = \frac{1}{2.68} \left[\log\left(\frac{q_c}{\sigma'_{vo}}\right) + 0.29 \right] \quad (3-2)$$

where N_{kt} is the cone factor, q_t is the corrected cone resistance, and σ'_{vo} is vertical effective stress.

N_{kt} was selected to be 15 which is the median of the recommended values by Robertson and Cabal (2012).

The interpretation of CPT results took account of results of laboratory soil tests conducted by Bhanot (1968). Thinner solid straight lines implemented in the profile of the soil strength parameters in Figure 3-3 are used as the upper limit of the corresponding soil type (Robertson and Cabal, 2012). The soil type, the undrained shear strength, and internal friction angle are included in the profiles.

3.3 Field testing program

3.3.1 Pile installation

Figure 3-5 describes the installation of a helical pile. The installation equipment consists of an excavator, a driving head, and a leveling rod. The driving head generates a plain torque and acts on the head of the helical pile so that the helix can penetrate the ground. The advancing rate is controlled by the driving head and an axial load (named crowding load) from the excavator may be exerted if necessary to maintain about one pitch advancement per revolution. During the downward penetration, a leveling rod may be used to correct the orientation of the pile. In general, only two operators are required to finish the installation within 30 min for large piles and 5 min for small piles.

During the installation, when the helix blade is penetrating the ground, the soil is disturbed resulting in an uncertainty of the ultimate capacity prediction. To minimize the soil disturbance, the leading edge of helix is sharpened, the helix radius is fabricated to be right angled to the shaft (known as true helix, Figure 3-6), the advancing rate of the installation is controlled to be one pitch (the length from the starting point to the ending point of the helix along the shaft) per revolution, and the spacing should be casted in increments of the pitch to make sure that all the successive helices follow the path created by the leading helix.

3.3.2 Pile dimensions and set-up

The test program considered three types of piles with shaft diameters ranging from 7.3 cm to 11.4 cm, helix diameters ranging from 0.305 m to 0.406 m, and pile lengths ranging from 2.44 m to 4.57 m. The thickness of the pipe wall of all three types is 7.8 mm. The detailed pile dimensions and sketches are shown in Table 3-1 and Figure 1-1, respectively. The piles are screwed into the ground by a plain torque applied to the pile head and the advancing rate is about

one pitch per revolution to minimize the soil disturbance. One-foot long pile shaft is left above the ground surface to allow for testing equipment set-up. A pile cap with two opposite hooks is welded to the head of every testing pile to fit the axially loaded hydraulic jack. The hooks are constructed in case of uniaxial rotation due to the lack of resisting moment about the pipe axis.

3.3.3 Load reaction system

Two test frames are established for compression and tension tests independently. The test frame consists of a reaction system, a loading system, a measuring system, and the testing pile. Except for the loading system, all the three parts of the test frame are the same for compression and tension tests.

The reaction system includes two big reaction piles and an H-shaped reaction beam sitting on the top of the reaction piles as shown in Figure 3-7 for compression and Figure 3-8 for tension.

Every reaction pile is 6.9 m long and 0.32 m in diameter. The bearing capacity of the reaction beam is 350 ton when the point load is applied to the center of it. According to the test frame design, the setup of the loading system is presented in Figure 3-9 and Figure 3-10.

The measuring system consists of two parallel reference beams, two linear variable differential transformers (LVDT), and two dial gauges. The four ends of the two reference beams are placed on four sand bags so that the elevation and angle of the beams can be adjusted by the deformation of sand bags. The above surfaces of the beams are adjusted to level so that the LVDTs and dial gauges can rest their needles on. The bodies of the LVDTs and dial gauges are attached to the cap of the testing pile via magnetic bases to measure the displacement of the testing pile. The readings of the LVDTs are used as the results and the readings of the dial gauges are for backup.

The loading system for compression tests consists of a load cell seated on a hydraulic jack. These two devices are aligned with the axis of the testing pile and the center of the reaction. Proper amounts of steel plates are placed on top of the load cell to make contact. The loading system for tension tests involves an additional retaining cap, several retaining nuts, and four connecting rods to transfer the tension load from the hydraulic jack sitting on the top of the reaction beam to the testing pile right under.

3.3.4 Testing Procedure

The compression load tests were conducted according to ASTM D1143 / D1143M - 07(2013), and the tension tests according to ASTM D3689 / D3689M - 07(2013). Specifically, the testing procedures include three parts: axial capacity prediction, load increment and time interval design, and load tests with measurements. To allow for the soil setup (i.e. the soil undrained strength recovers from being disturbed), at the clay site we waited for three weeks after installing the helical piles although one week waiting period is typically sufficient for soil setup. At sandy site, we did not wait for long because the soil setup in sand was not considerably important.

The limit compression and tension capacities of the helical piles were estimated from the final installation torques using the torque factor method (Hoyt and Clemence, 1989). The nominal value of K_t for preliminary capacity prediction was adopted as 33 m^{-1} for compression piles and 26 m^{-1} for tension piles.

For all of the axial load tests, each pile was loaded to ultimate failure at an increment of 5% of the predicted limit capacity. Constant time interval of 5 min was adopted to allow adequate time for pile mobilizing and data reading. Load increments were added until “failure” defined as the pile settlement reached 10% of the helix diameter. This maximum load was suspended for 15

min and then the unloading was started. Unloading stages adopted a decrement at 25% of the maximum load and the constant time interval increased to 10 min.

3.4 Tests results

3.4.1 Load vs. Displacement Curves

Twenty-six axial load-displacement curves are obtained from the axial compression and tension tests as depicted in Figure 3-11 and Figure 3-12. The ultimate axial capacity is interpreted from the load-displacement curves at the displacement corresponding to 10% of the helix diameter (see Figure 3-13), since the 10% criterion is one of most common use for practical design of deep foundations. The ultimate capacities are listed in Table 3-2.

Figure 3-11 shows that for Site 1 (medium to stiff clay), the limit state is reached since excessive displacement has been observed. All the load-displacement curves consist of a relatively steeper initial linear portion, a nonlinear and relatively milder uptrend following, a plateau part trailing, and an unloading segment descending with a similar slope as the initial linear boost. All the ultimate capacities indicated by the 10% criterion are located in the plateau segments of the load-displacement curves. It is also noticed that the compression capacity is greater than the tension capacity for each type of piles.

For Site 2 (silt to sand) as depicted in Figure 3-12, the limit state has not been reached because the plateau is not observed except for the compression tests of the longest pile P3. All the ultimate capacities are mobilized at the end of nonlinear segments and the compression capacity is greater than the tension capacity except for the compression tests of P3. The reason why the compression tests of P3 are exceptional may be the existence of the clay layer deposited at the depth of 4.2 m, which is right beneath the helix of P3 embedded at 4 m depth. According to the CPT profile provided in Figure 3-4, the cone tip resistance in the underlying clay layer is much

smaller than that in the sand at 4 m dept. Therefore the plunging failure zone created beneath the helix extended into the underlying weaker clay soil, and caused the reduction of the bearing capacity than expected (Meyerhof 1974).

The curvature of the nonlinear region of Site 1 is greater than that of Site 2 which indicates that the transition from the elastic state to plastic state of cohesive soil is shorter than that of cohesionless soil.

3.4.2 Torque factor analysis

Hoyt and Clemence (1989) proposed a simple relationship between final installation torque and ultimate pile capacity (Equation 3-3):

$$Q_u = K_t T \quad (3-3)$$

where K_t is the torque factor and T is the final installation torque.

The torque factor may range from 5 m^{-1} to 15 m^{-1} depending on the pile shaft geometries and loading directions. Although there is a lack of theory behind the torque method, Equation 3-3 is one of the most common design method used by the helical pile industry. A vital defect of this method is that a potential weak layer underlying the pile tip, which is extremely dangerous to axial pile capacity, is not reflected in the installation torque. To avoid this defect, a CPT profile which extends to a greater depth than the helical pile embedment may be used in the design.

The torque factors were estimated from the test results and presented in Figure 3-14. Torque factors were classified by pile types and loading direction. Generally, the torque factors for tension capacity were smaller than the torque factors for compression capacity. For Type 1 piles, the torque factors decreased when the installation torque increases. For instance, the torque factor of Type 1 pile subject to compressive loading decreased from 36 m^{-1} to 25 m^{-1} when the installation torque increased from $1500 \text{ N}\cdot\text{m}$ up to $4000 \text{ N}\cdot\text{m}$. But for the Type 2 and Type 3

piles, the measured pile capacities showed an approximately linear and constant relation to the corresponding installation torques. Additionally, the biggest Type 3 piles had much smaller torque factors than that of Type 1 and Type 2 piles.

3.5 Development of numerical models

The BNWF method is adopted to develop the numerical models in OpenSees to simulate the axial behavior of these helical piles. The numerical model consists of an elastic shaft and three sets of soil elements including the p - y (PySimple1), t - z (TzSimple1), and q - z (QzSimple1) springs. The pile shaft below ground surface and above helical plate is divided into certain numbers of 2 cm segments with a pile node at each demarcation point. Each pile node is connected to a fixed node via a corresponding spring. Three equally divided segments subject to vertical bearing or uplift load represented by three q - z springs are assigned on each side. All the pile segments are modeled by elastic uniaxial steel material since the pile shaft is far from being yielded during the axial load testing. The length of pile shaft below helical plate is neglected in the modeling as ineffective length (Narasimha Rao et al. 1991, Zhang 1999), which does not contribute to the skin friction resistance. According to the analysis in Section 2.1.1.1, the ineffective zone grows with the increasing pile displacement but further details remain unknown so that the ineffective zones are not considered in the numerical model development. Figure 3-15 shows a sketch of the axially loaded helical pile BNWF model. Although the load is axial and one-dimensional, the p - y springs are necessary to provide proper constraint. However the stiffness and ultimate capacity of the p - y spring in this model does not have to be exactly assigned since no lateral displacement is expected after all.

The wall thickness of the pile shaft, a circular steel pipe, was 7.8 mm. The deformation of the steel pipe during axial loading tests was negligible compared to the pile settlement so that the steel pipe elements are assigned to be elastic with a Young's modulus of 200 GPa.

All the three types of soil springs require two parameters, namely the ultimate capacity and the displacement at half capacity, to be determined. Considering the soil types and the ground water level, the following methods are adopted to generate the best estimation of the ultimate capacity (t_{ult} , q_{ult} , or p_{ult}) and the displacement at half capacity (z_{50} or y_{50}), see

Table 3-3.

3.6 Numerical simulation results

The undrained shear strength and friction angle profiles at the testing sites obtained from the CPT logs were used as the input to the parameters of the numerical model. The parameters of each spring material were generated from the CPT input using the approaches summarized in the previous section and adjusted to calibrate the load test results. Four typical load-displacement curves corresponding to different soil conditions and different loading directions were presented in Figure 3-16.

The BNWF numerical model was calibrated against the four selected load-displacement testing.

The following points could be observed from the comparisons in Figure 3-16.

- i. The selected load-displacement curves are consistent with results of the BNWF modeling in OpenSees, although the stiff clay condition at Site1 was simulated by soil reaction spring for soft clay which is the only soil type available in OpenSees.
- ii. The stiffness of the elastic portion of the load-displacement curves obtained from clay soil was underestimated by computation, especially when compared to the rest simulations for sand. The underestimation was likely due to the original fitting of the backbone for q - z

spring material. The backbone curve summarized from soft clay was not fully capable of simulating the tests in stiff clay.

- iii. The compression test calibration had a better agreement than tension test calibration in the early unloading phase. Despite the wild end of unloading, the pile resistance against compression had a higher initial stiffness during unloading. The most suspicious cause was vertical earth pressure acting on the helix to make it easier to settle (unloading tension) and harder to bounce (unloading compression).
- iv. A considerable deviation of each unloading curve, obtained from both numerical modeling and test results, was observed. To explain this deviation, one of the calculated curves is decomposed into q - z spring response and the resultant of all t - z springs' response presented in Figure 3-17. It is seen from Figure 3-17 that q - z spring (helical plate bearing) has a steeper unloading slope and greater residual displacement than the resultant of all t - z springs (the total skin friction). At the meantime, another character is observed that the resultant of t - z springs are not mobilized to ultimate limit state until about 50 mm displacement, which is much greater than the displacement for q - z spring to mobilize to ultimate limit state. In fact, the critical displacement of skin friction or adhesion should not be much larger than that of end bearing. Recalling the development of the numerical models, the ineffective zones were neglected which means the number of the t - z springs were overestimated so that the stiffness (determined by the input z_{50}) of t - z springs were underestimated (z_{50} was overestimated) to calibrate the load-displacement test results.
- v. Since the half capacity displacements of the q - z springs were selected from two recommended ranges based on the critical displacement z_c , a sensitivity analysis was conducted using the upper bound and lower bound of these two parameters. As shown in

Figure 3-18, z_{50q} equals 5% and 20% of z_c were selected for the clay of Site 1, and z_c of 3% and 9% of helix diameter were selected for the sand of Site 2. It was found z_{50q} has greater influence on the simulation results for cohesionless soil than that of cohesive soil.

3.7 Conclusions

The axial load-displacement behaviors of 26 single-helix piles installed in Western Canada were obtained from static loading tests in cohesive and cohesionless soils. The sites were characterized by CPT logs. A numerical model was developed using the BNWF method in OpenSees framework to simulate the behavior of three types of single-helix piles subject to axial compression or tension load. The following conclusions may be drawn.

- i. The helical piles exhibited two different load-displacement behaviors in cohesive and cohesionless soils. The ultimate capacities indicated by the 10% criterion are located in the plateau segments of the load-displacement curves for cohesion soil. However for the cohesionless soil, the ultimate capacities are mobilized at the end of nonlinear segment before the plateau segments. The transition from the elastic state to plastic state of cohesive soil takes less displacement than that of cohesionless soil.
- ii. A series of torque factors were proposed for the piles tested. The torque factors were found to vary with helical pile dimensions and loading directions. Generally, the bigger pile had a smaller torque factor, and the torque factor for tension capacity was smaller than that of compression. Torque factor method is not safe when an underlying weak layer exists. A soil strength profile extending to a sufficiently greater depth than the pile embedment is necessary to clarify the effect of potential underlying weak layers, or a trial load should be conducted after installation.

- iii. The BNWF method in OpenSees framework is capable of producing high quality simulation for the single-helix pile under axial static loading even though the soil types implemented in OpenSees are not sufficient yet.
- iv. The simulation can be improved if the behavior of the ineffective zones is verified. The influence of ineffective zones on the axial capacity prediction of helical piles is significant and should not be ignored.
- v. The CPT based method of selecting soil reaction spring parameters of the numerical models in OpenSees is efficient and effective.
- vi. The half capacity displacement of q - z springs z_{50q} has greater influence on the simulation results for cohesionless soil than that of cohesive soil.

Table 3-1. Test pile geometries

Pile Type	L (m)	d (cm)	D (m)	H (m)	P (cm)
1	2.44	7.3	0.305	1.83	7.6
2	3.05	8.9	0.356	2.44	7.6
3	4.57	11.4	0.406	3.96	7.6

Table 3-2: Axial ultimate capacities

Pile Type	Site Code	Compression/ Tension	Measured Capacities/kN
1	1	C	52,56,48
		T	48,44
	2	C	104,96
		T	80,73
	3	C	256
		T	160
2	1	C	75,70,73,72
		T	84,76
	2	C	126,134
		T	108,93
	3	C	254
		T	269
3	1	C	112,110
		T	100
	2	C	128,114
		T	178,164
	3	C	468
		T	329

Table 3-3: The estimation of parameters of the numerical model for axial loading

	Site 1, clay	Site 2, sand
p_{ult}	-	-
γ_{50}	-	-
q_{ult}	$q_{ult} = 9.0s_u$	$q_{ult} = N_q \sigma'$ Meyerhof (1976)
z_{50q}	$z_{50q} < z_c = 1\%D$ Aschenbrener and Olson (1984)	$z_{50q} < z_c = (3-9\%)D$ Vijayvirgya (1977)
t_{ult}	Figure 2-9 Coyle and Reese (1966)	Figure 2-6 Castello (1980)
z_{50t}	Figure 2-8 Coyle and Reese (1966)	Figure 2-12 Mosher (1984)

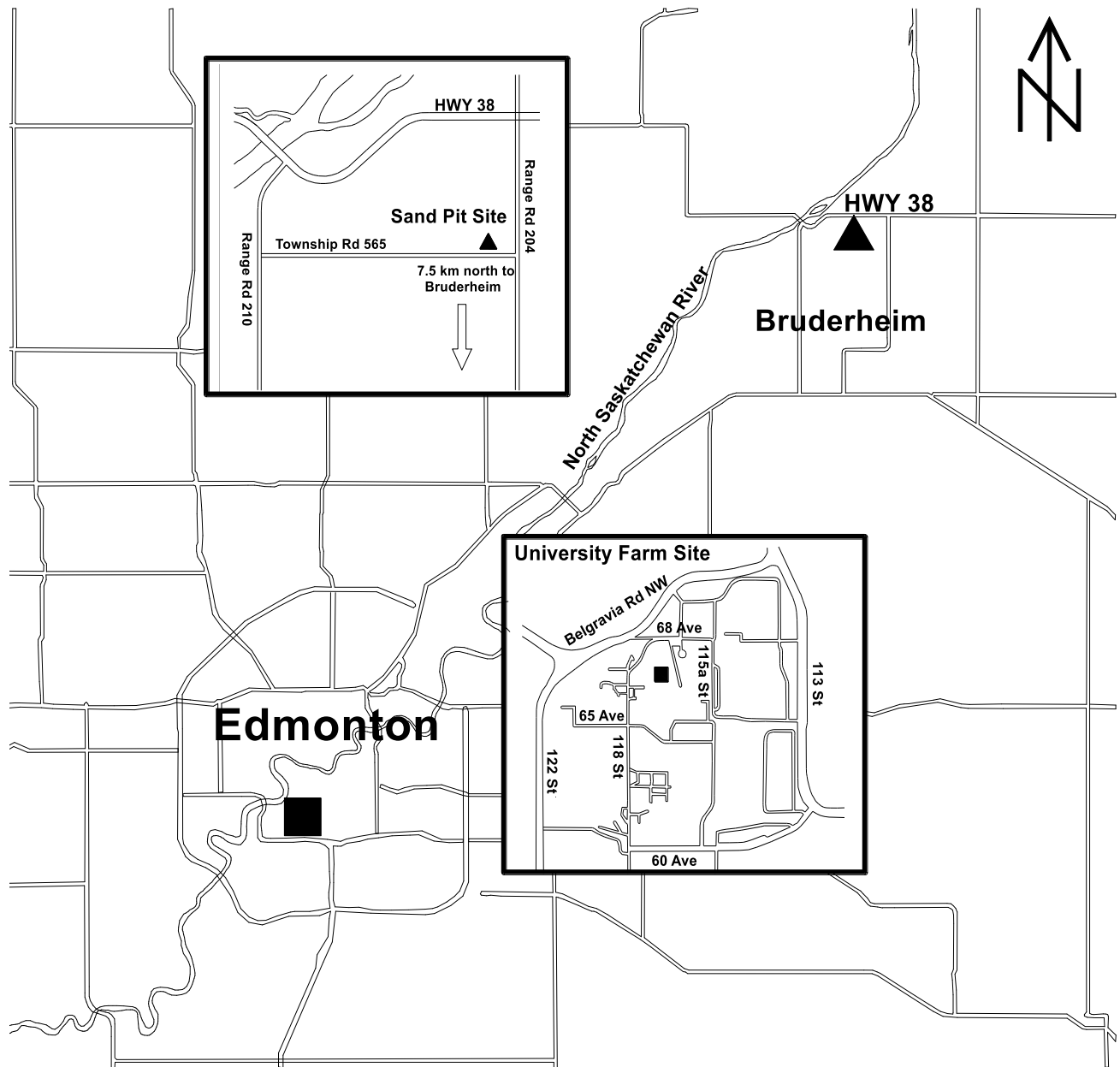


Figure 3-1: Locations of two test sites

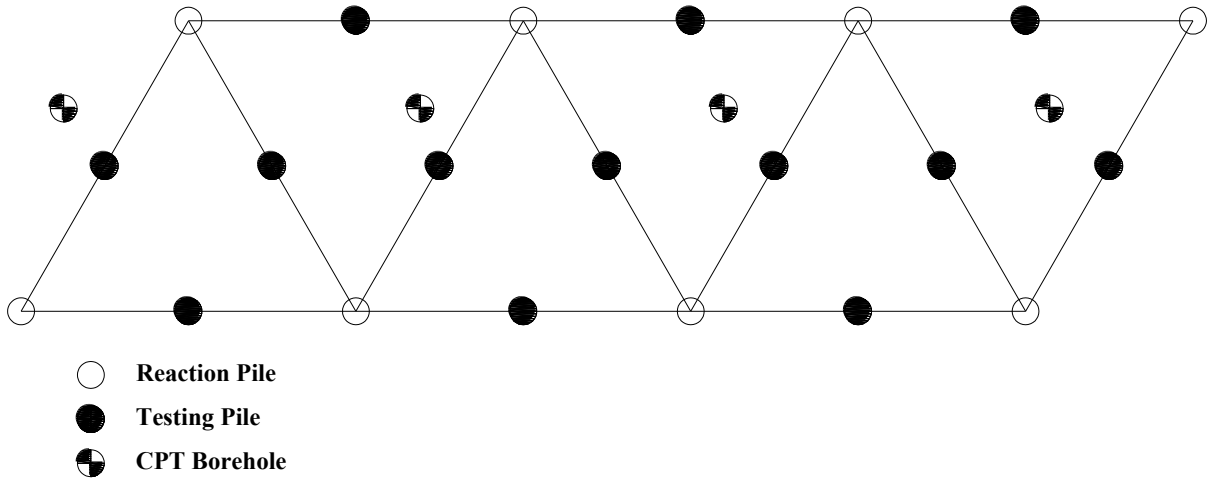


Figure 3-2: Layout of the piles and CPT boreholes

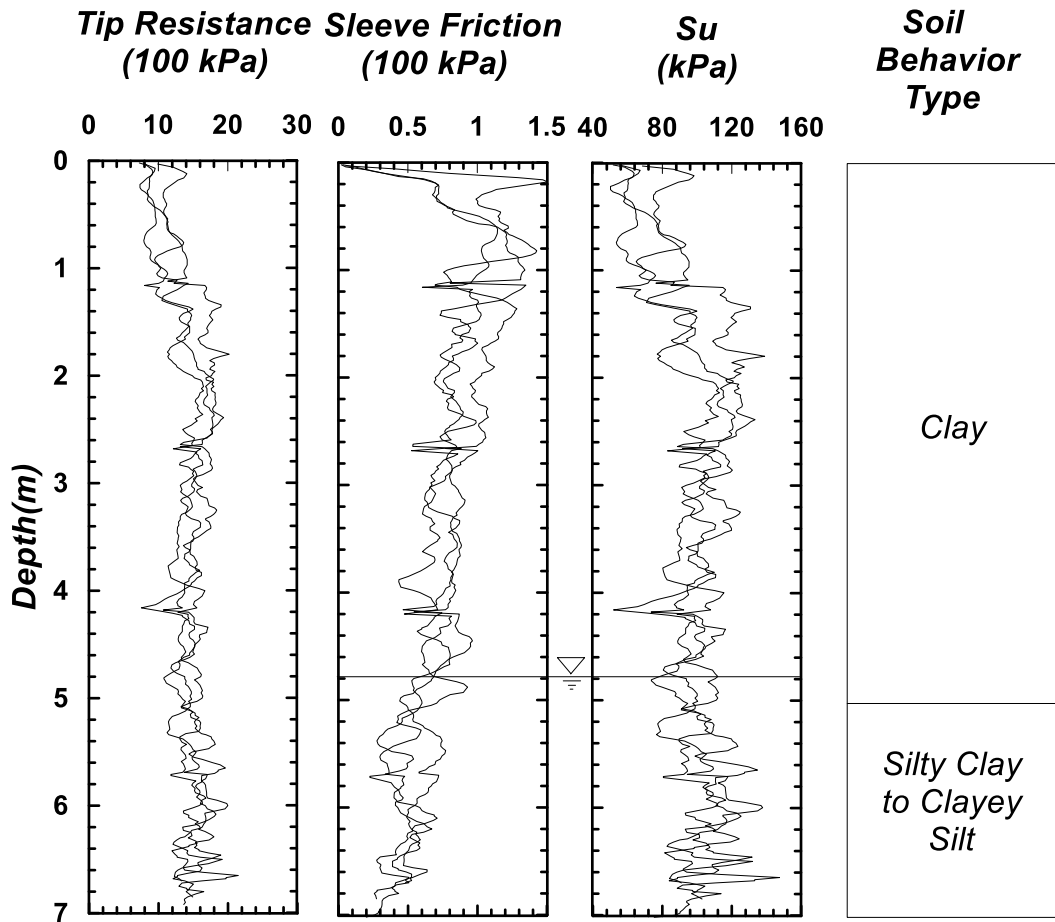


Figure 3-3: CPT profile of Site 1 at the University of Alberta Farm

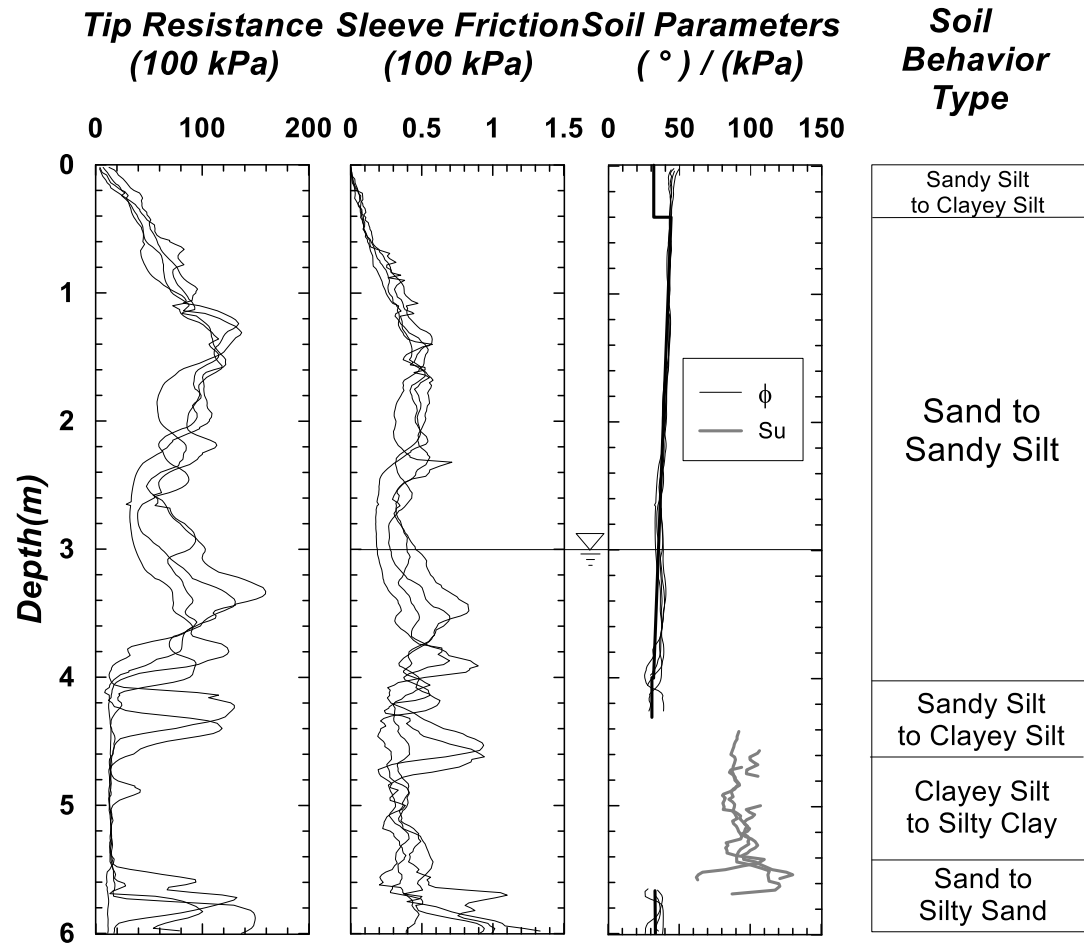


Figure 3-4: CPT profile of Site 2 at the Sand Pit in Bruderheim

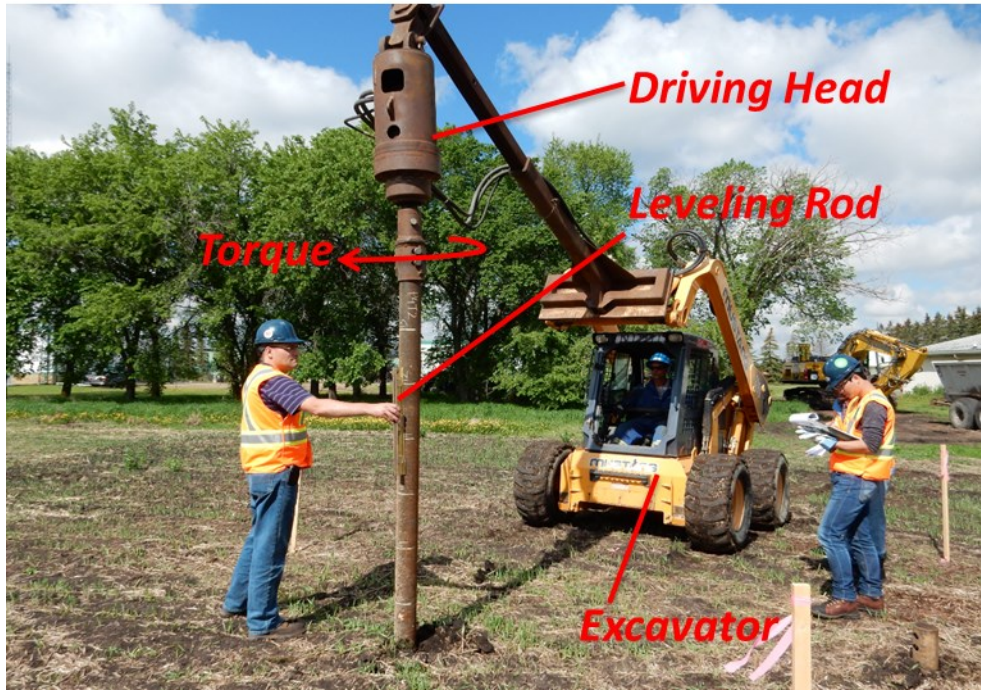


Figure 3-5: Installation of a helical pile

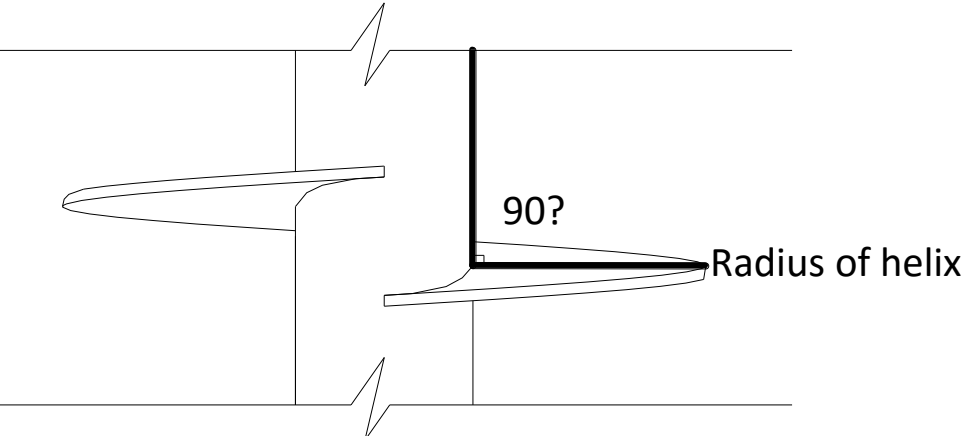


Figure 3-6: The true helix design

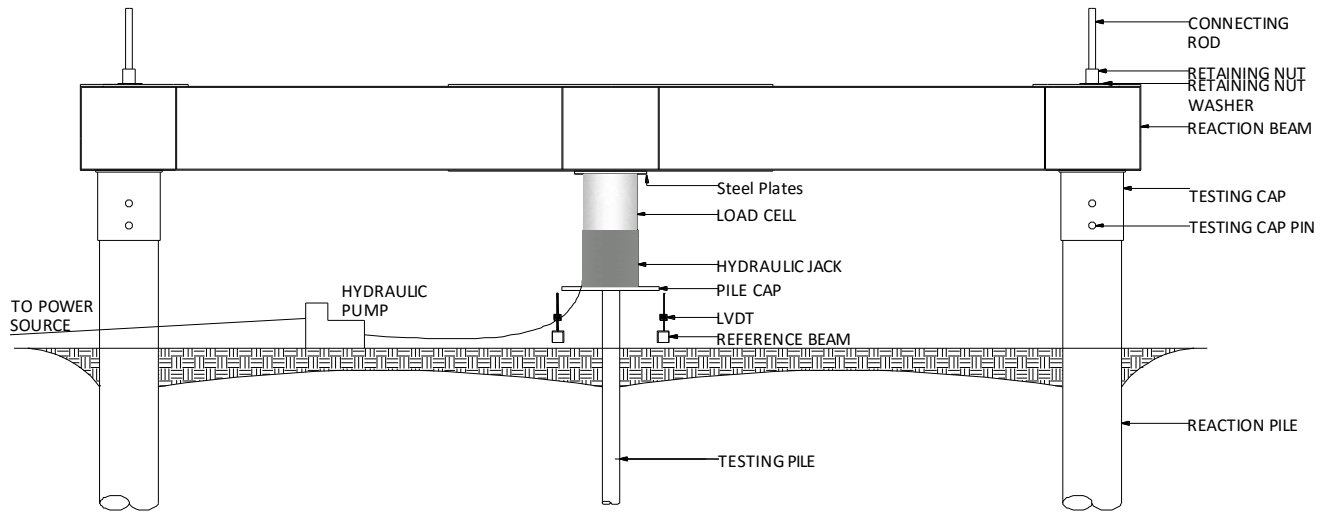


Figure 3-7: Test frame of axial compression loading

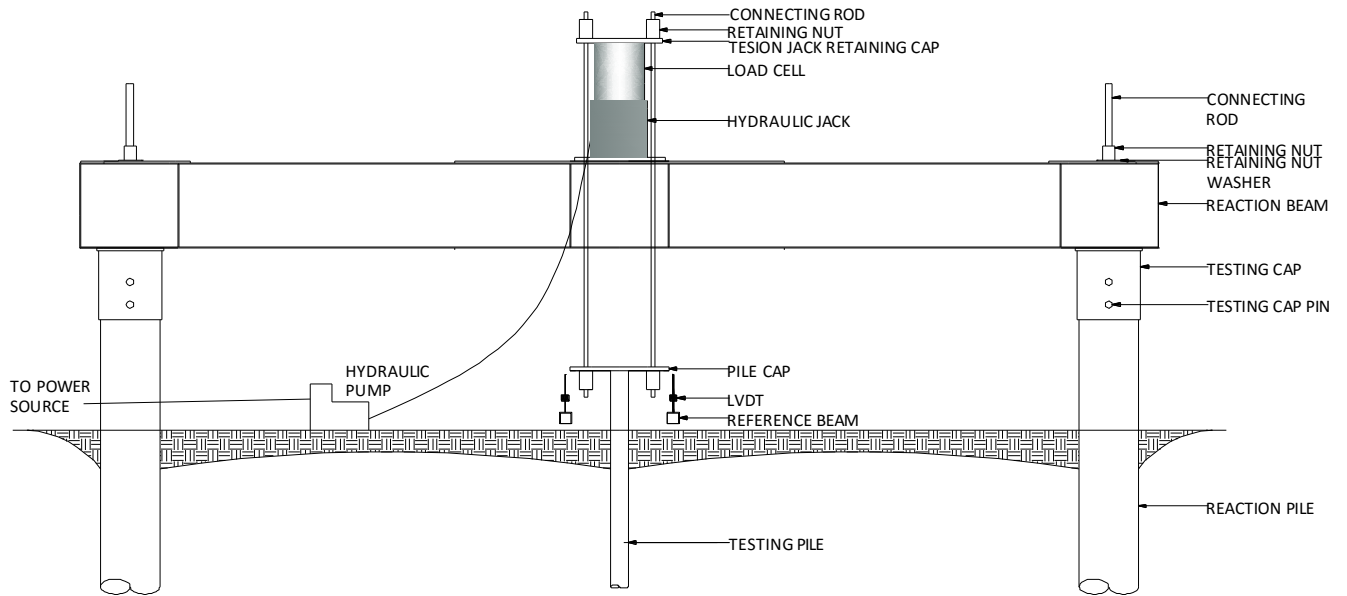


Figure 3-8: Test frame of axial tension loading



Figure 3-9: Setup of axial compression tests



Figure 3-10: Setup of axial tension tests

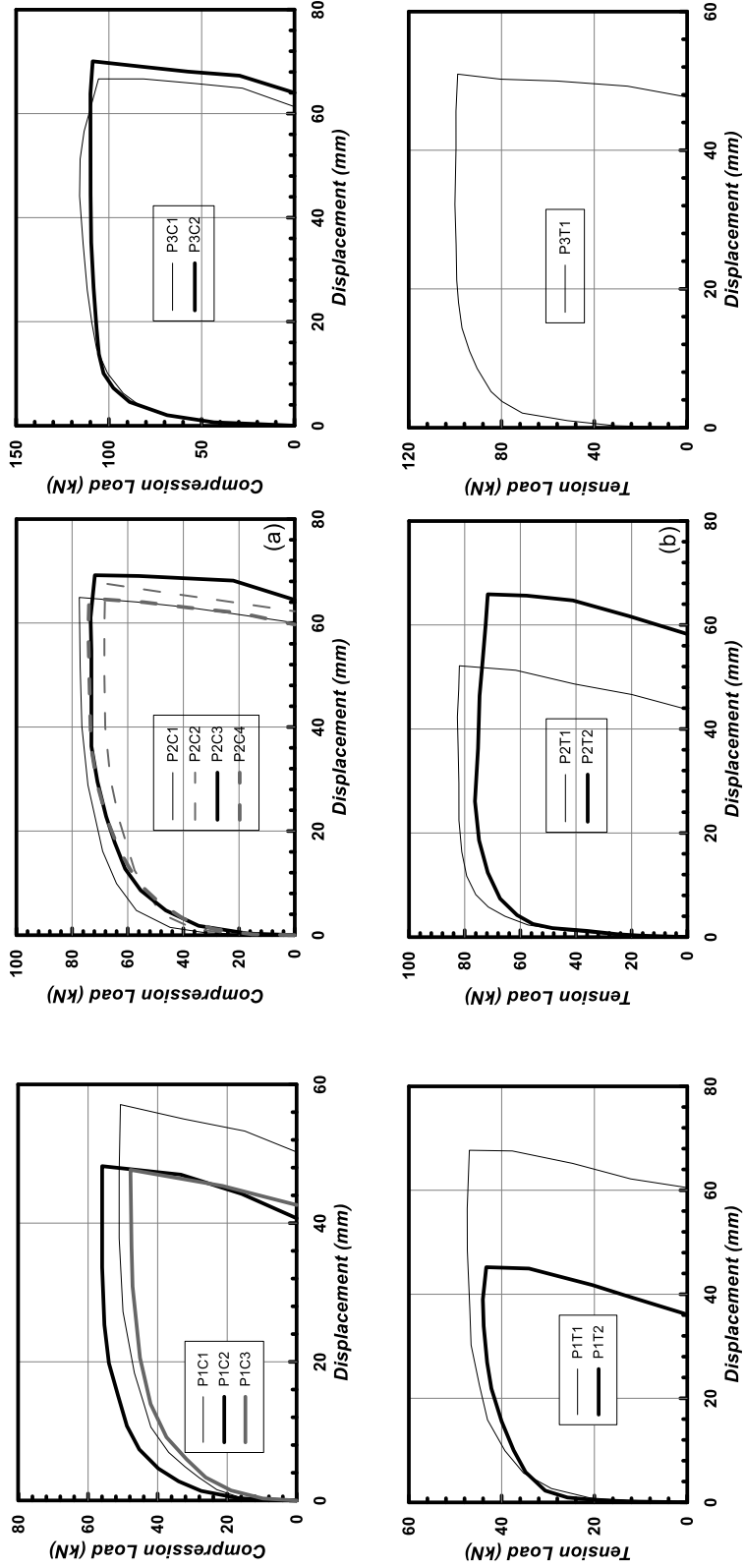


Figure 3-11: Test results from Site 1

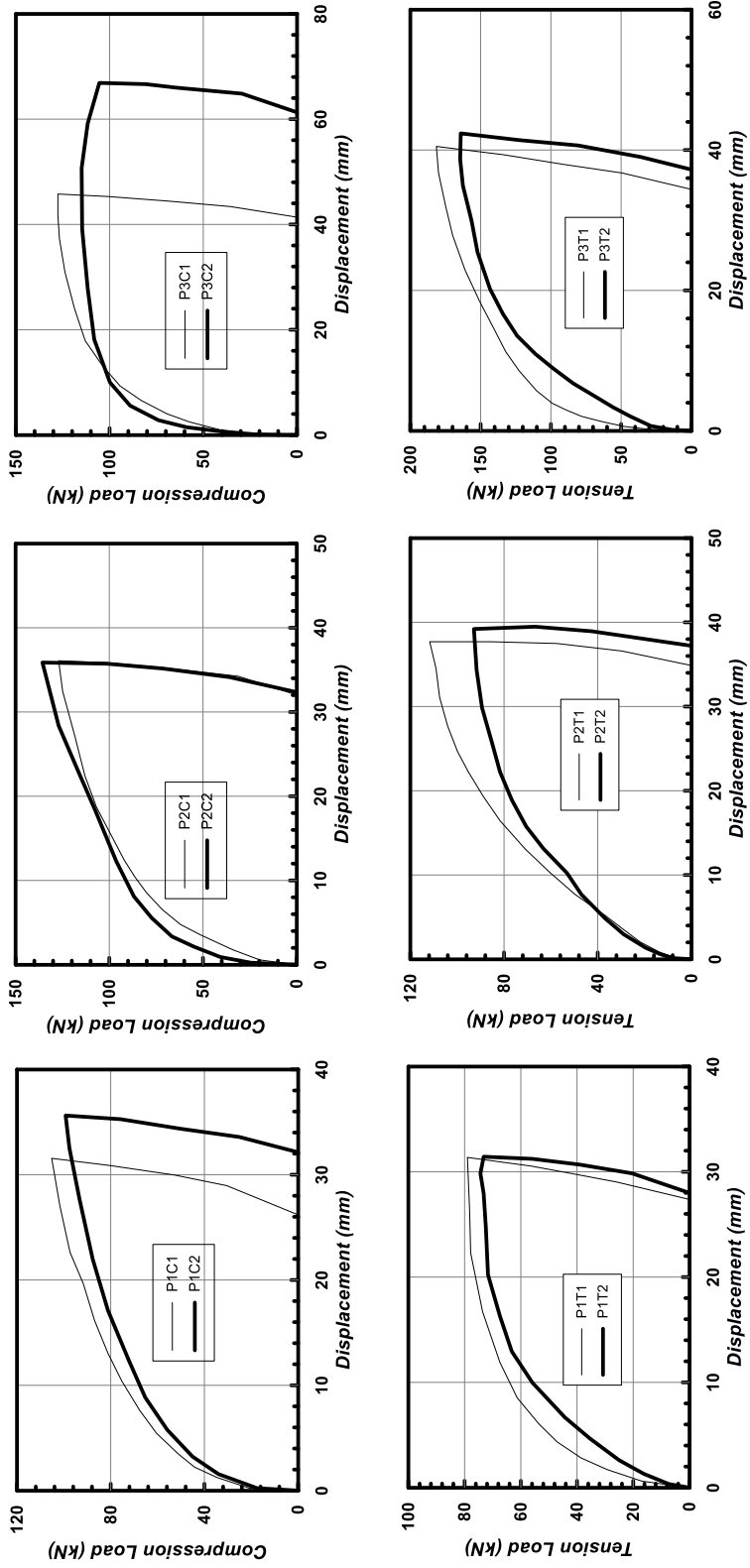


Figure 3-12: Test results from Site 2

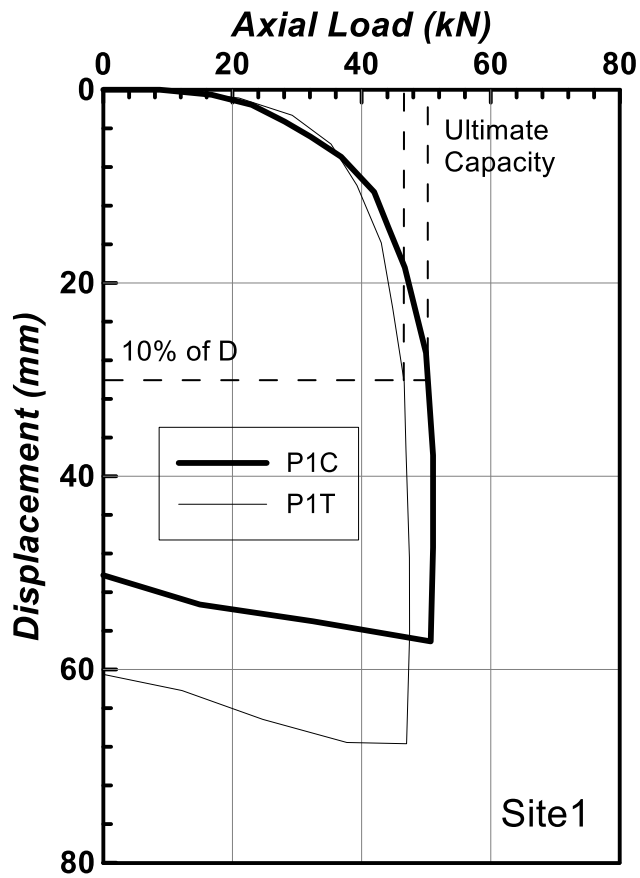


Figure 3-13: Axial ultimate capacity interpretation using the load-displacement curves of Type 1 piles (P1) under compression (P1C) and tension (P1T) loading at Site 1

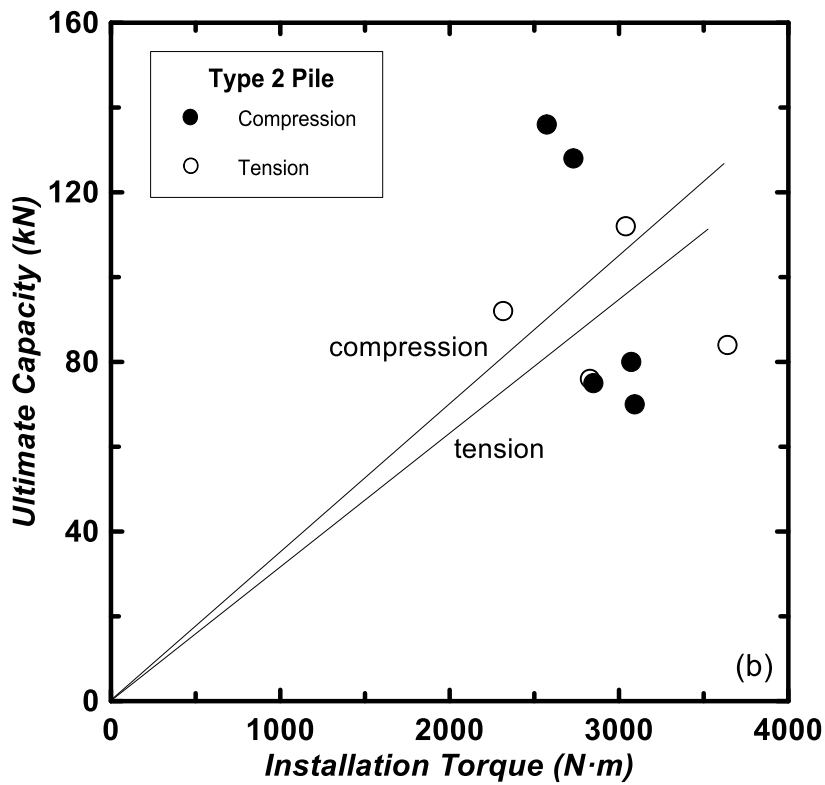
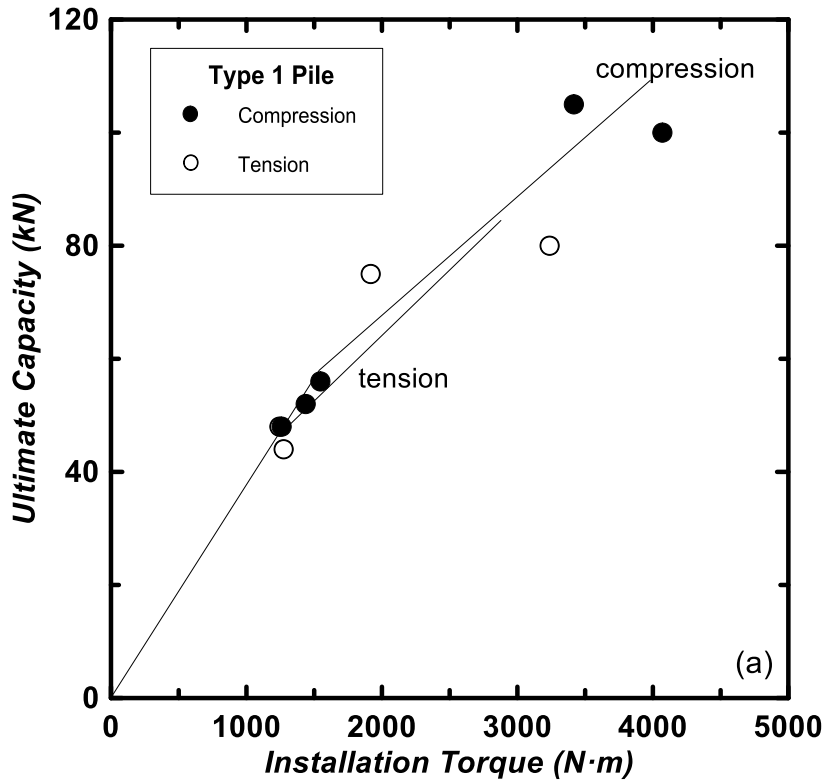


Figure 3-14: Torque factor design charts for the tested piles (to be continued)

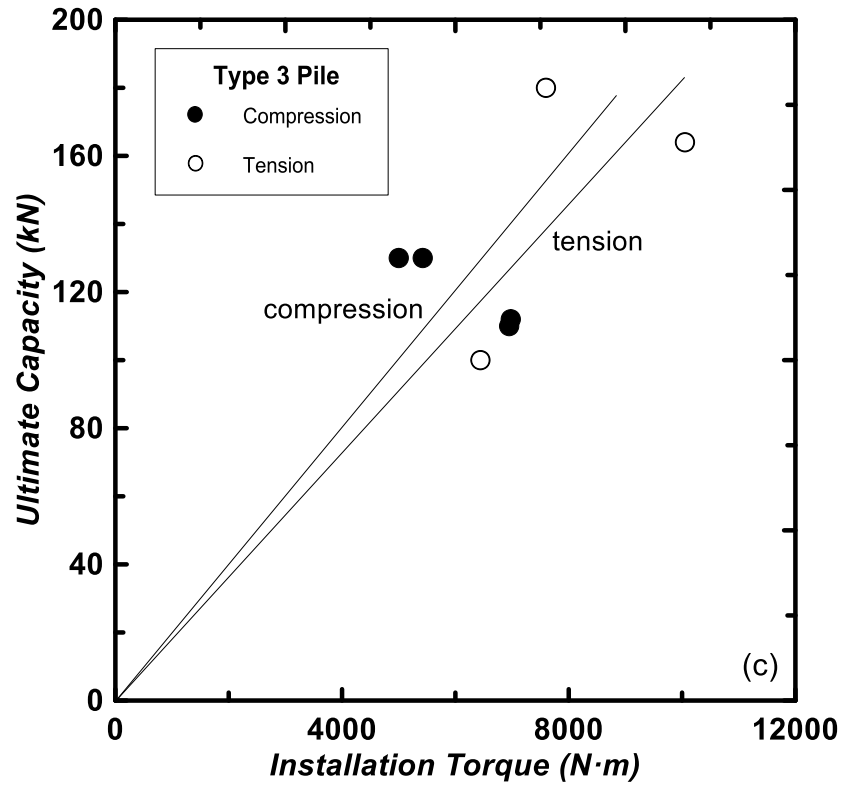


Figure 3-14: Torque factor design charts for the tested piles

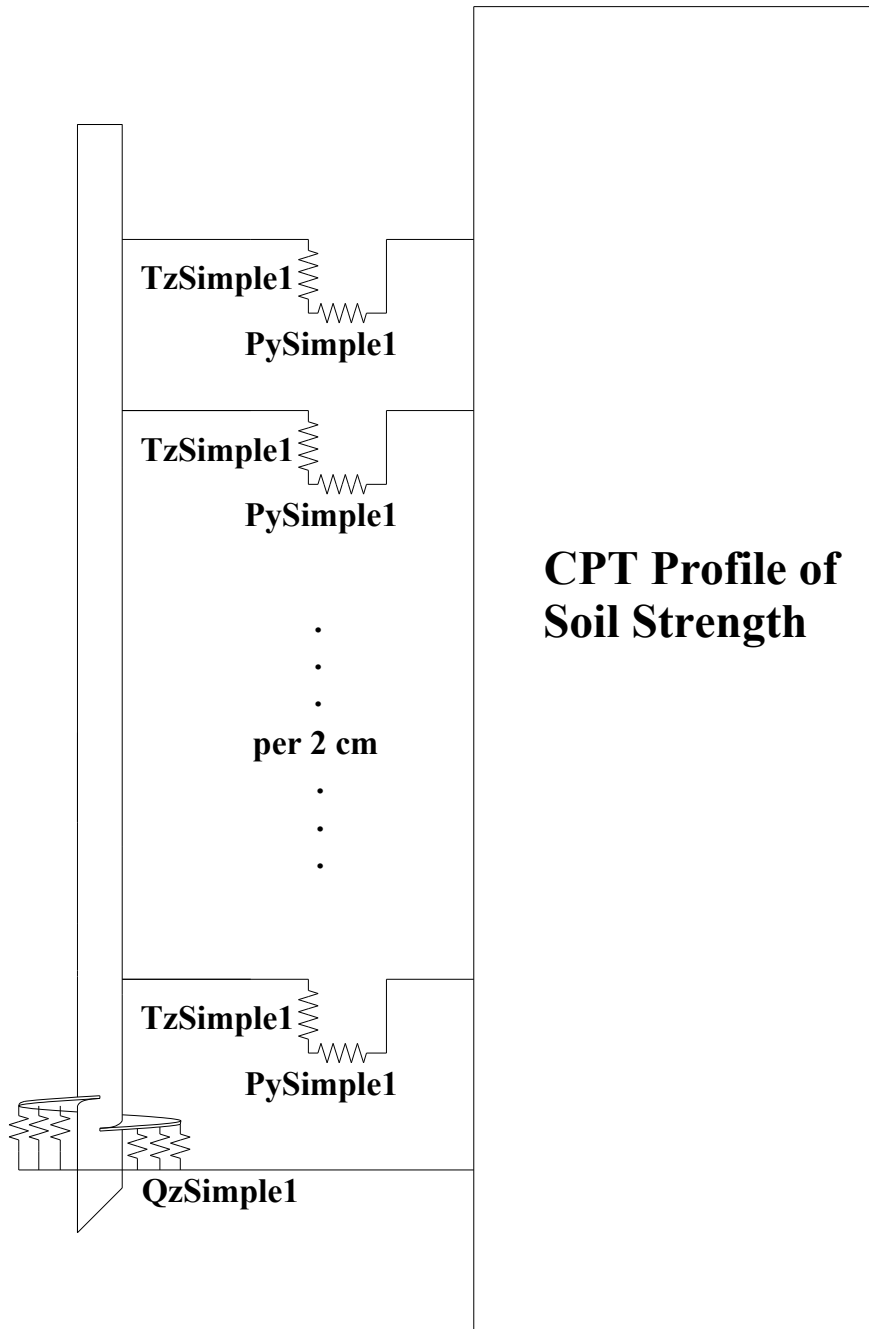


Figure 3-15: Numerical model configuration

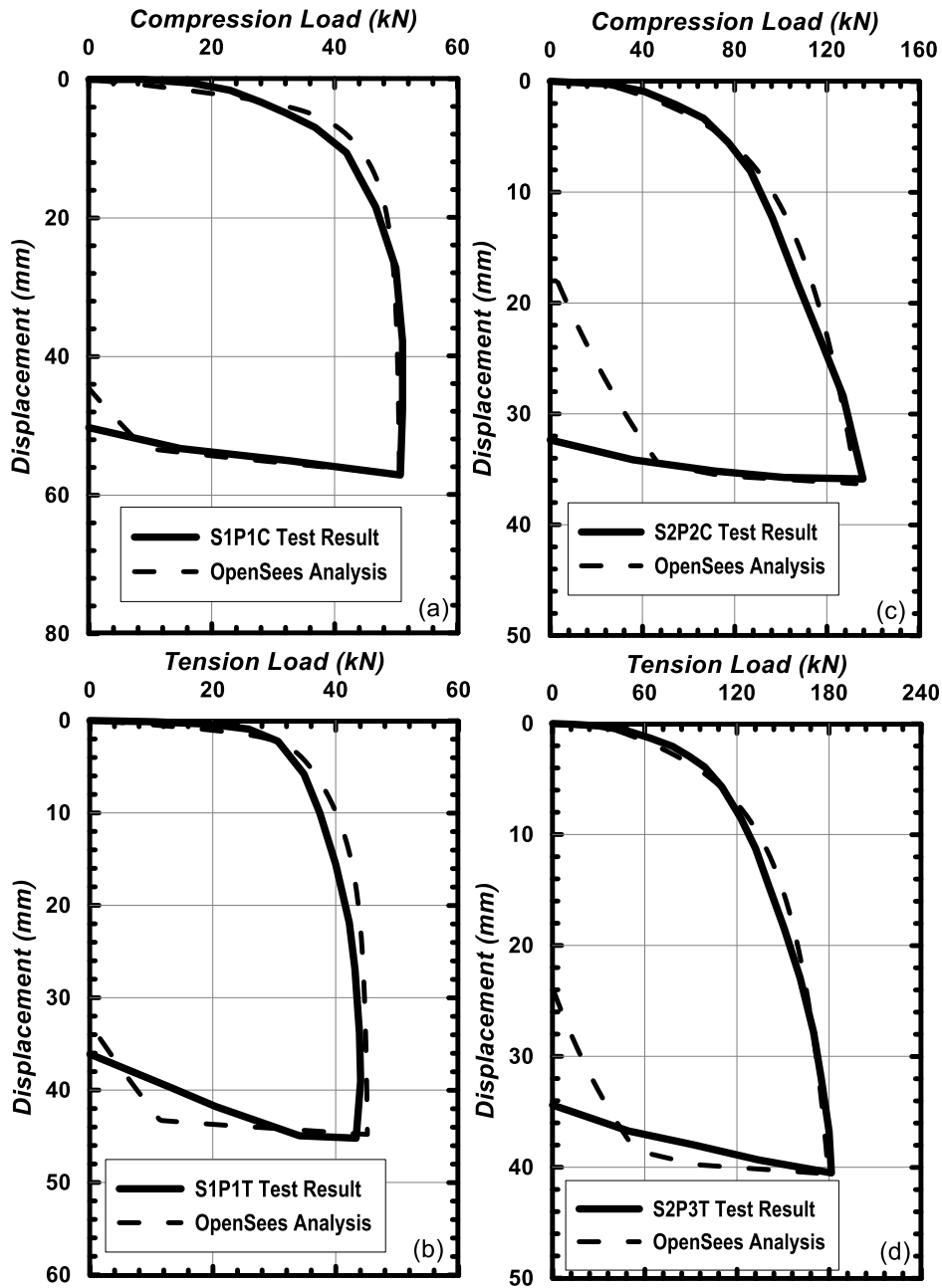


Figure 3-16: Comparison of numerical modeling to the in-situ test results of selected helical piles in clay (a)(b), and sand (c)(d)

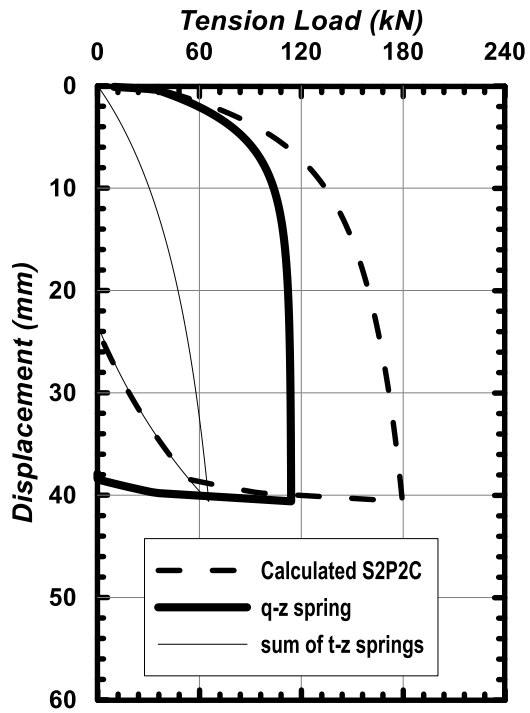


Figure 3-17: The components of numerical load-displacement curve for S2P2C

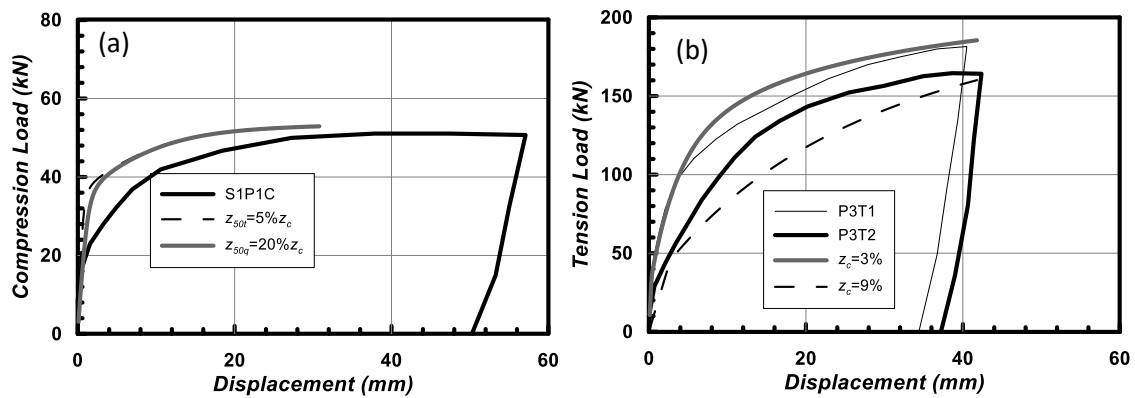


Figure 3-18: The sensitivity of the axial behavior to the half capacity displacement z_{50}

4 Numerical Modeling of Lateral Behavior of Helical Piles and Parametric Analyses

Abstract

The contribution of helix to the lateral capacity of helical piles has not been systematically quantified in the current literature. To find out the influence of helix on the lateral capacity is one of the critical interests to practitioners and researchers; this will substantially improve the design practice of helical piles used to resist large lateral loads due to winds or earthquake loads. In the present research, a 3-D BNWF model was developed to simulate the lateral behavior of helical piles in soft clay and dense sand; the model was calibrated against results of several existing lateral tests in the literature. A series of parametric analyses were carried out using the BNWF model to investigate the factors that influence the lateral capacity. For the parametric analyses, the diameter of helix, embedment depth of helix, diameter of pile shaft, diameter of bucket, and length of bucket were altered to investigate the response of the lateral capacity. It was found that the improvement of lateral capacity showed different tendency in soft clay and dense sand, and helical pile dimensions may be optimized to obtain the most effective lateral capacity.

4.1 Introduction

The lateral resistance of helical piles subject to wind and earthquake loads is a major concern when helical piles are being used or designed for lateral loads in relevant regions. Thus far there has been only a limited number of research projects devoted to the lateral behavior of helical piles. Puri et al. (1984) conducted a series lateral load tests on small-scale single-helix, double-helix, and triple-helix model piles in sand in the laboratory and proposed a mathematical relationship between lateral load and horizontal pile head deflection whereas there was no factor in this relationship accounted for the helices. Puri et al. (1984) recommended the lateral capacity of helical piles based on the evaluation procedures developed for conventional piles. Zhang

(1999) carried out field lateral load tests on 3-helix piles in clay and sand. Sakr (2009) presented lateral load tests on a single-helix pile and a double-helix pile installed in oil sands. Since both Zhang (1999) and Sakr (2009) seated the helices at a large depth, the effect of the helix on lateral capacity was considered minimal.

Prasad and Narasimha Rao (1996) compared the ultimate lateral capacities of straight piles without helix, double-helix piles, and 4-helix piles in soft clay. It was found the lateral capacity was significantly improved by the helices, and the improvement by 4 helices was greater than that by 2 helices. A similar and more comprehensive conclusion about the effect of helix was given by Al-Baghdadi et al. (2015) for helical piles in sand. The embedment depth of the helix, diameter of the helix, and diameter of the shaft were investigated as the factors that might influence the performance of helix. However the number of the control groups was not enough to develop an integrated profile of the effect of the helix subject to these factors. Besides, the helix was simplified into a horizontal plane plate which is different from the spiral configuration of the helix that would cause a considerable distinction according to the parametric study presented by Kurian and Shah (2009). The spiral configuration of the helix was implemented in a 3-D continuum finite element model developed by Kurian and Shah (2009) to evaluate the influence of the helix pitch and the inclination of the helix blade on the performance of the helix under lateral and axial loads. However, helix embedment depth and diameter of the shaft were not included.

Previous studies on the lateral behavior have suggested the following points: the influence of the helix may be negligible when the embedment depth is large (Puri et al. 1984, Zhang 1999, Sakr 2009), the lateral capacity is improved by 20% to 50% in soft clay (Prasad and Narasimha Rao

1996), and increased helix embedment depth decreases the limited improvement of lateral capacity in dense sand (Al-Baghdadi et al. 2015).

Despite previous research on the lateral behaviour of helical piles, there is a lack of study in the effects of helical plates in deep or shallow positions and on how to optimize the helical pile dimensions to maximize the lateral capacity. Therefore, a more systematic parametric study that involves the critical dimensions of the helical pile is necessary to better understand the effects of helix on the lateral capacity. In addition, the bucket pile, which is a special type of helical piles with enlarged segment (bucket) near the ground surface, has been introduced in recent years to carry large lateral resistance; however, the behavior of bucket pile has yet to be investigated. Corresponding to the knowledge gap, the specific objectives of the present study are: (i) develop a BNWF model to simulate the lateral behavior of helical piles and bucket piles based on existing lateral load tests; and (ii) evaluate the influence of several critical factors on lateral capacity: helix diameter, shaft diameter, helix embedment depth, bucket diameter, and bucket length.

4.2 Development of Numerical Models

The lateral resistance of a helical pile consists of lateral soil resistance (p - y spring) against the shaft, normal resistance (q - z spring) on the upper and lower surfaces of the helix against overturning, and the skin friction or adhesion (t - z spring) on shaft surfaces (Prasad and Narasimha Rao, 1996). In the developed 3-D BNWF numerical model, presented in Figure 4-1, the pile shaft is simplified as nonlinear beam-column elements connected by pile nodes, and the helix plate is represented by a set of rigid beams connected to the central shaft column via pile nodes in a spiral way. Every rigid beam is perpendicular to the central shaft column according to the “true helix” design. Three types of soil reaction springs connect the pile nodes to the relative

fixed nodes to provide soil reaction force. The material of the shaft has a Young's modulus of 200 GPa, a yield strength of 235 MPa, and a strain hardening ratio of 0.01. The pile dimensions are presented in Table 4-1.

Although there are approaches to evaluate the behavior of soil reaction springs by the soil strength parameters, considerable uncertainties will occur in the numerical simulation. Especially for the in-situ soil investigation, the interpreted soil strength parameters from SPT or CPT results are sometimes not reliable due to the complex soil deposits and different operator behavior.

Therefore the numerical model has to be calibrated using the physical test results. However, if the contribution of the helix to the total lateral resistance is too small, it is difficult to use the lateral load-deflection curves to calibrate the overturning resistance (q - z springs and t - z springs) of the helix. Thus an axial load-displacement curve obtained from the same soil and same pile as the lateral tests is necessary to assist the calibration of the q - z springs attached to the helix. When the helix has significant influence on the total lateral resistance, the calibration of the soil reaction springs attached to the helix can be performed based on lateral load test results after the p - y springs are calibrated by a lateral load-deflection curve of a straight pile without helix.

The assumptions when assigning parameters to the soil reaction springs are: (i) the bearing (uplift) resistance is uniformly distributed on the bottom (top) surface of the helix in axial loading tests, i.e., all the q - z springs share the same ultimate limit capacity and stiffness; (ii) the ultimate limit capacity and stiffness of the q - z springs resisting the rotation of the helix are the same as these q - z springs subject to the axial loading; and (iii) the skin friction (t - z springs) on the helix surfaces shares the same friction coefficient as the shaft skin friction.

4.2.1 Selected case studies for numerical model calibration

Sakr (2009) presented a lateral load test on a single-helix pile and found negligible influence of the helix on the total lateral resistance. In the same soil, Sakr (2009) conducted axial load tests on the same piles which provided an axial load-displacement curve for the calibration of the $q-z$ and $t-z$ springs. Prasad and Narasimha Rao (1996) provided a set of data obtained from the lateral tests in soft clay on model piles with shallowly embedded helices or straight piles without helix; it was found that, due to the shallow helices, lateral capacity was increased by more than 20% which is adequate to serve as a calibration tests.

Therefore in this section, test results presented by Sakr (2009) and Prasad and Narasimha Rao (1996) are adopted to calibrate the BNWF numerical model for the respective lateral load tests. Specifically, for Sakr's piles, an axial behavior simulation is used to calibrate the $q-z$ springs and $t-z$ springs before installing them into the numerical model for lateral behavior. For Prasad and Narasimha Rao's piles (see Figure 2-17), the $p-y$ springs are calibrated using the load-deflection curve of the straight pile; then the test results of the lateral loading on the double-helix piles are used to calibrate the $q-z$ and $t-z$ springs attached to the helix.

In order to calibrate the $q-z$ springs and the $t-z$ springs, a single-helix pile model has been built for Sakr's (2009) compression and uplift load tests. A straight pile model is developed to calibrate the $p-y$ springs using Prasad and Narasimha Rao's (1996) test results. After that a double-helix pile model is created for the simulation of the lateral behavior of Sakr's (2009) and Prasad and Narasimha Rao's (1996) test results to accomplish the calibration of all the soil reaction springs involved.

4.2.2 Calibration of soil reaction springs

Every soil spring requires two parameters: the ultimate capacity (t_{ult} , q_{ult} , or p_{ult}) and the displacement at half capacity (z_{50t} , z_{50q} , or y_{50}). The adjustment of the soil spring parameters is presented in the following subsections, and the approaches adopted to evaluate these parameters are summarized in Table 4-2.

4.2.2.1 Calibration of Sakr's (2009) axial load test

Two types of soil springs, namely t - z springs and q - z springs, are assembled in this model using the backbones respectively after Mosher (1984) and Vijayvirgya (1977). In the scenario presented by Sakr (2009), where piles were installed in saturated dense sand, the end bearing factor N_q for drilled piles (Meyerhof, 1976) and breakout factor N_b (Das, 1990) based on friction angles are adopted to estimate the ultimate bearing and uplift capacity of the helix using

Equations 4-1 and 4-2:

$$q_{ult} = \frac{\pi}{4} \sigma' N_q D^2 \quad (4-1)$$

$$q_{ult} = \frac{\pi}{4} \sigma' N_b D^2 \quad (4-2)$$

According to

Table 3-3, z_{50q} is less than the critical displacement z_c which ranges from 3% to 9% of the helix. Estimated from Figure 3-12, z_{50q} is about one eighth of z_c for compression tests, and one fifth for tension tests.

For t - z springs, Mosher (1984) proposed a method to evaluate the ultimate skin friction capacity, t_{ult} , and the displacement at half of the capacity, z_{50t} , using the frictional angle, depth to shaft diameter ratio z/d , and the initial slope k_f . A design chart and k_f values varying against frictional

angles are given by Castello (1980) and Mosher (1984) to estimate t_{ult} and z_{50t} respectively, see Figure 2-6 and Table 2-1.

The calibration result of the single-helix pile compression and tension tests is presented in Figure 4-2a. It is shown in Figure 4-2a the backbones developed from different types of piles and soils have the potential to simulate a lot of other types of piles and soils. The end bearing factor N_q is increased by 30%, the breakout factor N_b is increased by 13%, t_{ult} is increased by 15%, z_{50t} is decreased by 30%, and z_{50q} is selected to be $1/8 \cdot 4.5\% \cdot D$ for compression and $1/5 \cdot 6.4\% \cdot D$ for tension. The adjusted parameters of the soil springs are presented in Table 4-2.

4.2.2.2 Calibration of Prasad and Narasimha Rao's (1996) straight pile load test

P - y springs are calibrated in this simulation of laterally loaded straight pile behavior. Prasad and Narasimha Rao's (1996) experiments selected saturated soft clay with undrained shear strength s_u of 3 kPa. Matlock (1970) proposed a method to estimate p_{ult} and y_{50} by s_u , γ' , and ε_{50} . Since Prasad and Narasimha Rao (1996) did not present γ' or ε_{50} , typical values of saturated unit weight of 17.3 kN/m³ and ε_{50} of 0.03 for soft clay are selected. Based on the selected γ' or ε_{50} it was found that the computed load vs. displacement curve matched the measured curve as shown in Figure 4-2b. Summarized in Table 4-2, the p_{ult} is modified to be 6% higher than values recommended by Matlock (1970).

4.2.2.3 Calibration of Sakr's (2009) laterally loaded helical pile

After the q - z and t - z springs are verified, they were transferred to a double-helix pile numerical model with a series of p - y springs to simulate the behavior obtained by Sakr (2009) of double-helix pile subject to static lateral load. American Petroleum Institute (1993) presented an integrated method to develop the p - y springs in sand. After API (1993), the p_{ult} is reduced by 28%

from the API (1993) recommended value and the y_{50} is consistent with the recommended value to achieve a best agreement with the measured load-deflection curve as presented in Figure 4-3. To consider the realistic load condition in the practice, a vertical dead load about half of the axial ultimate capacity (500 kN) and a rotation constraint were separately added to the pile head to observe the response of the lateral load-deflection curve as depicted in Figure 4-3a. It is shown that the axial dead load reduces the lateral load, but the pile head rotation constraint improves the lateral performance.

4.2.2.4 Calibration of Prasad and Narasimha Rao's (1996) laterally loaded helical pile

The t - z and q - z springs of helical piles in clay are developed after Coyle and Reese (1966) and Aschenbrenner and Olson (1984) respectively. The recommended unit value of t_{ult} for soft clay whose s_u varies between 2 kPa and 5 kPa equals to $1.0s_u$. The z_{50t} is recommended to be 3.8 mm for the embedment depth of the present model piles. The uniform bearing or uplift capacity, q_{ult} per unit area, is recommended to be $9.0s_u$, and the z_{50q} is suggested to be less than z_{cq} that equals 1% of the helix diameter D . After a few trials, z_{50q} is selected to be 0.1% of D and the rest of the three parameters are kept consistent to the recommended values. Figure 4-3b exhibits the agreement between the measured and computed curves. A similar comparison was also conducted to investigate the influence of the axial dead load and pile head rotation constraint as shown in Figure 4-3. It is found the pile head rotation constraint significantly improves the lateral capacity, but the axial load has minor influence on the lateral capacity.

4.2.2.5 Results of calibrations

Based on the prior numerical simulations of the helical pile load-displacement curves measured by Sakr (2009) and Prasad and Narasimha Rao (1996), all the three types of soil springs are developed, modified, and installed into two single-helix numerical models for the following

parametric analysis. The adjustment of soil spring parameters based on the recommended values by the adopted approaches may be due to the uncertainties of the in-situ soil test results, the simplification of soil property profile, the load testing operation, and the particularity of the piles and soils used to develop the backbones of the soil pile interaction curves. The numerical calibration shows a potential of the BNWF method with the three types of soil springs to simulate the performance of helical piles in cohesionless and cohesive soils under static loading.

4.3 Parametric Analyses

After the numerical model has been validated for lateral load tests, the parametric analyses are carried out by varying the helical pile dimensions. As presented in Figure 1-1, a helical pile is characterized by the dimensions of the shaft, helix, and bucket, where a bucket is an enlarged shaft segment near the ground surface to increase the lateral capacity of the pile. In the present study, the numerical model for a single-helix pile is adopted to better quantify the effect of the diameter and embedment of the helix. The diameter of the shaft d , the length of shaft L , the diameter of the helix D , the position (embedment depth) of the helix H , the diameter of the bucket d_B , and the length of the bucket l_B are altered from the original dimensions.

The lateral resistance of helical piles in parametric analyses is adopted as the primary indicator of the influence of pile dimensions. In the present study, the lateral capacity of the pile is taken as the lateral resistance mobilized at 10% of the shaft diameter in the analysis. In the literature, there is no general agreement on the criterion for ultimate lateral capacity. For example, O'Neill and Reese (1999) used the ultimate lateral load at the pile head displacement at 5% of shaft diameter, Prakash and Sharma (1990) recommended 6.25 mm head displacement, and US – ACE (1991) suggested 6.25 mm (0.25 in) to 12.5 mm (0.5 in). However, the 6.25 mm or 12.5 mm is considered too strict for pile shaft of this size in many applications. According to the results

shown in Figure 4-3, the lateral resistance is almost linear within head deflection at 10% shaft diameter (Sakr, 2009) or ground line point deflection (Prasad and Narasimha Rao, 1996).

Besides, 10% of the shaft diameter of Sakr's (2009) pile is larger than 12.5 mm, so we can linearly convert the lateral load at the deflection of 10% of shaft diameter to the lateral load at the deflection of 5%, 6.25 mm, or 12.5 mm. Therefore the 10% criterion was applied to obtain the ultimate lateral capacity.

It should be noted from Figure 4-3 that this study focuses on the lateral behavior of the single pile without superstructures.

4.3.1 Influence of helix diameter D compared to helix embedment H

In general, the resistance of the helix against overturning increases with the diameter and rotation angle in a given soil. The rotation angle is related to the bending moment distribution along the pile length so that the location of the helix (H) determines the rotation angle. Thus the diameter and embedment of the helix are varied in the numerical model to obtain different lateral capacities to compare with the lateral capacity of corresponding straight piles. Based on the calibrated models, the lateral capacity of the straight pile is 26.0 kN for Sakr's (2009) and 13.6 N for Prasad and Narasimha Rao's (1996). In the computation, D/d is varied from about 4.0 to 8.0, and H/E is varied from 10% to 90% for both models. The lateral capacity improvement H_I is defined as:

$$H_I = \frac{H_u - H_{u0}}{H_{u0}} \cdot 100\% \quad (4-3)$$

3)

where H_u is the ultimate lateral capacity of helical piles, and H_{u0} is the ultimate lateral capacity of the benchmark straight piles without helix. The curves of H_I against D/d and H/E are plotted

in Figure 4-4. It is shown in Figure 4-4 that, H_l increases with the helix diameter whereas shows a non-monotonic trend against the embedment H .

For the cohesionless soil of Sakr's (2009), as shown in Figure 4-4a, the lateral capacity improvement exhibits the smallest amplitude of about 1% at the largest embedment H around 90%. It gradually grows and reaches the first local max when H/E decreases to 52%, which is followed by a descending trend to the first local minimum at H/E of 36%. While the H/E continues to decrease to 12%, H_l increases to the second local max that is about 9 times greater than the first local max. With the helix approaching the ground surface, H_l decreases again.

For the cohesive soil of Prasad and Narasimha Rao's (1996), as shown in Figure 4-4b, the lateral capacity also shows a general increase with the helix diameter. All the curves share a same point where H/E ratio is about 64% and H_l is about 6%. Either H/E ratio increases or decreases from this point, H_l increases.

The comparison between the cohesionless and cohesive soils indicates that the helix embedment H should not be too small in cohesionless soil whereas in cohesive soil the helix closer to the ground surface is more effective in enhancing the lateral capacity. This is because the skin friction and normal resistance on the helix surfaces in cohesionless soils is sensitive to the effective overburden stress, by which the surface adhesion is nearly not affected in cohesive soil.

In order to better understand the behavior of H_l versus H/E ratio, the bending moment and rotation angle distribution curves of the relative straight piles are presented in Figure 4-5. The rotation angle presented in Figure 4-5b is the global rotation angle of the pile cross section, which is a result of bending moment and lateral displacement. It is shown by Figure 4-5 that for cohesionless soil, the maximum bending moment occurs close to ground surface when Z/E is about 20%, where Z is the depth of interest, and the rotation angle and lateral displacement both

decrease with Z/E until depth. However, the vertical effective stress increases with Z/E .

Considering the vertical effective stress and the helix displacement (rotation angle and lateral displacement) have opposite influence on H_l against H/E , as a result, H_l reaches the peak value at H/E ratio around 12%. The bending moment distribution of the pile in cohesionless soil, Figure 4-5a, exhibits a fixed point where the bending moment is zero at 68% of H/E . Below this point, H_l is found to be negligible as shown in Figure 4-4a.

For the cohesive soil, the undrained shear strength of 3 kPa is too small to yield the pile shaft, so that the rotation angle distribution looks linear and the rotation angle is small. Thus the main resistance of the helix is the cohesion developed on the extensive surface area of helix. Besides, the cohesion on the helix increases when H/E decreases so that the maximum H_l is found at the ground surface as shown in Figure 4-4. In the practice, proper embedment depth has to be controlled such that the cohesion on the upper surface of helix can be developed.

4.3.2 Influence of helix diameter D compared to shaft diameter d

Apparently, both helix diameter D and pile shaft diameter d influence the lateral capacity of helical piles. However, in practice, D is usually limited by the torsional strength of the pile shaft, because the installation torque can be significantly increased by helix diameter (Tsuha et al. 2007). When the helix diameter is beyond the upper limit, the pile body may be damaged during installation. According to the prior analysis, the influence of D on the improvement of lateral capacity depends on the embedment depth H . To maximize the advantage of helix diameter, the embedment H should be selected to be 12 % of the pile embedment depth E in cohesionless soils. According to Figure 4-4a, when a frequently seen large D/d ratio of 5.0 is applied, the lateral resistance of helical pile is improved by 9%. Whereas for cohesive soil, theoretically the helix installed right below the surface is the most effective way to enhance the lateral capacity. For D

= $5.0d$, the helix close to the soft clay ground surface can also improve the lateral capacity by about 9%.

The lateral capacity proportionally increases with shaft diameter d . For instance, the lateral capacity theoretically increases by 50% when the shaft diameter d is enlarged by 50%. Although the influence of helix diameter is limited compared to shaft diameter, more helices can be considered to enhance the improvement. After all, the material cost is also proportional to shaft diameter.

4.3.3 Influence of bucket diameter d_B compared to bucket length l_B

According to Section 4.3.1, the maximum H_I is near to the greatest rotation angle and lateral displacement. Similarly it is assumed that an enlarged pile shaft (bucket) close to the greatest lateral displacement can effectively improve the lateral capacity. In this analysis, the diameter and length of the bucket are varied from $2.0d$ to $5.0d$ and $0.2E$ to $0.4E$ respectively to observe the improvement of the lateral capacity. The selection of these two ranges is based on the consideration that the bending moment and rotation angle reach the minimum value below the depth of $0.4E$, and $5.0d$ is a commonly used large bucket diameter.

The analysis results are shown in Figure 4-6. For dense sand in Figure 4-6a, H_I increases significantly with the bucket diameter d_B and bucket length l_B . When l_B exceeds $0.22E$, the improvement turns to be less effective and almost ineffective at $0.4E$. For soft clay in Figure 4-6b, H_I also increases sharply with d_B and bucket length l_B . However, the increase with d_B yields at about $3.7d$, and the increase with l_B yields at $0.4E$.

Therefore, it is recommended that bucket length should not be greater than 40% of the pile embedment depth, and bucket diameter not greater than 3.7 times of shaft diameter in soft clay.

4.4 Conclusions

The numerical models of lateral behavior of helical piles are developed and calibrated by axial and lateral load test results. The parametric analysis is performed by the calibrated numerical model. The helix diameter, shaft diameter, helix embedment depth, bucket diameter, and bucket length are assigned to be the variables. The following conclusions can be drawn from the numerical model development and parametric analyses:

- i. The contribution of the helix to the total lateral resistance is negligible when it is embedded below the fixed point of the pile. The influence of a helix on the overturning resistance depends on the vertical effective stress and the helix displacement, namely the rotation angle and lateral displacement, in cohesionless soil. An optimum embedment of the helix is determined by these two factors at around 12% of the pile embedment. The optimum improvement by a single helix whose diameter is 5 times of shaft diameter is about 9%.
- ii. In soft clay, both deeply and shallowly embedded helices can improve the lateral capacity of a helical pile. Theoretically the helix installed right below the surface of soft clay is the most effective design to enhance the lateral capacity. In the practice, proper embedment depth has to be controlled such that the cohesion on the upper surface of helix can be developed. The optimum improvement by a single helix whose diameter is 5 times of shaft diameter is also about 9%.
- iii. Although the influence of helix diameter is limited compared to shaft diameter, more helices can be considered to enhance the improvement.
- iv. The effect of bucket diameter yields at about 3.7d in soft clay, but not yet in the oil sand. The lateral capacity improvement of bucket length becomes less effective when the bucket length increases, and almost ineffective at 40% of the pile embedment depth.

- v. The BNWF model with soil reaction springs implemented in OpenSees shows the potential to simulate the helical pile behavior in most of the static loading conditions.

Table 4-1: Pile geometries

Pile Type	L (m)	d (cm)	D (m)	H (m)	P (cm)
Sakr's	5.791	17.8	0.406	5.2	15.0
Prasad and Rao's	0.513	1.38	0.033	0.363	N.A.

Table 4-2: Adjustment of parameters of numerical models

Prasad and Rao's (1996)			Sakr's (2009)	
p_{ult}	Matlock (1970)	+6%	API (1993)	-28%
γ_{50}	Matlock (1970)	$\varepsilon_{50} = 0.03$	API (1993)	--
q_{ult}	Aschenbrener and Olson (1984)	--	Meyerhof (1976)	$N_q + 30\%$
			Das (1990)	$N_b + 13\%$
z_{50q}	Aschenbrener and Olson (1984)	--	Vijayvirgya (1977)	$1/8 \cdot 4.5\% \cdot D$ for Comp. $1/5 \cdot 6.4\% \cdot D$ for Tens.
t_{ult}	Coyle and Reese (1966)	--	Mosher (1984)	+15%
z_{50t}	Coyle and Reese (1966)	$z_{50t} = 0.1z_{ct}$	Mosher (1984)	-30%

Note: "+" means estimation is greater than suggested, "-" means smaller, "--" means consistent, and no sign means values selected from the suggested range.

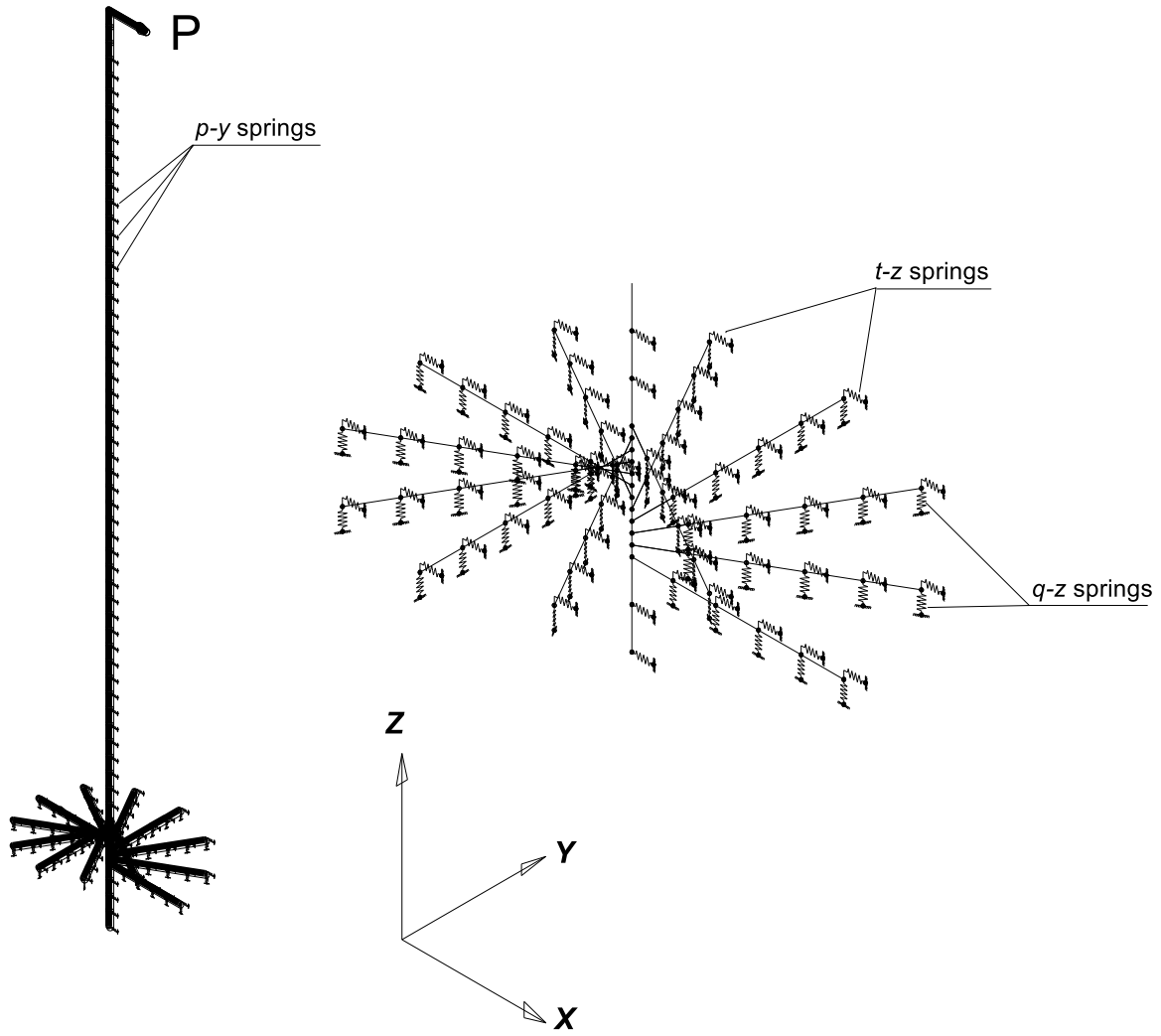


Figure 4-1: The 3-D BNWF model for a single-helix pile

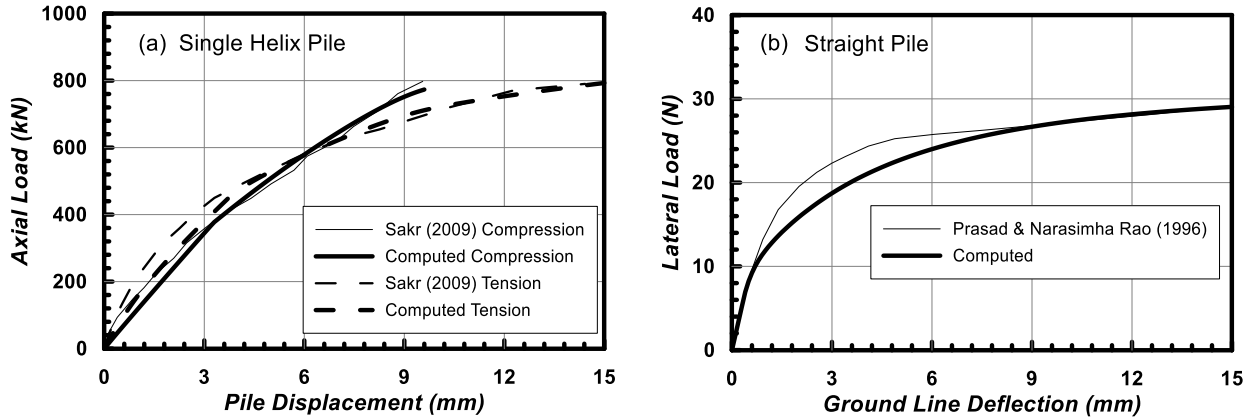


Figure 4-2: The calibration of single-helix pile and straight pile

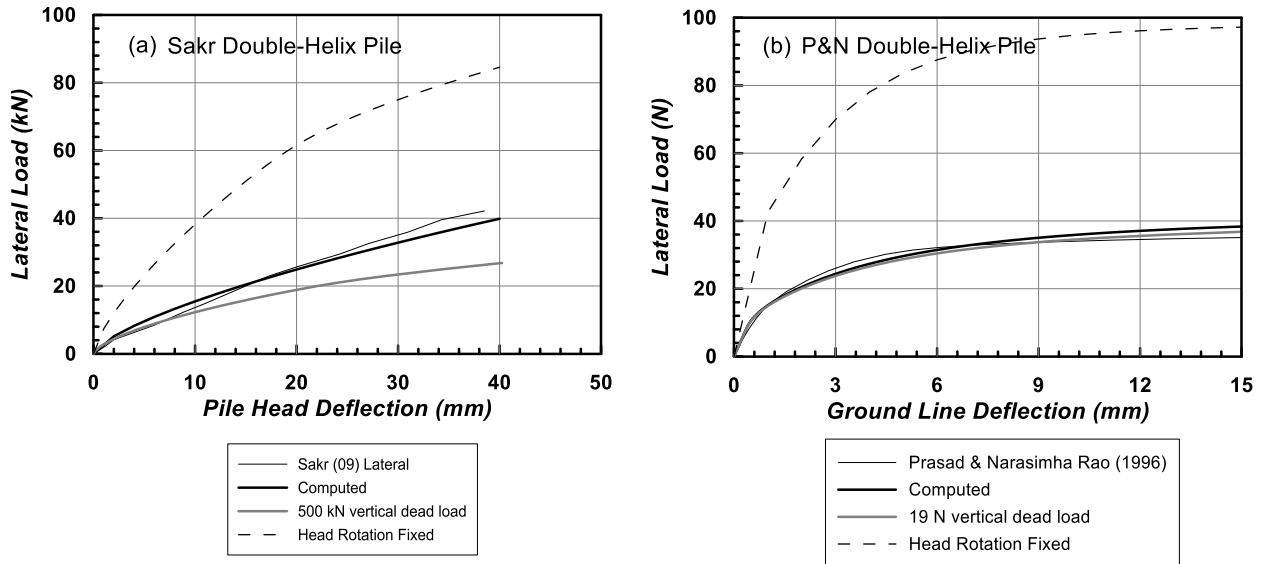


Figure 4-3: Effects of head fixity condition or vertical load on the lateral behaviour of double-helix piles under lateral loading

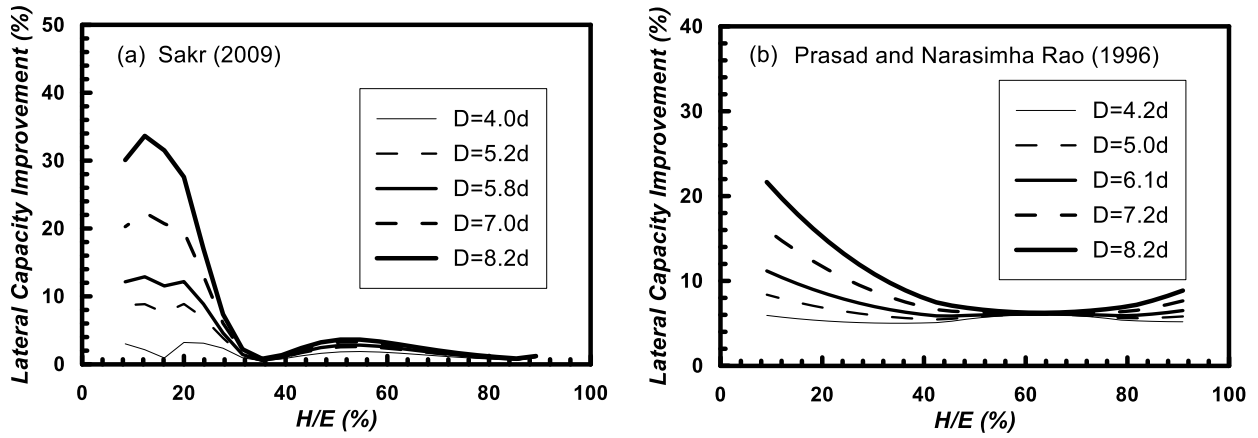


Figure 4-4: The lateral capacity improvement due to D/d and H/E

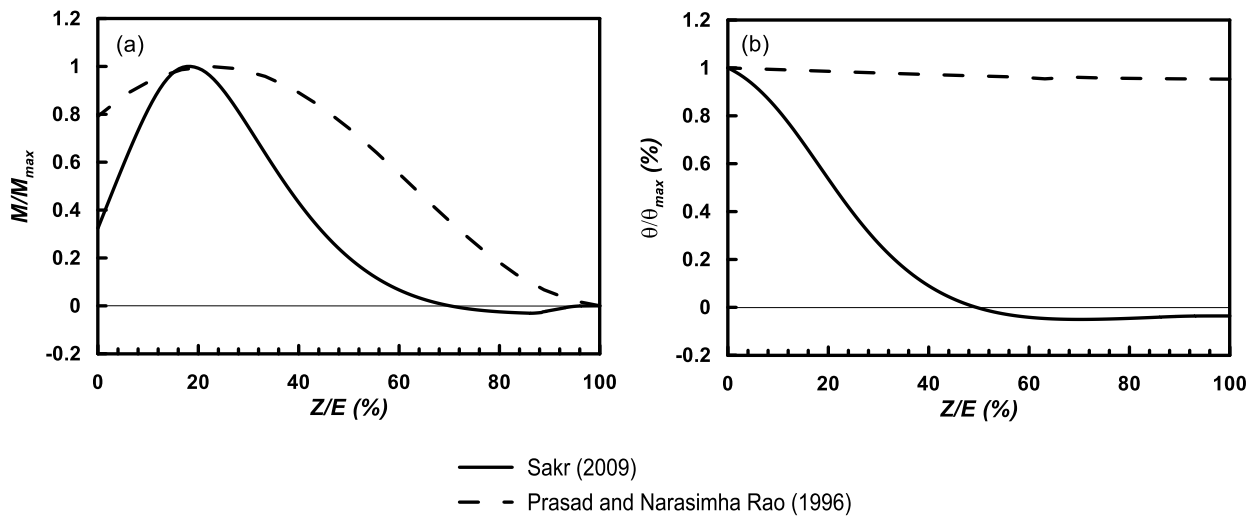


Figure 4-5: The bending moment and rotation angle distribution

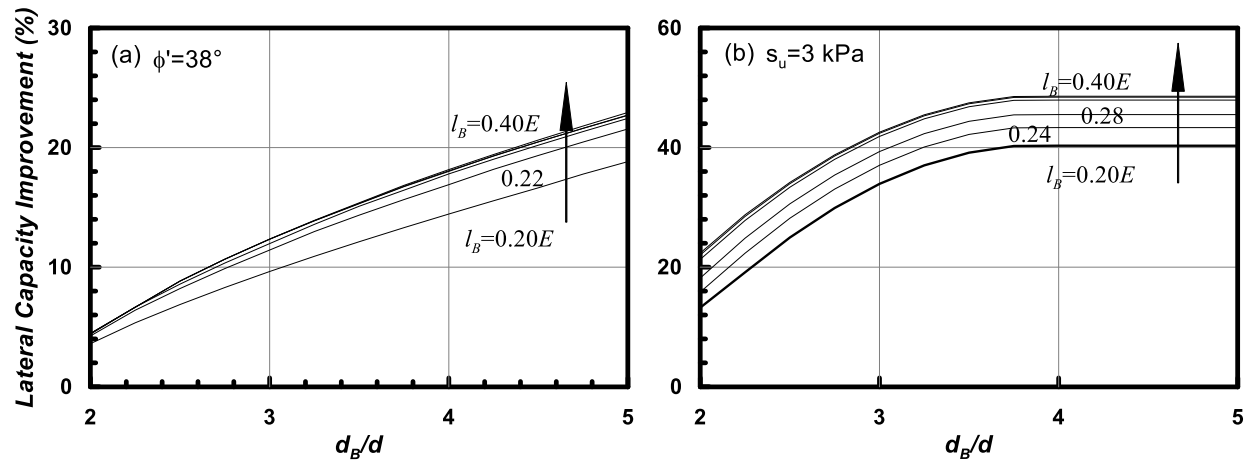


Figure 4-6: The lateral capacity improvement due to the length and diameter of bucket

5 Conclusions

The behavior of helical piles under axial and lateral static loadings was investigated using field load tests and numerical modeling method. Twenty-six single-helix piles were installed and loaded axially in two soils: medium to stiff clay, and dense sand. Axial compression and tension behaviour was examined using the axial load vs. displacement readings. In-situ CPTs were carried out at the sites to develop soil strength profiles to assist the investigation into the behavior of helical piles. BNWF models were developed and calibrated to simulate the axial and lateral behavior of helical piles. The pile dimensional parameters were altered to observe the response of the lateral resistance to the parameter alteration.

5.1 Axial Behavior of Helical Piles

- i. The helical piles exhibited two different load-displacement behaviors in cohesive and cohesionless soils. The ultimate capacities indicated by the 10% criterion are located in the plateau segments of the load-displacement curves for cohesion soil. However for the cohesionless soil, the ultimate capacities are collected before the plateau segments.
- ii. The torque factors were found to vary with helical pile dimensions and loading directions. Generally, the bigger pile had a smaller torque factor, and the torque factor for tension capacity was smaller than that of compression. Torque factor method is not safe when an underlying weak layer exists. A soil strength profile extending to a sufficiently greater depth than the pile embedment is necessary to clarify the effect of potential underlying weak layers, or a trial load should be conducted after installation.
- iii. The BNWF method in OpenSees framework is capable of producing high quality simulation for the single-helix pile under axial static loading even though the soil types

implemented in OpenSees is not sufficient yet. The simulation will be even better if the behavior of the ineffective zones can be revealed.

- iv. The influence of ineffective zones on the axial capacity of helical piles is significant and should not be ignored.
- v. The CPT based method of selecting soil reaction spring parameters of the numerical models in OpenSees is efficient and effective.
- vi. The half capacity displacement of q - z springs z_{50q} has greater influence on the simulation results for cohesionless soil than that of cohesive soil.

5.2 Lateral Behavior of Helical Piles

- i. The contribution of the helix to the total lateral resistance is negligible when it is embedded below the fixed point of the pile. The influence of a helix on the overturning resistance depends on the vertical effective stress and the helix displacement, namely the rotation angle and lateral displacement, in cohesionless soil. An optimum embedment of the helix is determined by these two factors at around 12% of the pile embedment. The optimum improvement by a single helix whose diameter is 5 times of shaft diameter is about 9%.
- ii. In soft clay, both deeply and shallowly embedded helices can improve the lateral capacity of a helical pile. Theoretically the helix installed right below the surface of soft clay is the most effective design to enhance the lateral capacity. In the practice, proper embedment depth has to be controlled such that the cohesion on the upper surface of helix can be developed. The optimum improvement by a single helix whose diameter is 5 times of shaft diameter is also about 9%.

- iii. Although the influence of helix diameter is limited compared to shaft diameter, more helices can be considered to enhance the improvement.
- iv. The effect of bucket diameter yields at about $3.7d$ in soft clay, but not yet in the oil sand. The lateral capacity improvement of bucket length becomes less effective when the bucket length increases, and almost ineffective at 40% of the pile embedment depth.
- v. The BNWF model with soil reaction springs currently available in OpenSees shows the potential to simulate the helical pile behavior in most of the static loading conditions.

5.3 Recommended Future Studies

A limitation to the study of the axial behavior of helical piles is the behavior of the ineffective zone along the pile shaft. The occurrence, progress, and ultimate length of the ineffective zone require further research to be characterized. The behavior of the ineffective zone may be affected by soil type, loading direction, and pile dimensions. Systematic research into the behavior of ineffective zones needs to be explored in the future study.

References

- American Society for Testing and Materials (ASTM). 2013. ASTM D1143/D1143M, Standard test methods for deep foundations under static axial compressive loads, West Conshohocken, PA.
- American Society for Testing and Materials (ASTM). 2013. ASTM D3689/D3689M, Standard test methods for deep foundations under static axial tensile loads, West Conshohocken, PA.
- API 1993. Recommended practice for planning, designing and constructing fixed offshore platforms – Working stress design. 20th Edition, American Petroleum Institute, Washington, D.C.
- Aschenbrenner, T. B., and Olson, R. E. 1984. Prediction of settlement of single piles in clay, Analysis and design of pile foundations. American Society of Civil Engineers, J. R. Meyer, ed., 1984.
- Bhanot, K. L. 1968. Behaviour of Scaled and Full-length Cast-in-place Concrete Piles. PhD dissertation, Department of Civil and Environmental Engineering, University of Alberta, Edmonton, Alberta.
- Boulanger, R. W., Curras, C. J., Kutter, B. L., Wilson, D. W., and Abghari, A. 1999. Seismic soil-pile-structure interaction experiments and analyses. *Journal of Geotechnical and Geoenvironmental Engineering*, ASCE, 125(9): 750-759.
- Boulanger, R. W., Kutter, B. L., Brandenburg, S. J., Singh, P., & Chang, D. 2003. Pile foundations in liquefied and laterally spreading ground during earthquakes: centrifuge experiments and analyses (No. UCD/CGM-03/01). Center for Geotechnical Modeling, Department of Civil and Environmental Engineering, University of California, Davis, California.

- Bradka, T. D. 1997. Vertical capacity of helical screw anchor piles. MEng Report, Department of Civil and Environmental Engineering, University of Alberta, Edmonton, Canada.
- Braja, M. D. 1990. Principles of foundation engineering. PC Boston.
- Brandenberg, S. J., Boulanger, R. W., Kutter, B. L., and Chang, D. 2007. Static pushover analyses of pile groups in liquefied and laterally spreading ground in centrifuge tests, *Journal of Geotechnical and Geoenvironmental Engineering*, 133(9): 1055-1066.
- Briaud, J. L., and Tucker, L. 1984. Piles in sand: a method including residual stresses. *Journal of Geotechnical Engineering*, 110(11), 1666-1680.
- Canadian Geotechnical Society 2006. Canadian Foundation Engineering Manual, 4th ed., Richmond, B.C., Canada.
- Castello, R. R. 1980. Bearing capacity of driven piles in sand, Ph.D. Thesis, Department of Civil and Environmental Engineering, Texas A&M University, College Station, TX.
- Cox, W. R., Reese, L.C., and Grubbs, B. R. 1974. Field testing of laterally loaded piles in sand. *In Proceedings, Offshore Technology Conference, Offshore Technology Conference, 1974.*
- Coyle, H. M., and Reese, L. C. 1966. Load transfer for axially loaded pile in clay. *Proc. ASCE*, SM2.
- Das, B. M. 2013. Earth anchors. J. Ross Publishing Inc., Pine Island, Florida.
- El Naggar, M. H, Shayanfar, M. A., Kimiaei, M., and Aghakouchak, A. A. 2005. Simplified BNWF model for nonlinear seismic response analysis of offshore piles with nonlinear input ground motion analysis, *Canadian Geotechnical Journal*, 42(2): 365-380.
- Elkasabgy, M. A., and El Naggar, M. H. 2015. Lateral performance of large-capacity helical piles. *In Proceeding of the International Foundations Congress and Equipment Expo 2015.*

- U.S. Army corps of Engineers (US-ACE). 1991. Design of Pile Foundations, Engineer Manual EM 1110-2-2906, Washington DC, US.
- Gavin, K., Doherty, P., and Tolooiyan, A. 2014. Field investigation of the axial resistance of helical piles in dense sand. *Canadian Geotechnical Journal*, 51(11): 1343-1354.
- Ghaly, A., Hanna, A., and Hanna, M. 1991. Uplift behavior of screw anchors in sand. I: dry sand, *Journal of Geotechnical Engineering*, 117(5): 773-793.
- Heydinger, A. G. 1987. Recommendations: Load-Transfer Criteria for Piles in Clay. Department of Civil Engineering, University of Toledo, Toledo, Ohio.
- Hoyt, R. M., & Clemence, S. P. 1989. Uplift capacity of helical anchors in soil. *In Proceedings of the 12th International Conference on Soil Mechanics and Foundation Engineering*, Rio de Janeiro, Brazil, Vol. 2, pp. 1019-1022.
- Kurian, N. P., and Shah, S. J. 2009. Studies on the behaviour of screw piles by the finite element method, *Canadian Geotechnical Journal*, 46(6): 627-638.
- Livneh, B., and El Naggar, M. H. 2008. Axial testing and numerical modeling of square shaft helical piles under compressive and tensile loading, *Canadian Geotechnical Journal*, 45(8): 1142-1155.
- Li, W., Schmidt, R., Li, B., and Deng, L. 2015. In-situ loading tests of small-diameter helical piles and evaluation of design methods. Annual Conf. Canadian Geotechnical Society, Quebec City, Que.
- Li, W., and Deng, L. 2015. OpenSees simulations of axial behaviour of single-helix piles. Annual Conf. Canadian Geotechnical Society, Quebec City, Que.

- Li, W., Zhang, D.J.Y., Sego, D.C., and Deng, L. 2016. Field testing of axial performance of helical piles in cohesive and cohesionless soils, *ASCE Journal of Geotechnical and Geoenvironmental Engineering*, in 2nd review.
- Matlock, H. 1970. Correlations for design of laterally loaded piles in soft clay, *Offshore Technology in Civil Engineering's Hall of Fame Papers from the Early Years*, 77-94.
- Meyerhof, G. G. 1974. Ultimate bearing capacity of footings on sand layer overlying clay. *Canadian Geotechnical Journal*, 11(2): 223-229.
- Meyerhof, G. G. 1976. Bearing capacity and settlement of pile foundations, *Journal of the Geotechnical Engineering Division, ASCE*, 102(3): 195-228.
- Mitsch, M.P., and Clemence, S.P. 1985. The uplift capacity of helix anchors in sand. *In Uplift Behaviour of Anchor Foundations in Soil: Proceedings of ASCE*. New York, New York, pp. 26-47.
- Mooney, J.M., Adamczak, S., and Clemence, S.P. 1985. Uplift capacity of helix anchors in clay and silt. *In Uplift Behaviour of Anchor Foundations in Soil: Proceedings of ASCE*. New York, NY, pp. 48-72.
- Mosher, R. L. 1984. Load-transfer criteria for numerical analysis of axially loaded piles in sand. Part 1: Load-transfer criteria, Final Report Army Engineer Waterways Experiment Station, Vicksburg, MS., 1.
- Mosher, R. L., and Dawkins, W. P. 2000. Theoretical manual for pile foundations (No. ERDC/ITL-TR-00-5). Engineering research and development center, Vicksburg, MS.
- Narasimha Rao, S., Prasad, Y.V.S.N., and Veeresh, C. 1993. Behaviour of embedded model screw anchors in soft clays. *Geotechnique*, 43: 605-614.

- Narasimha Rao, S., Prasad, Y.V.S.N., Shetty, M.D., and Joshi, V.V. 1989. Uplift capacity of screw pile anchors. *Geotechnical Engineering*, 20(2): 139-159. No. 2079, Houston, Texas.
- O'Neill, M.W., and Reese, L.C. 1999. Drilled shafts: Construction procedures and design methods. U.S. Depart. of Transportation, Federal Highway Administration (FHWA), Report No. FHWA-IF-99-025.
- Open System for Earthquake Engineering Simulation (OpenSees). 2016. <http://opensees.berkeley.edu>.
- Prakash, S., and Sharma, H.D. 1990. Pile foundations in engineering practice. John Wiley and Sons, Inc., 1st Edition, 721p.
- Prasad, Y. V., and Rao, S. N. 1996. Lateral capacity of helical piles in clays. *Journal of Geotechnical Engineering*, 122(11), 938-941.
- Puri, V. K., Stephenson, R. W., Dziedzic, E., and Goen, L. 1984. Helical anchor piles under lateral loading. *In Laterally Loaded Deep Foundations: Analysis and Performance*. ASTM, West Conshohocken, PA.
- Rao, S. N., Prasad, Y. V. S. N., and Shetty, M. D. 1991. The behaviour of model screw piles in cohesive soils, *Soils and Foundations*, 31(2): 35-50.
- Rao, S. N., Prasad, Y. V. S. N., and Veeresh, C. 1993. Behaviour of embedded model screw anchors in soft clays, *Geotechnique*, 43(4): 605-614.
- Reese, L. C. and M. W. O'Neill. 1987. Drilled shafts: Construction procedures and design methods. Report No. FHWA-HI-88-042, U.S. Department of Transportation, Federal Highway Administration, Office of Implementation, McLean, Virginia.

- Reese, L. C., and Sullivan, W. R. 1980. Documentation of computer program COM624; Parts I and II, Analysis of stresses and deflections for laterally-loaded piles including generation of p-y curves,” Geotechnical Engineering Software SG80-1, Geotechnical Engineering Center, Bureau of Engineering Research, University of Texas at Austin.
- Reese, L. C., and Welch, R. C. 1975. Lateral loading of deep foundations in stiff clay, *Journal of the Geotechnical Engineering Division, ASCE*, 101(7): 633-649.
- Reese, L. C., Cox, W. R., and Koop, F. D. 1974. Analysis of laterally loaded piles in sand. *In Proceedings, Fifth Annual Offshore Technology Conference, Paper No. OTC 2080, Houston, Texas.*
- Robertson, P. K., and Cabal Robertson. 2012. Guide to cone penetration testing for geotechnical engineering, Gregg Drilling & Testing Inc., Martinez, California.
- Sakr, M. 2009. Performance of helical piles in oil sand. *Canadian Geotechnical Journal*, 46(9): 1046-1061.
- Tappenden, K. M. 2007. Predicting the axial capacity of screw piles installed in Western Canadian soils. M.Sc. thesis, Department of Civil and Environmental Engineering, University of Alberta, Edmonton, Alberta.
- Terzaghi, K. 1943. *Theoretical soil mechanics*, Wiley, New York, USA.
- Todeshkejoei, C., Hambleton, J. P., Stanier, S. A., and Gaudin, C. 2014. Modelling installation of helical anchors in clay. *In Proceeding 14th International Conference of the International Association for Computer Methods and Advances in Geomechanics*, pp. 22-25.
- Tomlinson, M. J. 1957, August. The adhesion of piles driven in clay soils. *In Proceedings of the 4th International Conference on Soil Mechanics and Foundation Engineering*. pp. (2): 66-71.

- Tsuha, C. D. H. C., and Aoki, N. 2010. Relationship between installation torque and uplift capacity of deep helical piles in sand. *Canadian Geotechnical Journal*, 47(6): 635-647.
- Tsuha, C. H. C., Aoki, N., Rault, G., Thorel, L., and Garnier, J. 2007. Physical modelling of helical pile anchors. *International Journal of Physical Modelling in Geotechnics*, 7(4): 01-12.
- Vijayvergiya, V. N. 1977. Load-movement characteristics of piles. *In Proceeding of the Ports'77. 4th annual symposium of the American Society of Civil Engineers, Waterway, Port, Coastal and Ocean Division, Long Beach, California.* pp. (2): 269-284.
- Zhang, D. 1999. Predicting capacity of helical screw piles in Alberta soils. M.Sc. thesis, Department of Civil and Environmental Engineering, University of Alberta, Edmonton, Alberta.

Appendix – OpenSees code for lateral soil – helical pile interaction

The code of the parametric analysis of D and H

```
#####  
# Weidong Li #  
# Geotech Eng, Department of Civil & Environmental #  
# University of Alberta #  
#####  
  
wipe  
puts "D&H Based on Sakr's test results"  
for {set m 1} {$m<=10} {incr m} {;### m is the index used to change the helix diameter D  
set D [expr 0.406 +$m*0.105]; ## helix diameter in m  
# set basic constants  
set pi 3.141592654  
set g 9.81; #gravitational acceleration, m/s2  
# Section 1, set pile demensions  
#####  
set d 0.178 ;## pile shaft diameter in m  
set t [expr $d-2*0.00920]; ## pile inner dia, m  
for {set n 1} {$n<=22} {incr n} {;## n is the index used to change the embedment of the top helix H  
set s [expr $n*0.2]; # spacing of helices is varied so that the embedment of top helix is varied  
set tk 0.0191; # thickness of helix, m  
set l 5.8; #length of pile, m  
set l1 5.2; #pile length below ground surface,in m  
set l2 0.6; #pile length above ground surface,in m  
set p 0.16; ## helix pitch, m  
set h1 0.2 ;#the height of the bottom of the first helix, is fixed  
set h2 [expr $h1+$s+$p]; #the height of the bottom of the second helix  
  
set sizeEle 0.04; #length of each pile element, m  
  
set nSegHelixBeam 5; #number of helix segments on each helix beam  
set sizeHelixSeg [expr ($D-$d)/(2*$nSegHelixBeam)]; #size of the helix segment on each beam, m  
set nPitchEle 12; #number of pitch element  
set sizePitchEle [expr $p/$nPitchEle];# length of pitch element, m  
set nSpaceEle [expr round ($s/$sizeEle)]; #number of elements in spacing  
  
set delta [expr 2*$pi/$nPitchEle]; ## rad of each helix segment  
set A1 [expr 0.25*$pi*(pow($d+2*$sizeHelixSeg,2)-pow($d+0*$sizeHelixSeg,2))/ $nPitchEle]  
set A2 [expr 0.25*$pi*(pow($d+4*$sizeHelixSeg,2)-pow($d+2*$sizeHelixSeg,2))/ $nPitchEle]  
set A3 [expr 0.25*$pi*(pow($d+6*$sizeHelixSeg,2)-pow($d+4*$sizeHelixSeg,2))/ $nPitchEle]  
set A4 [expr 0.25*$pi*(pow($d+8*$sizeHelixSeg,2)-pow($d+6*$sizeHelixSeg,2))/ $nPitchEle]  
set A5 [expr 0.25*$pi*(pow($d+10*$sizeHelixSeg,2)-pow($d+8*$sizeHelixSeg,2))/ $nPitchEle]  
## set the areas of the helix beam elements  
  
# code of certain nodes  
set endTip [expr round ($h1/$sizeEle)+1]  
set startHelix1 [expr $endTip + 1]  
set endHelix1 [expr $startHelix1 + $nPitchEle -1]  
set startSpace [expr $endHelix1+1]  
set endSpace [expr $startSpace+$nSpaceEle]
```

```

set startHelix2 [expr $endSpace+1]
set endHelix2 [expr $endSpace+$nPitchEle]
set startPipeEmb [expr $endHelix2 +1]
set endPipeEmb [expr $startPipeEmb +round(($l1-$h2-$p)/$sizeEle)]
set nNode [expr $endPipeEmb +round($l2/$sizeEle)]
set nLoad [expr $endPipeEmb +round(0.5*$l2/$sizeEle)]
puts "nLoad $nLoad"

model BasicBuilder -ndm 3 -ndf 6

# create pile nodes and fixity at tip
for {set i 1} {$i<=$endTip} {incr i} {
    node $i 0.0 0.0 [expr ($i-1)*$sizeEle]
    fix $i 0 0 0 0 0
}

# create spring nodes and fixity at tip
for {set i 1} {$i<=$endTip} {incr i} {
    node [expr 1000+$i] 0.0 0.0 [expr ($i-1)*$sizeEle]
    fix [expr 1000+$i] 1 1 1 1 1
}

# create pile nodes and fixity at helix1
for {set i $startHelix1} {$i<=$endHelix1} {incr i} {
    node $i 0.0 0.0 [expr ($i-$endTip-0.5)*$sizePitchEle+$h1]
    fix $i 0 0 0 0 0
}

# create pile nodes and fixity at space
for {set i $startSpace} {$i<=$endSpace} {incr i} {
    node $i 0.0 0.0 [expr ($i-$startSpace)*$sizeEle+$p+$h1]
    fix $i 0 0 0 0 0
}

# create spring nodes and fixity at space
for {set i $startSpace} {$i<=$endSpace} {incr i} {
    node [expr 1000+$i] 0.0 0.0 [expr ($i-$startSpace)*$sizeEle+$p+$h1]
    fix [expr 1000+$i] 1 1 1 1 1
}

# create pile nodes and fixity at helix2
for {set i $startHelix2} {$i<=$endHelix2} {incr i} {
    node $i 0.0 0.0 [expr ($i-$endSpace-0.5)*$sizePitchEle+$h2]
    fix $i 0 0 0 0 0
}

# create embedded pipe nodes and fixity above top helix
for {set i $startPipeEmb} {$i<=$endPipeEmb} {incr i} {
    node $i 0.0 0.0 [expr ($i-$startPipeEmb)*$sizeEle+$p+$h2]
    fix $i 0 0 0 0 0
}

# create embedded spring nodes and fixity above top helix
for {set i $startPipeEmb} {$i<=$endPipeEmb} {incr i} {
    node [expr 1000+$i] 0.0 0.0 [expr ($i-$startPipeEmb)*$sizeEle+$p+$h2]
    fix [expr 1000+$i] 1 1 1 1 1
}

# create helix segment nodes and fixity at helix1

```

```

for {set i $startHelix1} {$i<=$endHelix1} {incr i} {
  node [expr $i+1000] [expr (0.5*$d+1*$sizeHelixSeg)*sin(($i-$startHelix1)*$delta)] [expr
(0.5*$d+1*$sizeHelixSeg)*cos(($i-$startHelix1)*$delta)] [expr ($i-$endTip-0.5)*$sizePitchEle+$h1]
  node [expr $i+2000] [expr (0.5*$d+2*$sizeHelixSeg)*sin(($i-$startHelix1)*$delta)] [expr
(0.5*$d+2*$sizeHelixSeg)*cos(($i-$startHelix1)*$delta)] [expr ($i-$endTip-0.5)*$sizePitchEle+$h1]
  node [expr $i+3000] [expr (0.5*$d+3*$sizeHelixSeg)*sin(($i-$startHelix1)*$delta)] [expr
(0.5*$d+3*$sizeHelixSeg)*cos(($i-$startHelix1)*$delta)] [expr ($i-$endTip-0.5)*$sizePitchEle+$h1]
  node [expr $i+4000] [expr (0.5*$d+4*$sizeHelixSeg)*sin(($i-$startHelix1)*$delta)] [expr
(0.5*$d+4*$sizeHelixSeg)*cos(($i-$startHelix1)*$delta)] [expr ($i-$endTip-0.5)*$sizePitchEle+$h1]
  node [expr $i+5000] [expr (0.5*$d+5*$sizeHelixSeg)*sin(($i-$startHelix1)*$delta)] [expr
(0.5*$d+5*$sizeHelixSeg)*cos(($i-$startHelix1)*$delta)] [expr ($i-$endTip-0.5)*$sizePitchEle+$h1]
  fix [expr $i+1000] 0 0 0 0 0
  fix [expr $i+2000] 0 0 0 0 0
  fix [expr $i+3000] 0 0 0 0 0
  fix [expr $i+4000] 0 0 0 0 0
  fix [expr $i+5000] 0 0 0 0 0
}

# create helix spring nodes and fixity at helix1
for {set i $startHelix1} {$i<=$endHelix1} {incr i} {
  node [expr $i+6000] [expr (0.5*$d+1*$sizeHelixSeg)*sin(($i-$startHelix1)*$delta)] [expr
(0.5*$d+1*$sizeHelixSeg)*cos(($i-$startHelix1)*$delta)] [expr ($i-$endTip-0.5)*$sizePitchEle+$h1]
  node [expr $i+7000] [expr (0.5*$d+2*$sizeHelixSeg)*sin(($i-$startHelix1)*$delta)] [expr
(0.5*$d+2*$sizeHelixSeg)*cos(($i-$startHelix1)*$delta)] [expr ($i-$endTip-0.5)*$sizePitchEle+$h1]
  node [expr $i+8000] [expr (0.5*$d+3*$sizeHelixSeg)*sin(($i-$startHelix1)*$delta)] [expr
(0.5*$d+3*$sizeHelixSeg)*cos(($i-$startHelix1)*$delta)] [expr ($i-$endTip-0.5)*$sizePitchEle+$h1]
  node [expr $i+9000] [expr (0.5*$d+4*$sizeHelixSeg)*sin(($i-$startHelix1)*$delta)] [expr
(0.5*$d+4*$sizeHelixSeg)*cos(($i-$startHelix1)*$delta)] [expr ($i-$endTip-0.5)*$sizePitchEle+$h1]
  node [expr $i+10000] [expr (0.5*$d+5*$sizeHelixSeg)*sin(($i-$startHelix1)*$delta)] [expr
(0.5*$d+5*$sizeHelixSeg)*cos(($i-$startHelix1)*$delta)] [expr ($i-$endTip-0.5)*$sizePitchEle+$h1]
  fix [expr $i+6000] 1 1 1 1 1
  fix [expr $i+7000] 1 1 1 1 1
  fix [expr $i+8000] 1 1 1 1 1
  fix [expr $i+9000] 1 1 1 1 1
  fix [expr $i+10000] 1 1 1 1 1
}

# create helix segment nodes and fixity at helix2
for {set i $startHelix2} {$i<=$endHelix2} {incr i} {
  node [expr $i+1000] [expr (0.5*$d+1*$sizeHelixSeg)*sin(($i-$startHelix2)*$delta)] [expr
(0.5*$d+1*$sizeHelixSeg)*cos(($i-$startHelix2)*$delta)] [expr ($i-$endSpace-0.5)*$sizePitchEle+$h2]
  node [expr $i+2000] [expr (0.5*$d+2*$sizeHelixSeg)*sin(($i-$startHelix2)*$delta)] [expr
(0.5*$d+2*$sizeHelixSeg)*cos(($i-$startHelix2)*$delta)] [expr ($i-$endSpace-0.5)*$sizePitchEle+$h2]
  node [expr $i+3000] [expr (0.5*$d+3*$sizeHelixSeg)*sin(($i-$startHelix2)*$delta)] [expr
(0.5*$d+3*$sizeHelixSeg)*cos(($i-$startHelix2)*$delta)] [expr ($i-$endSpace-0.5)*$sizePitchEle+$h2]
  node [expr $i+4000] [expr (0.5*$d+4*$sizeHelixSeg)*sin(($i-$startHelix2)*$delta)] [expr
(0.5*$d+4*$sizeHelixSeg)*cos(($i-$startHelix2)*$delta)] [expr ($i-$endSpace-0.5)*$sizePitchEle+$h2]
  node [expr $i+5000] [expr (0.5*$d+5*$sizeHelixSeg)*sin(($i-$startHelix2)*$delta)] [expr
(0.5*$d+5*$sizeHelixSeg)*cos(($i-$startHelix2)*$delta)] [expr ($i-$endSpace-0.5)*$sizePitchEle+$h2]
  fix [expr $i+1000] 0 0 0 0 0
  fix [expr $i+2000] 0 0 0 0 0
  fix [expr $i+3000] 0 0 0 0 0
  fix [expr $i+4000] 0 0 0 0 0
  fix [expr $i+5000] 0 0 0 0 0
}

```

```

# create helix spring nodes and fixity at helix2
for {set i $startHelix2} {$i<=$endHelix2} {incr i} {
  node [expr $i+6000] [expr (0.5*$d+1*$sizeHelixSeg)*sin(($i-$startHelix2)*$delta)] [expr
(0.5*$d+1*$sizeHelixSeg)*cos(($i-$startHelix2)*$delta)] [expr ($i-$endSpace-0.5)*$sizePitchEle+$h2]
  node [expr $i+7000] [expr (0.5*$d+2*$sizeHelixSeg)*sin(($i-$startHelix2)*$delta)] [expr
(0.5*$d+2*$sizeHelixSeg)*cos(($i-$startHelix2)*$delta)] [expr ($i-$endSpace-0.5)*$sizePitchEle+$h2]
  node [expr $i+8000] [expr (0.5*$d+3*$sizeHelixSeg)*sin(($i-$startHelix2)*$delta)] [expr
(0.5*$d+3*$sizeHelixSeg)*cos(($i-$startHelix2)*$delta)] [expr ($i-$endSpace-0.5)*$sizePitchEle+$h2]
  node [expr $i+9000] [expr (0.5*$d+4*$sizeHelixSeg)*sin(($i-$startHelix2)*$delta)] [expr
(0.5*$d+4*$sizeHelixSeg)*cos(($i-$startHelix2)*$delta)] [expr ($i-$endSpace-0.5)*$sizePitchEle+$h2]
  node [expr $i+10000] [expr (0.5*$d+5*$sizeHelixSeg)*sin(($i-$startHelix2)*$delta)] [expr
(0.5*$d+5*$sizeHelixSeg)*cos(($i-$startHelix2)*$delta)] [expr ($i-$endSpace-0.5)*$sizePitchEle+$h2]
  fix [expr $i+6000] 1 1 1 1 1 1
  fix [expr $i+7000] 1 1 1 1 1 1
  fix [expr $i+8000] 1 1 1 1 1 1
  fix [expr $i+9000] 1 1 1 1 1 1
  fix [expr $i+10000] 1 1 1 1 1 1
}

```

```

# create pipe nodes and fixity above ground
for {set i [expr $endPipeEmb+1]} {$i<=$nNode} {incr i} {
  node $i 0.0 0.0 [expr ($i-$endPipeEmb)*$sizeEle+$l1]
  fix $i 0 0 0 0 0 0
}

```

```

puts "pile dimension created"
# springs assignment
#####
# soil properties
set GWT 1.1 ; #GWT depth,m
set u 0.0055; #y50, m
set k0 0.4; # a constant adopted by API sand
set puK 0.3; #factor used to adjust pult
set yK 6.0; # factor used to adjust y50
set Phi 38; #internal friction angle of the sand, degree
set gamma [expr 22.2-$g];# effective unit weight of the sand, kN/m^3
set Nq [expr 0.1581*pow(2.7182818284,0.1462*$Phi)];# meyerhof's bearing factor for drilled pile

```

```

# create and install py spring at tip, 1000+i ### API sand (1993)
for {set i 1} {$i<=$endTip} {incr i} {
  set z [expr $l1-($i-1)*$sizeEle]
  set sigma [expr $z*$gamma]

  set fi [expr $pi*($Phi-0)/180]
  set beta [expr 0.25*$pi+$fi]
  set alpha [expr 0.5*$fi]
  set ka [expr pow(tan(0.25*$pi-$alpha),2)]
  set c1 [expr $k0*tan($fi)*sin($beta)/(tan($beta-$fi)*cos($alpha)) +
pow(tan($beta),2)*tan($alpha)/tan($beta-$fi) + $k0*tan($beta)*(tan($fi)*sin($beta)- tan($alpha))]
  set c2 [expr tan($beta)/tan($beta-$fi)-$ka]
  set c3 [expr $k0*tan($fi)*pow(tan($beta),4)+$ka]
  set pu1 [expr ($c1*$z+$c2*$d)*$sigma*$puK]
  set pu2 [expr $c3*$d*$sigma*$puK]

  if { $pu1>$pu2} {

```

```

        set pult [expr $pu2*$sizeEle]} else {
        set pult [expr $pu1*$sizeEle]
    }
    set zbRatio [expr $z/$d];
    if {$z<=1.1} {
    set k [expr 271.447*80]} else {
    set k [expr 271.447*122]}
    set atanh_value 0.238561
if {$zbRatio <= 5} {
    set As [expr 0.1039*pow($zbRatio,2)-0.9076*$zbRatio+2.852]} else {
    set As 0.88}
    set y50 [expr $yK*0.5*$atanh_value*$pult*$z/($sizeEle*$As*$k)]
    uniaxialMaterial PySimple1 [expr $i+500] 2 $pult $y50 0.1
    element zeroLength [expr 500+$i] $i [expr $i + 1000] -mat [expr $i+500] [expr $i+500] -dir 1 2
}
puts "Py tip done"
# create and install py spring at space, 1000+i
for {set i $startSpace} {$i<=$endSpace} {incr i} {
    set z [expr $l1-$h1-$p-($i-$startSpace)*$sizeEle]
    set sigma [expr $z*$gamma]

    set fi [expr $pi*(($Phi-0)/180]
    set beta [expr 0.25*$pi+$fi]
    set alpha [expr 0.5*$fi]
    set ka [expr pow(tan(0.25*$pi-$alpha),2)]
    set c1 [expr $k0*tan($fi)*sin($beta)/(tan($beta-$fi)*cos($alpha)) +
pow(tan($beta,2)*tan($alpha)/tan($beta-$fi) + $k0*tan($beta)*(tan($fi)*sin($beta)- tan($alpha))]
    set c2 [expr tan($beta)/tan($beta-$fi)-$ka]
    set c3 [expr $k0*tan($fi)*pow(tan($beta),4)+$ka]
    set pu1 [expr ($c1*$z+$c2*$d)*$sigma*$puK]
    set pu2 [expr $c3*$d*$sigma*$puK]

    if { $pu1>$pu2} {
        set pult [expr $pu2*$sizeEle]} else {
        set pult [expr $pu1*$sizeEle]
    }
    set zbRatio [expr $z/$d];
    if {$z<=1.1} {
    set k [expr 271.447*80]} else {
    set k [expr 271.447*122]}
    set atanh_value 0.238561
if {$zbRatio <= 5} {
    set As [expr 0.1039*pow($zbRatio,2)-0.9076*$zbRatio+2.852]} else {
    set As 0.88}
    set y50 [expr $yK*0.5*$atanh_value*$pult*$z/($sizeEle*$As*$k)]
    uniaxialMaterial PySimple1 [expr $i+500] 2 $pult $y50 0.1
    element zeroLength [expr 500+$i] $i [expr $i + 1000] -mat [expr $i+500] [expr $i+500] -dir 1 2
}
puts "Py space done"
# create and install py spring at embedment, 1000+i
for {set i $startPipeEmb} {$i<=$endPipeEmb} {incr i} {
    set z [expr $l1-$h2-$p-($i-$startPipeEmb)*$sizeEle+$sizeEle/2]
    set sigma [expr $z*$gamma]

    set fi [expr $pi*(($Phi-0)/180]
    set beta [expr 0.25*$pi+$fi]

```

```

set alpha [expr 0.5*$fi]
set ka [expr pow(tan(0.25*$pi-$alpha),2)]
set c1 [expr $k0*tan($fi)*sin($beta)/(tan($beta-$fi)*cos($alpha)) +
pow(tan($beta),2)*tan($alpha)/tan($beta-$fi) + $k0*tan($beta)*(tan($fi)*sin($beta)- tan($alpha))]
set c2 [expr tan($beta)/tan($beta-$fi)-$ka]
set c3 [expr $k0*tan($fi)*pow(tan($beta),4)+$ka]
set pu1 [expr ($c1*$z+$c2*$d)*$sigma*$puK]
set pu2 [expr $c3*$d*$sigma*$puK]

if { $pu1>$pu2 } {
  set pult [expr $pu2*$sizeEle]} else {
  set pult [expr $pu1*$sizeEle]
}
set zbRatio [expr $z/$d];
if {$zbRatio<=1.1} {
  set k [expr 271.447*80]} else {
  set k [expr 271.447*122]}
set atanh_value 0.238561
if {$zbRatio <= 5} {
  set As [expr 0.1039*pow($zbRatio,2)-0.9076*$zbRatio+2.852]} else {
  set As 0.88}
set y50 [expr $yK*0.5*$atanh_value*$pult*$z/($sizeEle*$As*$k)]
uniaxialMaterial PySimple1 [expr $i+500] 2 $pult $y50 0.1
element zeroLength [expr 500+$i] $i [expr $i + 1000] -mat [expr $i+500] [expr $i+500] -dir 1 2
}

puts "Py emb done"

# create and install qz spring and tz spring in helix 1
# Meyerhof (1976) for qult, Vijayvergiya (1977) for z50q, and Mosher (1984) for tult and z50t.

for {set i $startHelix1} {$i<=$endHelix1} {incr i} {
  set z [expr $l1-$h1-($i-$endTip-0.5)*$sizePitchEle]
  set sigma [expr $z*$gamma]
  set qu [expr $Nq*$sigma]
  set z50q [expr 0.05*0.2*$D]

  if { (32<=$Phi) && ($Phi<=35)} {
    set Kf [expr 1.88326*(10000+4000*($Phi-32)/3)]
  } elseif { (35<$Phi) && ($Phi<=38)} {
    set Kf [expr 1.88326*(14000+4000*($Phi-35)/3)]
  }
  set Kp [expr (1+sin($Phi*$pi/180))/(1-sin($Phi*$pi/180))]
  set tu [expr $Kp*$sigma*tan(0.667*$Phi*$pi/180)]
  set z50t [expr $tu/$Kf]

  uniaxialMaterial QzSimple1 [expr $i+1000] 2 [expr $qu*$A1] $z50q
  uniaxialMaterial TzSimple1 [expr $i+6000] 2 [expr $tu*$A1] $z50t
  element zeroLength [expr $i+1000] [expr $i+1000] [expr $i+6000] -mat [expr $i+1000] [expr $i+6000]
[expr $i+6000] -dir 3 2 1
  uniaxialMaterial QzSimple1 [expr $i+2000] 2 [expr $qu*$A2] $z50q
  uniaxialMaterial TzSimple1 [expr $i+7000] 2 [expr $tu*$A2] $z50t
  element zeroLength [expr $i+2000] [expr $i+2000] [expr $i+7000] -mat [expr $i+2000] [expr $i+7000]
[expr $i+7000] -dir 3 2 1
  uniaxialMaterial QzSimple1 [expr $i+3000] 2 [expr $qu*$A3] $z50q
  uniaxialMaterial TzSimple1 [expr $i+8000] 2 [expr $tu*$A3] $z50t

```

```

        element zeroLength [expr $i+3000] [expr $i+3000] [expr $i+8000] -mat [expr $i+3000] [expr $i+8000]
[expr $i+8000] -dir 3 2 1
        uniaxialMaterial QzSimple1 [expr $i+4000] 2 [expr $qu*$A4] $z50q
        uniaxialMaterial TzSimple1 [expr $i+9000] 2 [expr $tu*$A4] $z50t
        element zeroLength [expr $i+4000] [expr $i+4000] [expr $i+9000] -mat [expr $i+4000] [expr $i+9000]
[expr $i+9000] -dir 3 2 1
        uniaxialMaterial QzSimple1 [expr $i+5000] 2 [expr $qu*$A5] $z50q
        uniaxialMaterial TzSimple1 [expr $i+10000] 2 [expr $tu*$A5] $z50t
        element zeroLength [expr $i+5000] [expr $i+5000] [expr $i+10000] -mat [expr $i+5000] [expr $i+10000]
[expr $i+10000] -dir 3 2 1
    }
    puts "helix1 springs created"

# create and install qz spring and tz spring in helix2

for {set i $startHelix2} {$i<=$endHelix2} {incr i} {
    set z [expr $l1-$h2-($i-$endSpace-0.5)*$sizePitchEle]
    set sigma [expr $z*$gamma]
    set qu [expr $Nq*$sigma]
    set z50q [expr 0.05*0.2*$D]

    if { (32<=$Phi) && ($Phi<=35) } {
        set Kf [expr 1.88326*(10000+4000*($Phi-32)/3)]
    } elseif { (35<$Phi) && ($Phi<=38) } {
        set Kf [expr 1.88326*(14000+4000*($Phi-35)/3)]
    }

    set Kp [expr (1+sin($Phi*$pi/180))/(1-sin($Phi*$pi/180))]
    set tu [expr $Kp*$sigma*tan(0.667*$Phi*$pi/180)]
    set z50t [expr $tu/$Kf]

    uniaxialMaterial QzSimple1 [expr $i+1000] 2 [expr $qu*$A1] $z50q
    uniaxialMaterial TzSimple1 [expr $i+6000] 2 [expr $tu*$A1] $z50t
    element zeroLength [expr $i+1000] [expr $i+1000] [expr $i+6000] -mat [expr $i+1000] [expr $i+6000]
[expr $i+6000] -dir 3 2 1
    uniaxialMaterial QzSimple1 [expr $i+2000] 2 [expr $qu*$A2] $z50q
    uniaxialMaterial TzSimple1 [expr $i+7000] 2 [expr $tu*$A2] $z50t
    element zeroLength [expr $i+2000] [expr $i+2000] [expr $i+7000] -mat [expr $i+2000] [expr $i+7000]
[expr $i+7000] -dir 3 2 1
    uniaxialMaterial QzSimple1 [expr $i+3000] 2 [expr $qu*$A3] $z50q
    uniaxialMaterial TzSimple1 [expr $i+8000] 2 [expr $tu*$A3] $z50t
    element zeroLength [expr $i+3000] [expr $i+3000] [expr $i+8000] -mat [expr $i+3000] [expr $i+8000]
[expr $i+8000] -dir 3 2 1
    uniaxialMaterial QzSimple1 [expr $i+4000] 2 [expr $qu*$A4] $z50q
    uniaxialMaterial TzSimple1 [expr $i+9000] 2 [expr $tu*$A4] $z50t
    element zeroLength [expr $i+4000] [expr $i+4000] [expr $i+9000] -mat [expr $i+4000] [expr $i+9000]
[expr $i+9000] -dir 3 2 1
    uniaxialMaterial QzSimple1 [expr $i+5000] 2 [expr $qu*$A5] $z50q
    uniaxialMaterial TzSimple1 [expr $i+10000] 2 [expr $tu*$A5] $z50t
    element zeroLength [expr $i+5000] [expr $i+5000] [expr $i+10000] -mat [expr $i+5000] [expr $i+10000]
[expr $i+10000] -dir 3 2 1
    }
    puts "helix2 springs created"

# transformation
geomTransf Linear 1 1 0 0; #pile shaft elements

```

```

geomTransf Linear 2 0 0 1; #helix elements

# create pile elements, 2000+i

set E 200000000.0; #psi 200GPa
set Fy 235000.0; #235MPa
set b 0.1; #hardening ratio
set R0 15.0
set cR1 0.925
set cR2 0.15
uniaxialMaterial Steel02 5000 $Fy $E $b $R0 $cR1 $cR2
uniaxialMaterial Steel01 6000 $Fy $E $b

#section of pipe
section Fiber 1 {
  patch circ 5000 36 9 0.0 0.0 [expr $t/2] [expr $d/2] 0.0 360.0
}
set sectionPipe 11
section Aggregator $sectionPipe 5000 T -section 1
# section of helix
section Fiber 2 {
  patch circ 6000 36 9 0.0 0.0 0.0 [expr $d/2] 0.0 360.0
}
set sectionHelix 12
section Aggregator $sectionHelix 6000 T -section 2

for {set i 1} {$i<=[expr $nNode-1]} {incr i} {

  element dispBeamColumn [expr $i+600000] $i [expr $i+1] 3 $sectionPipe 1
}

puts "pile elements created"

#create helix plate element
for {set i $startHelix1} {$i<=$endHelix1} {incr i} {
  element dispBeamColumn [expr $i+100000] $i [expr $i+1000] 3 $sectionHelix 2
  element dispBeamColumn [expr $i+200000] [expr $i+1000] [expr $i+2000] 3 $sectionHelix 2
  element dispBeamColumn [expr $i+300000] [expr $i+2000] [expr $i+3000] 3 $sectionHelix 2
  element dispBeamColumn [expr $i+400000] [expr $i+3000] [expr $i+4000] 3 $sectionHelix 2
  element dispBeamColumn [expr $i+500000] [expr $i+4000] [expr $i+5000] 3 $sectionHelix 2
  ##          elementTag      , iNode      , jNode      , number of integrator points ,
sectionTag ,TransformationTag
}
puts "helix1 plates created"

for {set i $startHelix2} {$i<=$endHelix2} {incr i} {
  element dispBeamColumn [expr $i+100000] $i [expr $i+1000] 3 $sectionHelix 2
  element dispBeamColumn [expr $i+200000] [expr $i+1000] [expr $i+2000] 3 $sectionHelix 2
  element dispBeamColumn [expr $i+300000] [expr $i+2000] [expr $i+3000] 3 $sectionHelix 2
  element dispBeamColumn [expr $i+400000] [expr $i+3000] [expr $i+4000] 3 $sectionHelix 2
  element dispBeamColumn [expr $i+500000] [expr $i+4000] [expr $i+5000] 3 $sectionHelix 2
  ##          elementTag      , iNode      , jNode      , number of integrator points ,
sectionTag ,TransformationTag
}

```

```

puts "helix2 plates created"

#create time series and load pattern

timeSeries Linear 1
pattern Plain 1 1 {
  load $nLoad 1.0 0.0 0.0 0.0 0.0 0.0
}
# record displacements at pile nodes

recorder Node -file SakDh/SakDh[expr 100+$m][expr 100+$n].txt -time -node $nLoad -dof 1 disp

recorder display "OpenSees Real Time" 10 10 700 1000 -wipe
prp      0 25 -1
vup      0 1 0
vpn      0 0 1
display  1 1 5

#create analysis
puts "analyzing"

constraints Transformation
numberer RCM
system SparseGeneral
test NormDispIncr 1.0e-6 20 0
algorithm Newton
integrator DisplacementControl $nLoad 1 [expr 0.02*$d]
analysis Static
analyze 5
puts "m $m n $n"
puts "The end, Thank you!"
wipe;
}
}

```